Technische Universität München
Institut für Energietechnik

Lehrstuhl für Thermodynamik

High Frequency Response of Auto-Ignition and Heat Release to Acoustic Perturbations

Mathieu Paul Gebhard Zellhuber

Vollständiger Abdruck der von der Fakultät für Maschinenwesen der Technischen Universität München zur Erlangung des akademischen Grades eines

DOKTOR – INGENIEURS

genehmigten Dissertation.

Vorsitzender:
Univ.-Prof. Dr.-Ing. Michael W. Gee
Prüfer der Dissertation:
1. Univ.-Prof. Wolfgang Polifke, Ph.D.
2. Assoc. Prof. Dr. ir. Jim B. W. Kok,
University of Twente / Niederlande

Die Dissertation wurde am 22.05.2013 bei der Technischen Universität München eingereicht und durch die Fakultät für Maschinenwesen am 30.10.2013 angenommen.

Preface/Vorwort

Die vorliegende Arbeit entstand während meiner Tätigkeit als wissenschaftlicher Mitarbeiter am Lehrstuhl für Thermodynamik der Technischen Universität München. Sie wurde im Rahmen der 2. Phase der Forschungsinitiative "Kraftwerke des 21. Jahrhunderts" (KW21) von Alstom Power und dem Freistaat Bayern gefördert.

Besonders danken möchte ich meinem Doktorvater, Herrn Professor Wolfgang Polifke, für die menschlich immer angenehme und wissenschaftlich stets anregende Zusammenarbeit in den vergangenen Jahren. Er gab mir das Vertrauen, mich von den Vorgaben des Projektantrags zu lösen und eine der Fragestellung angepasste Betrachtungsweise zu entwickeln. Er begleitete mich dabei mit zahlreichen kritischen Fragen und Anmerkungen, die mir manches (vieles) Kopfzerbrechen bereitet, aber immer (meistens) geholfen haben, das Rad noch etwas weiter zu drehen. Bei aller Begeisterung für komplizierte physikalische Zusammenhänge legte er immel viel Wert darauf, dass diese verständlich und klar dargestellt werden. In dieser Hinsicht durfte ich viel von ihm lernen und hoffe, dass sich dieser Gedanke in meiner Dissertation wiederfinden lässt.

Herrn Professor Jim Kok danke ich sehr herzlich für die Übernahme des Koreferates und Herrn Professor Michael Gee für die Übernahme des Vorsitzes während der mündlichen Prüfung.

Für die tolle inhaltliche Zusammenarbeit mit dem Industriepartner Alstom Power möchte ich mich stellvertretend bei den Herren Dr. Bruno Schuermans, Dr. Andreas Huber und Dr. Nicolas Noiray bedanken. Von meinen Aufenthalten im Entwicklungszentrum in Baden bin ich immer mit einem Koffer voller Ideen und Motivation zurückgekommen, die diese Arbeit wesentlich geprägt haben. Die intensiven und spannenden Diskussionen insbesondere mit Herrn Dr. Bruno Schuermans werden mir als sehr bereichernd in Erinnerung bleiben.

Allen Kolleginnen und Kollegen am Lehrstuhl danke ich für das kollegiale Arbeitsumfeld und die heitere Stimmung, die in einem Forschungsinstitut nicht selbstverständlich sind. Das macht das Arbeiten um einiges angenehmer, und falls doch mal ein Problem jedwelcher Art auftauchen sollte, so waren Frau

Helga Bassett und Frau Sigrid Schulz-Reichwald stets zur Stelle. Vielen Dank dafür!

Für die sehr gute Zusammenarbeit am Lehrstuhl möchte ich einigen weiteren Kollegen ausdrücklich danken. An erster Stelle meinem langjährigen Bürokollegen und Projektpartner, Dr. Rohit Kulkarni, mit dem ich zahlreiche Diskussionen rund um die Themen Verbrennungsmodellierung und Simulation führte, Frustrationen und Jubelarien ob der Simulationsergebnisse teilte und immer eine sehr angenehme und freundschaftliche Zusammenarbeit erlebte. Hervorheben möchte ich weiter die Herren Frédéric Collonval, Dr. Luis Tay Wo Chong und Dr. Joachim Schwing, mit denen ich ebenfalls intensiv zusammengearbeitet habe. Einen besonderen Dank möchte ich an die Herren Christoph Meraner und Josselin Guillozet aussprechen, die im Rahmen Ihrer Tätigkeiten als Hiwis und Diplomanden wertvolle Beiträge zum Gelingen dieser Arbeit geliefert haben. Den Essens-, Kaffee- und Freizeitkumpanen um Anja, Gary, Danilo, Plamen, Katrin, Volker, Eva, Vanja, Manuel, Alejandro, Hannes, Camilo et al. danke ich für unzählige witzige und hitzige Unterhaltungen am Tisch und an der Bar, auf Tanzflächen und Bierbänken, auf Skipisten und reißenden Flüssen.

Zu guter Letzt gilt mein innigster Dank meinen Freunden, meiner Familie und vor allem meinen Eltern Colette und Wolfgang, die mich stets unterstützt haben und mir immer verlässlich, offen und ehrlich zur Seite stehen. Merci beaucoup!

Martinsried, im Februar 2014 Mathieu Zellhuber

Teile dieser Dissertation wurden vom Autor bereits vorab als Konferenz- und Zeitschriftenbeiträge veröffentlicht [59, 122–128]. Alle Vorveröffentlichungen sind entsprechend der gültigen Promotionsordnung ordnungsgemäß gemeldet. Sie sind deshalb nicht zwangsläufig im Detail einzeln referenziert. Vielmehr wurde bei der Referenzierung eigener Vorveröffentlichungen Wert auf Verständlichkeit und inhaltlichen Bezug gelegt.

Parts of this Ph.D. thesis were published by the author beforehand in conference proceedings and journal papers [59, 122–128]. All of these prior printed publications are registered according to the valid doctoral regulations. For this reason, they are not quoted explicitly at all places. Whether these personal prior printed publications were referenced, depended on maintaining comprehensibility and providing all necessary context.

Kurzfassung

Die vorliegende Arbeit befasst sich mit der thermoakustischen Stabilität im Hochfrequenzbereich von Gasturbinenbrennkammern, die bei hohen Eintrittstemperaturen betrieben werden. Eine mathematische Beschreibung für lokale Schwankungen der Wärmefreisetzungsrate wird eingeführt, um die Nicht-Kompaktheit der Flamme in Bezug auf hochfrequente akustische Moden zu berücksichtigen. Mittels verschiedener numerischer Simulationstechniken wird die Flammenantwort insbesondere auf transversale akustische Störungen untersucht. Dabei stellt sich heraus, dass sich verschiedene Rückkopplungsmechanismen überlagern. Die eingeführte theoretische Beschreibung wird verifiziert, indem die Gesamtantwort der Flamme erfolgreich aus den Einzelbeiträgen rekonstruiert wird. Hierfür werden neuartige Auswertemethoden von Grobstruktursimulationen entwickelt und verwendet. Darüber hinaus werden für einige wichtige Rückkopplungsmechanismen Modelle von Flammentransferfunktionen vorgeschlagen, die für die Stabilitätsanalyse von realen Brennkammern verwendet werden können.

Abstract

This work is related to the thermoacoustic stability in the high frequency range of gas turbine combustors operating at elevated inlet temperatures. A mathematical description of local heat release rate fluctuations is proposed in order to account for the non-compactness of the flame with respect to high-frequency acoustic modes. Various numerical simulation techniques are employed to study the flame response in particular to transverse acoustic perturbations. The response is observed to be a superposition of different flame feedback mechanisms. The theoretical description introduced is verified by reconstructing the total flame response from the single feedback contributions. This is achieved by using newly developed postprocessing techniques for large eddy simulations. Moreover, flame transfer function models are proposed for several important feedback contributions; they can be used for the stability analysis of practical combustors.

Contents

List of Figures

List of Tables

Nomenclature

Latin letters

a	Speed of sound [m/s]
A	Area [m^2]
$\mathscr{A}$	Arrhenius pre-exponential factor [1/s]
b	Arrhenius temperature exponent [-]
c	Normalised reaction progress [-]
c_p	Specific heat capacity [J/(kg K)]
D	Thermal diffusivity [m^2/s]
Da	Damköhler number [-]
e_{ac}	Volumetric acoustic energy [J/m^3]
E_{ac}	Acoustic energy [J]
E_a	Activation energy [J/kg]
f, g	Riemann invariants [m/s]
h	Specific enthalpy [J/kg]
h	Specific sensible enthalpy [J/kg]
h_k°	Specific formation enthalpy of species k [J/kg]
H	Height [m]
k	Wave number [1/m]
l, L	Length [m]
m	Mass [kg]
$\dot{m}$	Mass flow [kg/s]
M	Mach number [-]
p	Pressure [Pa]
Pr	Prandtl number [-]
$\dot{q}$	Volumetric heat release rate [J/(m^3s)]
$\dot{Q}$	Heat release rate [J/s]
R	Gas constant [J/(kg K)]
ri	Volumetric Rayleigh index [kg^2/(s^4m^2)]
RI	Rayleigh index [kg^2m/s^4]

Sc	Schmidt number [-]
S_c	Flame consumption speed [m/s]
S_l	Laminar flame speed [m/s]
t	Time [s]
t^+	Reactor lifetime [s]
t_{ij}	Stress tensor [kg/(m s^2)]
T	Temperature [K]
$\mathcal{T}$	Oscillation period [s]
u, v, w	Velocity [m/s]
U'	Turbulence intensity [m/s]
V	Volume [m^3]
x, y, z	Spatial coordinates [m]
x_f	Flame position [m]
Y_c	Reaction progress [-]
Y_k	Mass fraction of species k [-]
Z	Mixture fraction [-]

Greek letters

α	Growth rate [1/s]
χ	Scalar dissipation rate [1/s]
δ	Dirac delta function [-]
Δ	Displacement [m]
η	Random value [-]
γ	Isentropic exponent [-]
Γ	Effective species diffusivity [m^2/s]
λ	Air excess ratio [-]
ν	Dynamic viscosity [m^2/s]
Φ	Phase [rad]
φ_p	Pressure sensitivity factor [-]
ρ	Density [kg/m^3]
σ	Spread of normal probability density function [s]
ω	Angular frequency [1/s]
$\dot{\omega}$	Reaction source term [1/s]
$\dot{\omega}_c$	Normalised progress variable source term [1/s]
$\dot{\omega}_h$	Mass-specific heat release rate [J/(kg s)]

τ	characteristic time scale [s]
ξ, ψ, ζ	Spatial coordinates in moving frame [m]

Indices

ac	Acoustic
$Arrh$	Related to Arrhenius expression
b	Burnt
c	On cold side
CA	Carrier air
$chem$	Chemical
dyn	Corresponding to dynamic reactor with time-variant pressure
f	Flame
F	Fuel
FD	Flame dynamics
h	On hot side
HF	High frequency limit
i	Conditions at injection point
ign	Ignition
in	Inlet conditions
inh	Inherent
mod	Modelled
mix	Mixing
Ox	Oxidiser
p	Pressure-related
pot	Potential velocity field
Φ	Mixing-related
$reconstr$	Reconstructed
res	Residual
Ref	Reference conditions
SGS	at subgrid scale range
$stat$	Corresponding to static reactor with constant pressure
$stoch$	Stochastic
$tech$	Technical premixing
t	Turbulence-related
u	Velocity-related

1,2	Conditions upstream and downstream of network element
+, −	Downstream and upstream direction

Symbols and operators

$\overline{(.)}$	Mean value
$(.)'$	Acoustic fluctuation
$\hat{(.)}$	Fluctuation amplitude
$\widetilde{(.)}$	Favre-filtered value in LES
$\langle . \rangle$	Reynolds-filtered value in LES
$(.)^{\star}$	Subgrid scale fluctuations
$\check{(.)}$	Complex fluctuation term
$(.)^{*}$	Complex conjugate
$\lvert . \rvert$	Absolute value
$(.)^{(n)}$	Realisation in n'th stochastic field
$\vec{\nabla}$	Spatial differentiation
$\vec{.}$	Vector notation
$\mathscr{F}$	Fourier transform
G	Green's function
$\mathscr{H}$	Heavyside step function

Acronyms and abbreviations

AI	Auto-ignition
CFD	Computational fluid dynamics
EV	Environmental
FDF	Flame describing function
FEM	Finite elements method
FP	Flame propagation
FTF	Flame transfer function
LES	Large eddy simulation
LHS, RHS	Left/Right hand side
SEV	Sequential environmental
UIR	Unit impulse response

1 Introduction

1.1 Economic context of power generation sector - Consequences for gas turbine development

The power generation sector is currently undergoing an important transition, which entails huge economic and technical challenges. In the context of CO_2 reduction needs and depletion of fossil fuel resources, the optimisation of power plant efficiency has been a major development objective for many years. Recently, operational flexibility has earned growing attention in the sector, since the increased use of renewable energies introduces a higher volatility in power generation. The political decision to turn away from nuclear energy in Germany imposes an additional strain on the local and European energy market, which thus needs innovative solutions to ensure a safe, affordable, and sustainable power supply.

Different scenarios are currently developed in order to show realistic pathways toward an electricity supply based on renewable energies. This is a primary goal in order to limit the global warming. The German Energy Agency (Deutsche Energie Agentur GmbH) has recently published an extensive outlook on the integration of renewables into the German and European electricity market [42]. With respect to Germany it projects an increase of renewable energy contribution to the gross electricity production from 16.7% in 2010 to 89% in 2050. Wind and solar energy will at that time represent more than 55% of the total renewable energy production. As mentioned, these energy sources are subjected to strong fluctuations, which need to be compensated by other resources in order to maintain a stable grid voltage.

As a remedy, a much larger reserve power will be needed by the middle of the century. This will mainly be provided by conventional, fossil power plants burning gas and coal. Indeed, while the fossil electricity production is projected to drop by 84.6% between 2010 and 2050, the installed fossil power ca-

pacity will only be reduced by 63.2%. It should be obvious that the requirements for new fossil power plants will change, since the operational flexibility will move more and more into the focus. The consequences for future fossil power plants can thus be summarised as follows:

1. Demand for base load power will be significantly reduced,
2. Operational flexibility will become a major customer requirement,
3. Compatibility with large-scale storage techniques will be of high interest.

Therefore, gas powered plants, in particular combined cycle gas turbine plants, are expected to ensure most of this fossil reserve power by 2050, as they offer already today the asset of a comparatively high load flexibility. Furthermore, the existing gas pipeline infrastructure could be used for the distribution of hydrogen and synthetic methane produced in periods of renewable energy overflow. In peak consumption hours, the chemically stored energy could be converted back to electrical power through combustion in gas turbines. As a consequence, the installed capacity of coal and oil in Germany is expected to drop from 38.1 GW (2010) to 11 GW until 2050, whereas the capacity based on gas will increase from 13.9 GW to 37.3 GW [42].

This outlook illustrates the challenges that gas turbine manufacturers will have to face in the next decades, namely to satisfy a growing market asking for highly developed products. Moreover, the traditional development credo of ”high efficiency at reduced emissions and lower costs” will be expanded by an additional dimension: the operational flexibility. The latter can be split into three different aspects:

1. Load flexibility: ensure low emissions and high efficiency over wide load ranges,
2. Fuel capability: guarantee stable operation with varying fuel types and qualities,
3. Low maintenance need: ensure high and schedulable plant availability.

With respect to combustor development, the ways to success adopted in the past consisted in increasing the turbine inlet temperature, and especially in

enhancing the mixing between fuel and oxidiser for stable, lean premix combustion. In addition, alternative concepts have received growing attention in recent years, as pointed out by Hellat [39]. Whereas the "Rich-Burn-Quick-Quench" concept and catalytic combustor concepts have not yet been applied at industrial scale, sequential combustion has been commercialised by Alstom in the 1990's in the GT24/GT26 gas turbine series. Details of such a sequential (also called reheat) combustion concept will be given in the following section. One of its main advantage consists in the increased load flexibility compared to conventional architectures.

Regardless of the chosen concept (apart maybe from catalytic combustion), the avoidance of thermoacoustic pulsations can be considered as one of the key criteria for ensuring a stable operation over wide load ranges. Indeed, when designed for base-load operation, stability can be guaranteed more easily since the operating conditions are well defined and subjected to few variations. However, this becomes a very challenging task when a multitude of operation points are involved, see the works of Bothien et al. [7] and Singla et al. [113]. A pure "trial and error" approach based on engine testing is therefore not suitable and needs to be complemented by a methodical approach based on a detailed understanding of thermoacoustic instabilities.

The present work contributes to the latter point and deals with the occurrence of high-frequency instabilities in reheat combustors, which can appear when moving the engine out of the typical operation window, as reported by Singla et al. [113]. Possible thermoacoustic feedback mechanisms are investigated with numerical simulation and analytical models are proposed. The research was carried out as a part of the German research initiative KW21 (second phase), whose objective is the further development of conventional fossil power plants able to ensure a sustainable and reliable transition to a "green" electrical power supply.

1.2 Sequential combustion systems

Before discussing thermoacoustic stability, a brief introduction to gas turbines with sequential combustion is given. These are generally characterised by the presence of two combustors that are arranged in series.

For example, in Alstom's GT24/GT26 architecture, a "sequential environmental" (SEV) combustor is added to the first-stage "environmental" (EV) combustor. It is introduced between the high and low pressure turbine stages, as sketched in Fig. 1.1. In the SEV combustor, the fuel is injected through a central fuel lance into the incoming flue gas as a jet-in-crossflow. In order to avoid the establishment of a diffusion flame at the injector, the fuel jet is surrounded by a concentric shielding air jet, which delays the ignition, such that the main heat release occurs at a well-defined location behind the area expansion.

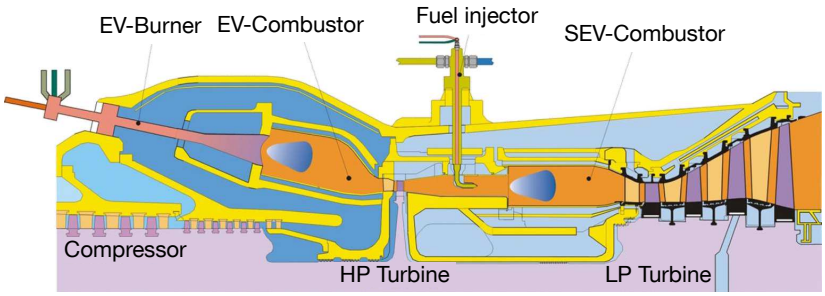

Figure 1.1: Schematic cut view of Alstom's GT24/GT26 gas turbine family (adapted from [35])

The corresponding thermodynamic cycle resembles a reheat steam cycle, which also features a second heat addition between two turbine stages. As can be seen from the T-s diagram in Fig. 1.2, such a sequential gas turbine concept allows to maximise the specific work for a given maximum turbine inlet temperature. The same specific work can thus be obtained at lower peak temperatures than in a conventional gas turbines; hence, reheat combustion systems offer an intrinsic advantage regarding NO_X emissions and turbine cooling [21, 39]. This applies to full load operation, and even more to part load, when the fuel supply is first reduced in the reheat combustor, whereas the primary chamber is run at its optimum design point. As one can see from Fig. 1.3, such an operation strategy allows to keep the NO_X emissions low over a wide load range. The low-load operation (LLO) capability is thus significantly enhanced through the use of a sequential combustion system.

The main reason for this is the fact that the reheat combustor is quite insensitive to load variations. While conventional, aerodynamically stabilised burners approach flammability limits in the part-load regime, the heat addition in the reheat combustors is stabilised through auto-ignition. This is due to the elevated temperatures of the flow coming out of the high pressure turbine, into which the secondary fuel stream is injected. The sensible enthalpy of the

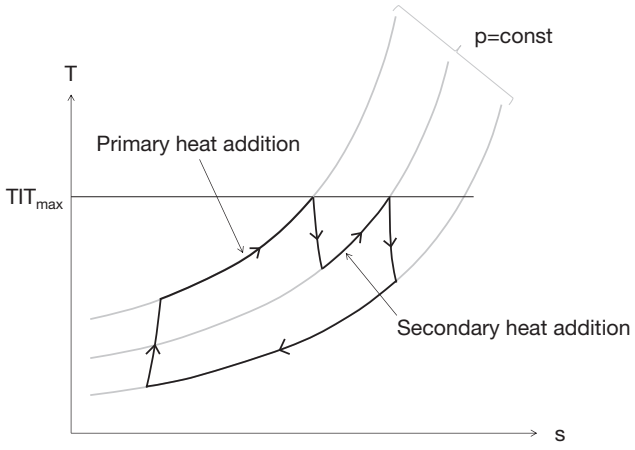

Figure 1.2: Schematic representation of a sequential gas turbine thermodynamic cycle in a T-s diagram

flow is sufficiently high to launch the pre-ignition reactions, which finally lead to heat release after a certain ignition delay. As will be explained in more detail in section 2.1.1, the flame stabilisation in such a setup highly depends on the local flow characteristics, i.e. on mixture distribution, rather than on global flow parameters, as e.g. the global equivalence ratio in the combustor. As a consequence, reheat combustion at part-load occurs similarly as at full-load conditions, and no noticeable increase in NO_X emissions occurs when reducing the fuel supply in the sequential combustor [35].

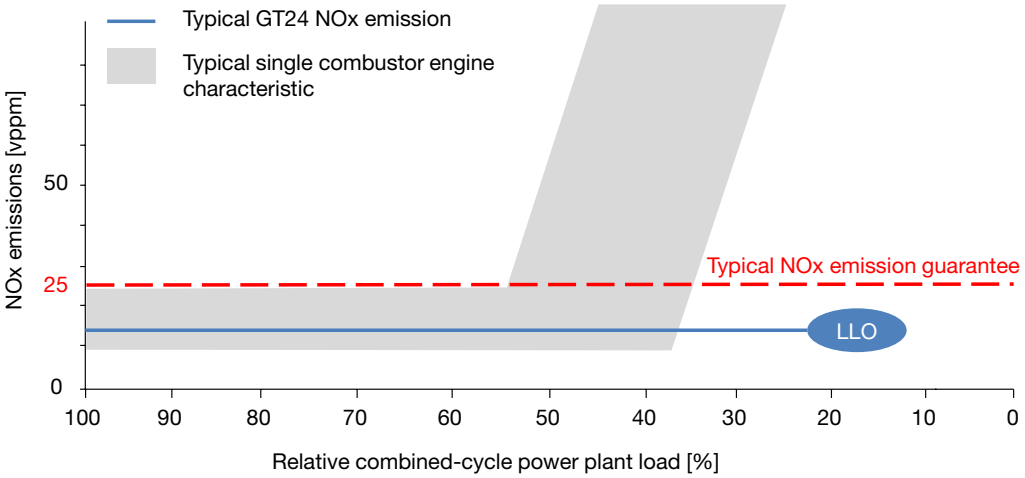

Figure 1.3: Schematic representation of combined-cycle power plant NOx emissions over relative load - Comparison between single and sequential combustion engine concepts (adapted from [100])

1.3 Introduction to thermoacoustics

First observations of thermoacoustic phenomena date back to the eighteenth century. Higgins reported experiments made in 1777 with a hydrogen flame placed in tubes of varying lengths, which produced ”many different tones”. His observations were published in 1802 in form of a letter attached to an article of Nicholson [80], who proposed possible physical explanations of the phenomena. Nicholson introduces the concept of flame dynamics, postulating that ”the intension and remission of the flame of the hidrogen”, i.e. flame surface variations, might cause the generation of sound.

Half a century later, Rijke [97] reports similar observations, but with a wire-gauze placed in a vertical tube. After sufficient heating of the gauze, either by a hydrogen lamp, a carbonic oxide flame, or an electric current, a strong tone, close to the fundamental harmonic of the tube, is observed. The strongest sound emission occurs when the gauze is placed at the quarter length of the tube. Rijke tries to explain the phenomenon by consecutive dilatations and contractions of the air due to heat addition and subtraction at the gauze and the tube walls, respectively.

A profound explanation is given later by Lord Rayleigh [96], who stated that, when a periodic pressure oscillation is in phase with an unsteady heat source, the coupling between the two leads to an amplification of the acoustic pressure wave.

In the 1930’s and 1940’s, thermoacoustics were for the first time investigated with respect to technical applications, since combustion instabilities had been found to cause severe structural damage to enclosed combustion systems. Indeed, a closed feedback loop is obtained when acoustic waves are amplified by the flame and reflected at the domain boundaries, leading to an exponential growth of the acoustic perturbations. Culick [19] gives an overview of these early works, which were mainly related to solid and liquid fuel rockets, but also to afterburners in jet engines. Fundamental work was done in the following decades, developing quantitative methods for the prediction of thermoacoustic stability problems, first in linear context for small perturbations, see e.g. Crocco and Cheng [16], and later also at higher oscillation levels considering non-linear gas dynamics, see e.g. the works of Culick [17, 18].

In gas turbine combustion, similar issues began to rise after the introduction of lean premix combustion systems in the 1990's, which allowed to significantly reduce NO_X emissions, but are more prone to thermoacoustic instabilities. The research was much driven by industrial needs to develop prediction tools that allow a reliable layout of stable combustion systems. As a result many efforts have been provided on low-order-modeling, representing the combustor as an acoustic network element with the flame acting as a source, see e.g. Deuker [20] or Dowling [22]. These works are generally based on the classical "n-τ" model for the flame transfer function introduced by Crocco and Cheng [16]. In industrial practice, the n-τ model parameters are determined experimentally, see e.g. Paschereit et al. [86], numerically using computational fluid dynamics simulations, as done e.g. by Deuker [20] and Polifke et al. [94], and analytically, see e.g. Schuermans et al. [106] and Sattelmayer [99].

In recent years, a broadening of topics has been observed in thermoacoustic research. Some of the works aimed e.g. at deepening the physical understanding of flame feedback mechanisms, in particular those linked to axial velocity perturbations, see the works of Palies et al. [85], Tay et al. [115], or Blumenthal et al. [5]. Other works are related to the development of prediction methods for non-linear and non-normal flame dynamics, see the works of Noiray et al. [81] or Balasubramanian and Sujith [3]. Moreover, flame dynamics linked to low-frequency azimuthal velocity perturbations have also received growing interest, see Hauser et al. [37] and O'Connor and Lieuwen [82, 83]. The general trend therefore goes to extending thermoacoustic theory to a wide range of regimes and excitation cases.

1.4 Aim and scope of the present work

The present work fits well into this context, since it deals with high-frequency, transverse acoustic mode stability in reheat combustors, which had not been investigated extensively before. It partly builds up on an analytical study by Ni et al. [79], who proposed a model for longitudinal mode stability prediction in reheat combustors. The present research work has also been conducted in parallel with experimental studies investigating high-frequency transverse instabilities in premix swirl combustors, see the works of Schwing et al. [108–111].

As one can conclude from the basic description given above, sequential combustors use a type of flame stabilisation very different from the one usually applied in conventional, swirl stabilised burners. Hence, the next chapter will first give an overview on the fundamentals of turbulent, lifted flames stabilised by auto-ignition. Possible dynamic effects in such flames will be discussed, which could be of importance regarding the thermoacoustic stability of sequential combustors. Chapter 3 is related to the computational tools and methods that are used in the present work: methods for the calculation of lifted auto-ignition flames and their dynamics, incl. chemical kinetics, as well as tools for thermoacoustic stability prediction.

The detailed investigation of combustion dynamics and possible thermoacoustic feedback mechanisms is the subject of chapters 4 to 7. This goes on with an increasing degree of physical and modelling complexity, starting from the analytical modelling of a low-order, simplified case (chapter 4) and ending with the transient, 3D CFD calculation of realistic combustor configurations, with perfect (chapter 5) and technical premixing (chapter 6). With this combination of approaches and the use of advanced post-processing techniques, the feedback effects introduced in chapter 2 will be investigated, in order to understand why sequential combustors can run into pulsation problems when leaving the design operation window. Chapter 7 then translates the knowledge gained on thermoacoustic feedback in reheat combustors into a quantitative description that can be used for stability analysis, and discuss its potential application in the industrial design process. A final summary and a wider outlook are given in chapter 8.

Throughout this work, the discussion is centred on the case of sequential combustion as it is used in practice by Alstom. Recently, similar, staged combustion concepts have been investigated by various research groups [28, 38, 103], partly in cooperation with gas turbine manufacturers. These concepts also include a secondary fuel injection, which is however located before the high pressure turbine, directly downstream of the first stage. This results in slightly different thermodynamic conditions than in a sequential combustor (higher temperature and pressure). Nevertheless, the physical effects involved are similar, in particular a flame stabilisation due to auto-ignition. Thus, the physical description and the methods developed in the present work should be applicable as well to other combustor concepts with preheat temperatures near or above the auto-ignition threshold.

2 Fundamentals of Flames and Combustion Dynamics

The present chapter introduces important theoretical concepts regarding flame stabilisation mechanisms and combustion dynamics, which are constituting the state-of-the-art for the present research work. Subsequently, a more detailed description of the objectives of this work will be given, by identifying the flame feedback mechanisms that are of interest, and by underlining the need for a local analysis of heat release rate fluctuations caused by high-frequency acoustic modes.

2.1 Steady flame characteristics

The sequential combustion concept was introduced in the previous chapter by describing its integration into the gas turbine architecture and its main advantages. In the present section, more details shall be given on the different elements constituting the reheat combustor and on the physical effects governing the heat release. Various publications by Alstom and cooperating research institutes are available in the literature and provide insight into the combustor design and the combustion process [10, 21, 26, 27, 35, 52, 77, 95].

A reheat combustor, as it is used in Alstom's GT24/GT26 gas turbine series, is composed of three main elements:

1. Vortex generators shaped as delta wings, which lead to the formation of counter-rotating vortex pairs,
2. A fuel lance placed on the burner axis with concentric injection holes of fuel and shielding air, located in between two vortex pairs,
3. An area expansion from the burner into the combustion chamber, which leads to the formation of recirculation zones close to the liner walls.

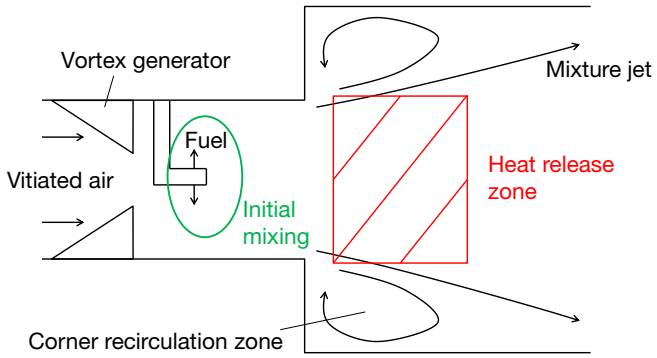

Figure 2.1: Sketch of Alstom's SEV combustor

The layout of these elements is shown schematically in Fig. 2.1. A specific orientation of the injector holes with respect to the vortex generators allows to obtain a high penetration depth of the fuel jet into the vitiated air stream, despite the high flow velocities of the main stream. This allows a fast mixing of the streams before ignition onset and thus guarantees low emission levels. This injection concept was found to be more efficient than other designs, see Eroglu et al. [26].

Recently, a novel injection concept was presented by Poyyapakkam et al. [95]. It aims at extending the fuel flexibility toward higher hydrogen contents, which significantly increase the fuel reactivity. In order to avoid flashback and subsequent damage to the fuel lance, the fuel injection is directly integrated into the vortex generators. For the remaining part of this work, the discussion will be centred on the conventional injection through the fuel lance. Nevertheless, the physical processes involved are similar for both concepts, and the results from this work are thus applicable to the other injection system as well.

The exhaust gas stream coming from the high pressure turbine is generally referred to as the *hot gas* stream. It enters the reheat combustor at temperatures around 1000°C [95]. Downstream of the injector holes, a so-called *ternary mixing* process takes place, between hot gas, fuel, and shielding air. While the fuel temperature is close to ambient conditions, the shielding air is at a medium temperature level, as it is extracted at an intermediate compressor stage. The sensible enthalpy of the hot gas is sufficiently high to initiate the formation of chemical radical species, which lead to auto-ignition delay times of a few milliseconds. The global flame stabilisation in a reheat combustor is

hence ensured by auto-ignition, leading to a so-called *lifted flame*, which is located downstream of the fuel injection.

2.1.1 Turbulent lifted flames stabilised by auto-ignition

The flame in a reheat combustor can thus be characterised as a turbulent, non-premixed lifted flame. Simplified configurations of this kind have been studied extensively in academic research, mostly with a fuel jet in oxidiser co-flow.

However, one needs to make a distinction with respect to the oxidiser temperature level. Many investigations have for instance been conducted with a cold oxidiser stream, as described in a review article written by Lawn [63]. These setups need an external ignition source to spark the flame, which then stabilises at a position downstream of the fuel injection. Lawn points out that the flame stabilisation in such setups requires a balance between convection and upward propagation of heat. Flame propagation through a stratified mixture is therefore the main stabilising mechanism, in particular for elevated jet velocities and consequently large lift-off heights. Such setups are therefore not appropriate for describing the processes in reheat combustors and are not considered any further in the present work.

Co-flow configurations with mixing between hot, vitiated oxidiser and cold fuel do, however, resemble reheat combustors. In distinction to setups with cold oxidiser co-flow, they do not rely on external ignition.

The probably most-cited auto-igniting configuration is the so-called *Cabra flame*, which was first investigated in an experimental study by Cabra et al. [12]. Different research groups conducted various studies on this setup, using both experimental [11, 32] and numerical techniques [33, 34]. In recent years, the setup installed at Cambridge University by Markides and Mastorakos received a lot of attention, as it shows the various regimes that auto-igniting setups can present as a function of the oxidiser temperature and the stream velocity. Indeed, when gradually varying these parameters, various distinct flame appearances were observed:

1. At low temperatures: No flame regime,

2. At medium temperatures: Random-spots regime,
3. At elevated temperatures and low stream velocities: Flashback regime,
4. At elevated temperatures and high stream velocities: Lifted flame regime.

To explain the different regimes, one has to consider that auto-ignition in jet flows requires a balance between various physical processes: First, fuel and oxidiser have to mix in order to obtain reactive mixture regions. There, chemical radical species are formed at a rate mainly governed by the local temperature. These need to be accumulated up to a specific level in order to launch the chain-branching reactions responsible for ignition and heat release. The build-up time, during which the temperature rise is very low, is generally referred to as *induction phase* (see Fig. 2.2). This takes place in the mixing layer between the two streams, where strong composition gradients exist, leading to intense diffusive processes. Radical species are therefore transported away from the reactive regions, the build-up of the radical pool is delayed. The actual auto-ignition length finally depends on the build-up time, the size of reactive mixture regions, and the convection of the mean flow.

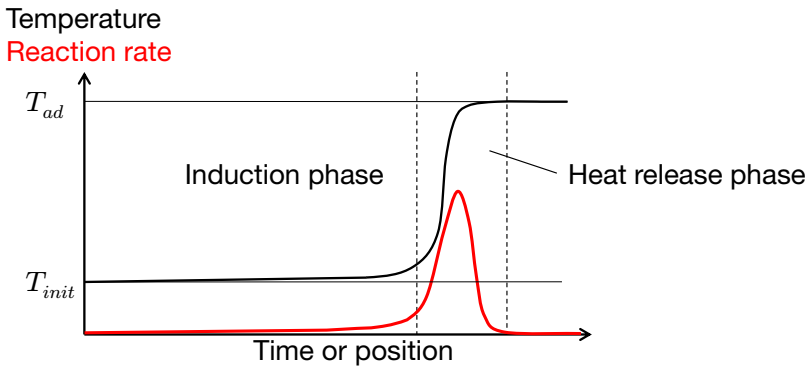

Figure 2.2: Typical temperature evolution during ignition process with indication of induction and heat release phases (adapted from [9])

In the limit case of the no-flame regime, the chemical formation rates are not high enough to counterbalance the cross-stream species diffusion and the fuel leaves the domain unburnt.

The random-spots regime is characterised by the intermittent appearance of auto-ignition spots or *kernels*, because the balancing between mixing, reaction, and diffusion is affected by turbulent fluctuations. Hence, the kernels

appear at positions fluctuating around a mean location, which depends on inflow conditions like jet velocity, temperature and turbulence level, as will be discussed later. As pointed out by Markides and Mastorakos [69], the ignition kernels grow in size while being convected downstream, before finally dying out. The initial kernel formation by auto-ignition is therefore followed by a flame propagation into the unburnt mixture, which however quenches at a certain point. Nevertheless, the random-spots regime results as "a statistically stable situation" [69]; the kernel formation frequency is observed to increase with the oxidiser temperature.

When increasing the temperature further, two different regimes may appear as a function of the stream velocities. At low velocities, the first kernel appearance is immediately followed by flame flashback and the establishment of a diffusion flame. The flame propagation from the initial kernel is hence outweighing the convective mixture transport.

The lifted flame regime observed for higher velocities is the most relevant for technical applications like reheat combustors, since it allows a flame stabilisation at a position sufficiently downstream to not damage the injector. Under these conditions, the Cambridge setup behaves similarly to the one investigated by Cabra and co-workers, as pointed out Markides and Mastorakos [69]. It can be viewed as a continuation of the random-spots regime, i.e. a case with very high formation frequency of kernels, which get distorted and finally lead to the observed lifted flame appearance, see Gordon et al. [32]. Transport budget calculations made by Gordon et al. [33, 34] on the Cabra flame setup indicate that flame propagation only plays a minor role in flame stabilisation.

However, in reheat combustors, flame propagation through forced flow recirculation further stabilises the combustion process, in the corner recirculation zones behind the area expansion. The academic test cases mentioned before do not feature such a forced recirculation of combustion products. Hence, flame propagation needs to be considered to a much larger extent for reheat combustors. Nevertheless, auto-ignition still plays the major role in flame stabilisation because of the high flow velocities.

The main characteristics of kernel formation shall be described further in the following. For a binary mixture case, the mixture fraction expresses the fuel content in the inert mixture:

$$Z = \frac{Y_F}{Y_F + Y_{Ox}} \tag{2.1}$$

with Y_F and Y_{Ox} denoting the mass fractions of fuel and oxidiser, respectively. For the applications of interest, the oxidiser temperature is far higher than that of the fuel. As a consequence, when adding more oxidiser, i.e. making the mixture leaner, the temperature of the unburnt mixture increases. Kinetic reaction rates $\dot{\omega}$ show an exponential temperature dependence, which is described by the Arrhenius equation

$$\dot{\omega} \propto \mathscr{A}\, T^b \exp\left(-\frac{E_a}{RT}\right) \tag{2.2}$$

using the pre-exponential factor $\mathscr{A}$, a temperature exponent b, and the activation energy of the reaction E_a.

Commonly used correlations for auto-ignition delay times, as e.g. given by Spadaccini and Colket [114], use a similar ansatz :

$$\tau \propto \exp\left(\frac{E_a}{RT}\right) \tag{2.3}$$

with a value of $E_a/R = 22500K$ when dealing with methane-air mixtures. As a result, the auto-ignition delay time is halved when increasing an initial mixture temperature of 1300 K by only 54 K, i.e. by less than 5%.

For mixtures of hot oxidiser and cold fuel, the highest reactivity, and thus the shortest ignition delays, are obtained at lean conditions. The mixture dependence of the ignition delay is shown in Fig. 2.3 for a mixture of methane at 300 K with vitiated air at 1300 K and a pressure of 18 bar. The minimum ignition delay is clearly located on the lean side and determines the so-called *most reactive mixture fraction* Z_{MR}.

As Mastorakos [70] pointed out in his extensive review on ignition phenomena, auto-ignition kernels preferably appear close to the most reactive mixture fraction isosurface in a flow. Moreover, he mentions that the history of scalar dissipation rate χ strongly influences the kernel formation. This quantity de-

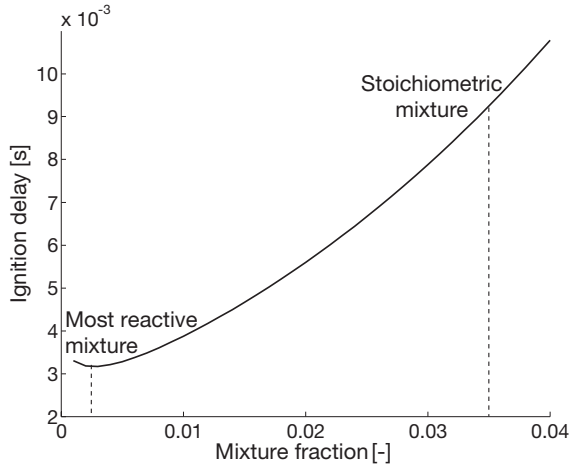

Figure 2.3: Mixture dependence of ignition delay for pairing of methane (300 K) and vitiated air (1300 K) at elevated pressure conditions (18 bar). Results from detailed chemistry calculations.

pends on mixture gradients and is taken as a measure for diffusive fluxes in the flow. For turbulent flows with a turbulent viscosity ν_t, it is expressed by:

$$\chi = \nu_t \left(\frac{\partial Z}{\partial x_i} \right)^2 . \tag{2.4}$$

The combined influence of mixture fraction and scalar dissipation rate in turbulent flows allows to quantify the balance act between radical formation and diffusion described above: If high dissipation rates appear close to the most reactive region, the species formed are diffusing into less reactive regions and the build-up of radicals is delayed. The conditional value of the scalar dissipation on the most reactive mixture fraction is thus of high relevance, i.e. $\langle \chi | Z_{MR} \rangle$, as explained by Mastorakos [70]. For illustration, Fig. 2.4 shows results of 2D DNS autoignition calculations by Hilbert and Thévenin [40], where the relevance of the conditional scalar dissipation is very obvious. This picture shows a snapshot at a given time; when taking a scenario evolving in time, the appearance of intermittent ignition spots becomes conceivable, distributed along the Z_{MR} isosurface and dependent on the scalar dissipation field, which, in turbulent flows, is subjected to strong temporal and spatial fluctuations. As will be elaborated later, the total available Z_{MR} isosurface area also plays an important role, since an increasing size of highly reactive regions increases the probability of kernel formation.

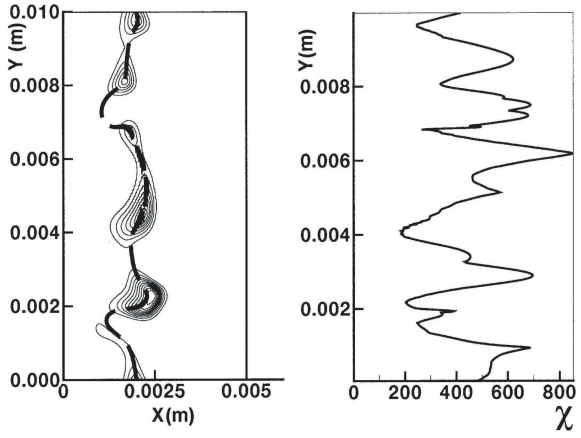

Figure 2.4: Left: Location of auto-ignition kernels (indicated by heat release rate contours) along Z_{MR} isoline in 2D-DNS. Right: Corresponding instantaneous scalar dissipation rate, indicating the coincidence of auto-ignition kernels and low scalar dissipation regions (from [40]).

The impact of operation parameter variations can be explained within the scope of the general flame behaviour described above. With respect to technical applications, the following parameters may be of interest:

- Oxidiser temperature
- Oxidiser mass flow/global equivalence ratio
- Turbulence characteristics

Variations in oxidiser temperature strongly affect the chemical reaction rates due to the exponential temperature dependence of the Arrhenius expression. However, the mixing field will not be significantly changed. As a consequence, when increasing the oxidiser temperature, the ignition delay is shortened. This results in an upstream displacement of the flame and an increasing formation frequency of ignition kernels. These observations were made experimentally for hydrogen and n-heptane by Markides et al. on the Cambridge setup [68, 69]. Numerical calculations do also predict the same behaviour, as was shown by Kulkarni et al. [57, 59].

The same authors also conducted studies with the Cambridge setup on the influence of the bulk mean velocity on auto-ignition length. For this parameter variation, the equal fuel and air jet velocities were varied conjointly. If

only the chemical time scale were relevant, the flame position would scale linearly with the velocity. However, this is not the case, since the increased turbulent diffusivity strengthens the delaying action of the scalar dissipation. This finally leads to a disproportionate downstream movement of the flame location. Experimental measures do for instance indicate a 71% increase in flame position for a velocity increase of only 30% [68]. In his numerical work, Kulkarni showed that this was not linked to changes in the global mixing field, but to higher scalar dissipation levels, as postulated by Markides [68].

Markides and Mastorakos also studied the impact of non-equal jet velocities [69]. They showed that, for a constant air velocity, variations in fuel velocity lead to a proportional change in auto-ignition length. In other words, the ignition delay time is not significantly altered by the fuel velocity. The global mixing ratio ($\dot{m}_{Ox}$ vs. $\dot{m}_F$) therefore does not have any significant impact on the ignition delay time when the co-flow conditions remain unchanged. This fits well to the general behaviour, which states that the ignition heavily depends on the scalar dissipation rate close to the most reactive mixture fraction. As the latter is located on the lean side, variations of the fuel stream have a small impact, contrarily to variations of the co-flow.

The impact of turbulence characteristics of the co-flow, i.e. turbulent intensity and integral length scale, has long been discussed in a contradictory manner in the literature. Within the scope of the present research work, a detailed parameter study was conducted regarding this aspect and the results have recently been published by Kulkarni et al. [59]. Therein, it was shown that the dependence is non-monotonous, depending on the ratio between the turbulent time scale τ_t in the co-flow and the reference ignition delay time τ_{MR} at the most reactive mixture fraction. This ratio can be expressed as an auto-ignition Damköhler number Da_{AI}:

$$\mathrm{Da}_{AI} = \frac{\tau_t}{\tau_{MR}}. \tag{2.5}$$

The turbulent time scale τ_t in the co-flow is defined as the ratio between turbulent length scale l_t and turbulence intensity U' applied at the inlet. Its impact on the auto-ignition length is investigated by means of two distinct parameter variation studies, applying different values of l_t and U'.

In both studies, it is observed that, for cases of weak turbulence (Da_{AI}>1), any decrease in turbulent time scale leads to a shorter ignition length. However,

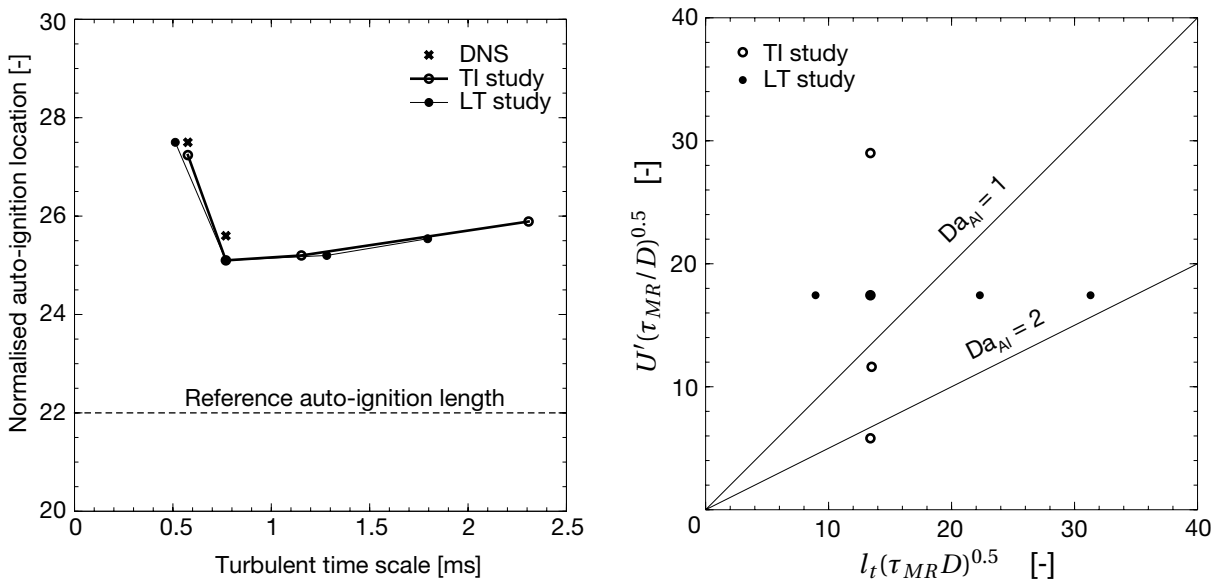

Figure 2.5: Left: Turbulence influence on auto-ignition delay in jet-in-coflow configuration. Results from systematic variations of turbulence intensity (TI study) and turbulent length scale (LT study) in LES as well as from DNS calculations [54] are shown. Right: Regime diagram for turbulence-chemistry interaction in auto-igniting setups (both from [59])

this holds true only up to a certain point, which lies close to Da_{AI}=1. If the turbulence time scale is further reduced, the ignition length starts to increase again. The simulation results showing the minimum auto-ignition length are depicted in the left plot of Fig. 2.5.

An explanation of the non-monotonous evolution is proposed in [59]. It also uses the concept of the conditioned scalar dissipation rate, but further considers the available surface of most reactive mixture fraction. This is needed to explain the non-monotonous behaviour of the auto-ignition length, since the scalar dissipation rate increases steadily when the turbulent time scale is reduced. At the same time, it is found that the surface of most reactive mixture fraction increases unsteadily. A strong increase is only noticed when τ_t is still large, while the most reactive mixture fraction surface remains nearly constant when τ_t comes down to low values.

Physically speaking, it is argued that in weak turbulence, the total radical formation is more aided by the increase in Z_{MR} surface than it is inhibited by the increased scalar dissipation rate. This corresponds to the right branch in the curve for the auto-ignition length shown in Fig. 2.5. In strong turbulence, any

further decrease in turbulent time scale inhibits the radical formation by diffusion more strongly than it creates reactive mixture regions; this explains the left branch of the curve.

The right side of Fig. 2.5 locates the operating points investigated within a non-dimensional Damköhler representation of the turbulence-chemistry interaction, similar to the one proposed by Borghi [6] for premixed propagating flames. As in the premix flame diagram, the axes denote the turbulent time scale and turbulence intensity, put into relation with the chemical time scale and the laminar diffusivity D, in a way that the Damköhler isolines appear as straight lines starting from the origin. Analogously to the "corrugated/wrinkled flame regime" in premix combustion, turbulence is beneficial to the reaction in the lower right part (Da_{AI}>1), while the opposite is the case at low Damköhler numbers, hence equivalent to the "broken reaction zone" regime of premix flames.

In summary, turbulent auto-ignition flames show a strong dependence on the conditions in the oxidiser flow. This is mainly due to the fact that auto-ignition kernels appear on the lean side, and are thus only weakly influenced by the characteristics of the fuel stream. The temperature of the hot gas stream can therefore be considered as the main influencing parameter, due to the exponential formulation of the Arrhenius expression. Moreover, both mean and fluctuating velocity affect the ignition delay.

The previous analysis of influence parameters indicates how auto-igniting setups depend on stationary operating conditions. When dealing with thermoacoustics, one needs to investigate the dynamics of the flame, i.e. how the flame reacts to acoustic perturbations. As explained in section 2.3.1, thermoacoustic instabilities can only occur if a periodic coupling occurs between the flame and the acoustic flow perturbations. The previous analysis will help to understand the dynamics of auto-ignition processes.

Moreover, for technical reheat combustors, it is also necessary to consider flame propagation effects which occur in the shear layer region between the entering flow and the recirculation zones. Turbulent propagating flames have received far more attention in the literature than auto-ignition flames. They are thus discussed only very briefly in the next subsection, mainly in order to underline the differences between the two flame types.

2.1.2 Turbulent premixed flames stabilised by flame propagation

Auto-ignition flames can be described by fuel particles injected into a stream of hot oxidiser. While they travel downstream and mix with the oxidiser, pre-ignition reactions take place until a sufficiently high radical concentration is present to launch the heat release reactions. The previous section showed that the entire mixing history is of importance for the occurrence of ignition.

For propagating flames the situation is different. Generally, the temperature levels on the unburnt side are far lower than for auto-igniting flames, such that no significant reactions occur before the flame. Hence, flame propagation depends solely on a local equilibrium of reactive, diffusive, and convective processes. The chain-branching reactions can only be launched, once a sufficient amount of heat has been transferred from the burnt products to the fresh mixture. Propagation flames are thus always characterised by the presence of a preheat zone, in which diffusive processes take place, and a, generally much thinner, reaction zone, in which the heat release takes place. The flame structure is shown schematically in Fig. 2.6.

In the laminar case, the heat diffusion is governed by the molecular diffusivity in the mixture, the corresponding propagation velocity of the flame is described by the laminar flame speed S_l. In a first approximation, it depends on the thermal diffusivity D_u of the unburnt mixture and the chemical reaction rate $\dot{\omega}$, as expressed by the relation of Mallard and Le Châtelier [67]:

$$S_l = \sqrt{D_u \dot{\omega}_F}. \tag{2.6}$$

In turbulent flows, the molecular diffusion is aided by turbulent transport processes. These can interact with the flame in different ways, depending on the relative chemical and turbulent time scales. Hence, in cases of weak turbulence, vortices mostly wrinkle the flame, which locally still behaves as a laminar flamelet. The turbulent burning velocity is in these cases increased over the laminar flame velocity by enlarging the available flame surface. For more intense turbulence and smaller vortical structures, the diffusive transport processes within the preheat zone are getting enhanced by the smallest turbulent scales, what generally further promotes the reaction. However, in cases of very intense turbulence, local extinction effects come into play, when chemical reaction rates cannot keep pace with the fast turbulent mixing. More details

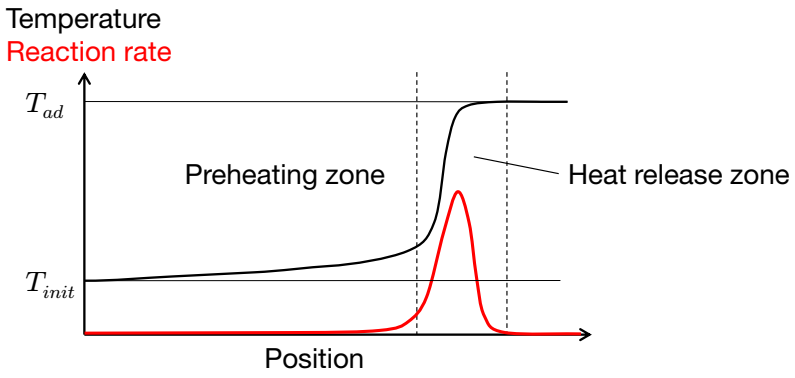

Figure 2.6: Structure of a premixed propagation flame (adapted from [41, 120])

about turbulence-chemistry interaction can be found in [6, 87, 91], including the typical graphical representation of the various regimes.

Because of the high inlet temperatures and the presence of large recirculation zones, both auto-ignition and flame propagation play a role in flame stabilisation in reheat combustors. The simulation tools used and the description of heat release dynamics developed in the remainder of this work thus need to be applicable to both types of flame stabilisation.

2.2 Unsteady flame characteristics

The unsteady flame behaviour is of particular importance when considering the emergence of thermoacoustic pulsations. As will be explained in detail in the next subsection, flames can act as acoustic sources, when a positive coupling occurs between acoustic pressure fluctuations and heat release variations. Within this work, mean quantities and acoustic fluctuations of a random parameter β are denoted $\overline{\beta}$ and β', respectively; one can generally write $\beta = \overline{\beta} + \beta'$.

Understanding the combustion dynamics is a prerequisite to correctly predict the occurence of an instability. In the present subsection, various mechanisms will be presented, which can lead to temporally and spatially fluctuating heat release rates, for both auto-ignition and propagation flames.

In previous studies, attention was mostly paid to the instability of longitudinal and circumferential modes in premixed configurations stabilised by flame

propagation, since this kind of thermoacoustic pulsations caused the most concerns in the industrial development of annular lean premix gas turbine combustors. Fundamental work on premix flame dynamics was performed by various research groups, both experimentally and numerically, as e.g. Dowling et al. [22], Schuermans et al. [106], Lieuwen [64], Polifke et al. [93, 94], Sattelmayer [99], or Schuller et al. [107].

The frequencies of longitudinal and circumferential modes typically considered in gas turbine combustors are rather low, and the flame can be regarded as compact with respect to the acoustic wavelength. Hence, in classical thermoacoustic theory, only temporal variations of the overall heat release rate are taken into account. Such fluctuations of heat release rate can be caused by different effects:

- Variations of the fuel mixture fraction Z, caused by velocity and density fluctuations in the fuel supply line [45, 46, 65, 66, 99].
- Variations of the density ρ at the flame position [106].
- Variations of the flame surface A, created e.g. by coherent flame wrinkling [107] or swirl fluctuations [55, 85, 115],
- Variations of the consumption speed S_c, possibly caused by modulations of the mixture fraction [45, 46], and/or changes in thermodynamic state. The latter effect is however mostly neglected, with the notable exceptions of the works done by Clavin et al. [14], McIntosh [72], Rook et al. [98], Wu et al. [121], and Schmidt and Jimenez [101].

The relevance of these variations becomes obvious after writing down the relation governing the heat release rate $\dot{Q}$ of a premix flame:

$$\dot{Q} = Z \Delta h_F^\circ \rho_u A S_c \tag{2.7}$$

with Δh_F° and ρ_u denoting the constant reaction heat per mass of the fuel and the density of the unburnt mixture, respectively.

The resulting heat release rate fluctuations can thus be expressed by the following expression in the linear context:

$$\frac{\dot{Q}'}{\overline{\dot{Q}}} = \frac{Z'}{\overline{Z}} + \frac{\rho_u'}{\overline{\rho}_u} + \frac{A'}{\overline{A}} + \frac{S_c'}{\overline{S}_c}. \tag{2.8}$$

For the numerical prediction of system stability, these fluctuation values have to be expressed as a function of acoustic fluctuation values (typically velocity and/or pressure) and coupled with an acoustic solver, as will be explained in chapter 3.3.

When dealing with harmonic fluctuations, it is very convenient to introduce a complex notation. For example, the heat release rate fluctuations $\dot{Q}'$ are defined as the real part of the complex value $\check{\dot{Q}}$:

$$\dot{Q}' \equiv \Re\left(\check{\dot{Q}}\right) = \frac{1}{2}\left(\check{\dot{Q}} + \check{\dot{Q}}^*\right) \tag{2.9}$$

with $\check{\dot{Q}}^*$ denoting the complex conjugate of $\check{\dot{Q}}$. Complex flame transfer functions (FTFs) are commonly used for linking heat release rate fluctuations to acoustic terms. For example, harmonic heat release and flame area fluctuations at the angular frequency ω can be expressed as a function of the corresponding acoustic velocity in the complex space:

$$\left.\frac{\check{\dot{Q}}}{\overline{\dot{Q}}}\right|_{\omega,A} = \left.\frac{\check{A}}{\overline{A}}\right|_{\omega} = \left.\frac{\check{u}}{\overline{u}}\right|_{\omega} \mathrm{FTF}_{u',A}(\omega) \tag{2.10}$$

with

$$\mathrm{FTF}_{u',A}(\omega) = |\mathrm{FTF}_{u',A}|(\omega)\exp\left(i\phi_{u',A}(\omega)\right) \tag{2.11}$$

and $|\mathrm{FTF}_{u',A}|(\omega)$ and $\phi_{u',A}(\omega)$ denoting the gain and the phase of the flame response due to area fluctuations, respectively. The location of the corresponding velocity fluctuation measurement needs to be defined according to the problem.

The present work aims at extending the thermoacoustic theory to high-frequency transverse modes and to combustion processes typical for reheat combustors with high oxidiser temperatures. The first point mainly leads to a non-compact flame with respect to the acoustic wavelength. Indeed, the first transverse mode stretches over half a wavelength between the liner walls. Since flames can develop nearly over the whole combustor height, i.e. in swirled flows, it becomes clear that the scale separation made for longitudinal modes is not valid anymore. This is illustrated in Fig. 2.7.

As a consequence, heat release rate fluctuations have to be accounted at a local scale, using the volumetric heat release rate $\dot{q}$. It is related to the total heat release rate $\dot{Q}$ by a simple volume integration: $\dot{Q} = \int_V \dot{q}\,dV$. Spatiotemporal

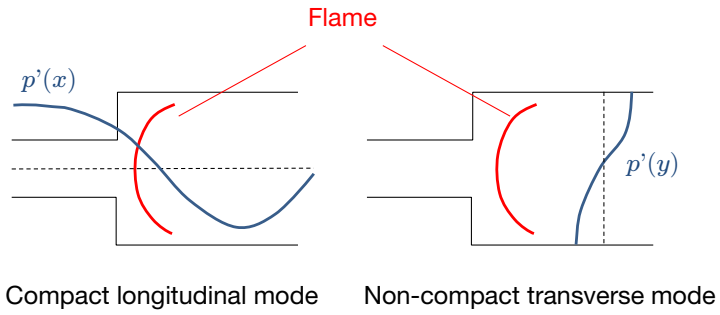

Figure 2.7: Illustration of flame compactness with respect to longitudinal and transverse acoustic modes

fluctuations of the heat release rate now also have to be taken into account. Transverse velocity fluctuations lead for example to a periodic displacement Δ of the flame in transverse direction. At the local scale this results in noticeable heat release rate fluctuations. Such a behaviour was reported by Schwing et al. [109] and Méry et al. [74]. The former group further proposed an analytical model which allows to quantify the thermoacoustic feedback related to such displacement effects in thin flames, which will be extended in the present work.

At a local scale, the concept of flame consumption speed is less appropriate, even more so if the description shall also be valid for auto-ignition problems. By introducing a mass-specific heat release rate $\dot{\omega}_h$, one can write

$$\dot{q} = \rho \dot{\omega}_h \tag{2.12}$$

and express the local fluctuations as follows:

$$\frac{\dot{q}'}{\overline{\dot{q}}} = \frac{\rho'}{\overline{\rho}} + \frac{\dot{\omega}'_h}{\overline{\dot{\omega}_h}}. \tag{2.13}$$

Whilst the density appears as for compact flames, the second term on the RHS of Eq. (2.13) now includes a multitude of fluctuation effects. These can be mixture fraction, chemical rate, flame area variations, and/or flame displacement. In chapter 5, a theoretical decomposition of the latter term will be derived, which can be applied to simulation results in order to distinguish between individual feedback contributions.

It was mentioned that acoustic variations of pressure and temperature are generally considered to have a negligible direct impact on chemical reaction

rates in propagation flames. This argument is revised in the present work since higher inlet temperature levels are considered, leading to auto-ignition of the mixture. Since auto-ignition processes present a very high sensitivity in particular to temperature, acoustic variations are expected to strongly alter chemical reaction rates. As a linear approximation, the temperature variations can be directly derived from the acoustic pressure level when assuming an isentropic state change:

$$\frac{T'}{\overline{T}} \approx \frac{\gamma - 1}{\gamma} \frac{p'}{\overline{p}} \tag{2.14}$$

with the isentropic exponent γ. In the remainder of this work, acoustic pressure variations will always imply both pressure and temperature fluctuations for convenience. Hence, the reader shall keep in mind that, whenever the pressure impact on auto-ignition kinetics is mentioned, it is rather a temperature impact on the kinetics. A significant part of the present work investigates this influence of pressure waves on auto-ignition and heat release, see chapter 4.

In summary, Fig. 2.8 illustrates the various unsteady flame effects which are expected to occur in combustors with high oxidiser temperatures and subjected to high-frequency modes. Whether this lead to a positive thermoacoustic feedback depends on the phase information of heat release rate and pressure signals, as will be described in a quantitative manner in the following.

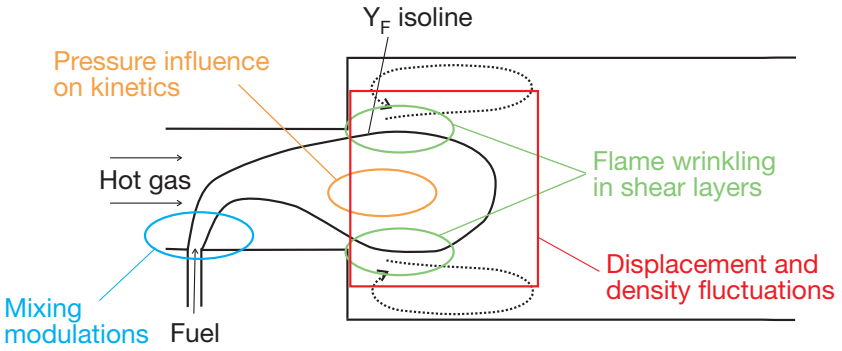

Figure 2.8: Illustration of flame dynamics possibly induced by transverse acoustic modes in reheat combustors

2.3 Thermoacoustic feedback

2.3.1 Rayleigh index

Classical thermoacoustic theory relies on the physical explanation given by Lord Rayleigh [96], which has already been introduced earlier. The feedback behaviour can be quantified in terms of the so-called *Rayleigh index* (RI), which can be defined as follows:

$$\mathrm{RI} = \int_V \int_0^{\mathcal{T}} p'(\vec{x},t)\,\dot{q}'(\vec{x},t)\,dt\;d\vec{x}. \tag{2.15}$$

with $\mathcal{T} = 2\pi/\omega$ denoting the period of oscillation. From that definition, it follows that a positive value of the Rayleigh index is obtained when pressure and heat release rate oscillations are in phase. A local Rayleigh index $\mathrm{ri}(\vec{x})$ can as well be expressed using

$$\mathrm{ri}(\vec{x}) = \int_0^{\mathcal{T}} p'(\vec{x},t)\,\dot{q}'(\vec{x},t)\,dt. \tag{2.16}$$

In its general formulation, the Rayleigh index is expressed as a spatial integral over the considered domain. For compact flames, the heat source can be considered as a point source at position $\vec{x}_f$ and the corresponding Rayleigh index can be written as:

$$\mathrm{RI} = \int_0^{\mathcal{T}} p'(\vec{x}_f,t)\,\dot{Q}'(t)\,dt. \tag{2.17}$$

The combination of Eqs. (2.8) and (2.17) can be considered as state-of-the-art in the development of lean premix gas turbine combustors, and allows accurate treatment of low-frequency longitudinal and circumferential modes. The flame-acoustics coupling in such configurations can thus be expressed as the superposition of four flame dynamic mechanisms, analogously to Eq. (2.8):

$$\mathrm{RI} = \mathrm{RI}_Z + \mathrm{RI}_\rho + \mathrm{RI}_A + \mathrm{RI}_{S_c}. \tag{2.18}$$

2.3.2 Feedback to transverse acoustic modes

For transverse modes, the non-compact formulation of the Rayleigh index given by Eq. (2.15) has to be used. Analogously to the decomposition of the compact Rayleigh index made before, one could split the non-compact one

into two parts, following the decomposition made for the local heat release rate fluctuations in Eq. (2.13).

However, Schwing et al. [109] proposed an analytical model for the feedback caused by the periodic displacement $\vec{\Delta}$ of a very thin flame, yielding the following Rayleigh index contribution:

$$\mathrm{RI}_{\Delta,\text{Schwing et al.}} = \iiint \int_0^{\mathcal{T}} p'(\vec{x}+\vec{\Delta},t)\overline{\dot{q}}(\vec{x})\,dt\,d\vec{x}. \tag{2.19}$$

This relation describes the feedback caused by the spatiotemporal fluctuations due to the flame displacement, which is positive if the flame is predominantly displaced toward regions with positive acoustic pressure.

This separate consideration of flame displacement leads to the following decomposition of the Rayleigh index:

$$\mathrm{RI} = \mathrm{RI}_\rho + \mathrm{RI}_{\dot{\omega}} + \mathrm{RI}_\Delta. \tag{2.20}$$

The first and the last terms correspond to the feedback of density and displacement, while the middle term gathers all remaining feedback effects, which can generally be expressed as temporal fluctuations of the mass-specific reaction rate. It is a priori not straightforward to clearly distinguish between the effects when dealing with actual flow data. This can be considered as one of the main achievements of the present work: in chapter 5 a formalism is proposed, which allows to decompose local heat release rate fluctuations into distinct contributions and thus to quantify individual feedback contributions. This further allows to compute the displacement feedback for homogeneous reaction zones, which do not fulfill the requirement of a very thin flame imposed by the model of Schwing et al. [109].

3 Computational Tools and Modelling Techniques for Thermoacoustic Problem Analysis

The present chapter introduces the numerical techniques used throughout this work. A variety of approaches was employed in order to deal with the different feedback mechanisms, and to distinguish their respective contributions. Hence, the impact of pressure waves on chemical kinetics is investigated first at a fundamental level using simplified setups, i.e. in 0D homogeneous reactor, 1D plug flow reactor, and 1D premixed flame setups. More complex configurations with realistic geometries and turbulence are calculated using compressible Large Eddy Simulations (LES), which rely on tabulated chemistry data obtained from homogeneous reactor calculations. Advanced post-processing methods have been developed in order to extract information on the distinct contributions from the extensive set of data available in LES. Finally, acoustic network models are employed in this work in order to illustrate their impact on system stability. All these tools are presented as an overview in this chapter. Moreover, multi-dimensional acoustic solver tools based on finite-element-methods are introduced, since these are very relevant in industrial practice.

Before starting with the presentation of the tools, it shall be mentioned that all of them are based on the Navier-Stokes equations, which describe the conservation of continuity, momentum, energy, and species for Newtonian fluids. The Einstein notation will be used throughout this chapter for a compact notation of the transport equations. The set of partial differential equations can be written as follows [91], when omitting volumetric forces, radiative heat exchange and external heat sources:

- Continuity:

$$\frac{\partial \rho}{\partial t} + \frac{\partial (\rho u_i)}{\partial x_i} = 0. \tag{3.1}$$

- Momentum:
$$\rho\frac{\partial u_i}{\partial t}+\rho u_j\frac{\partial u_i}{\partial x_j}=-\frac{\partial p}{\partial x_i}+\frac{\partial t_{ij}}{\partial x_j}, \tag{3.2}$$
with t_{ij} denoting the elements of the shear stress tensor.

- Species:
$$\rho\frac{\partial Y_k}{\partial t}+\rho u_j\frac{\partial Y_k}{\partial x_j}=\frac{\partial}{\partial x_j}\left(\rho\frac{\nu}{\mathrm{Sc}_k}\frac{\partial Y_k}{\partial x_j}\right)+\rho\dot{\omega}_k, \tag{3.3}$$
with ν, Sc_k, and $\dot{\omega}_k$ denoting the dynamic viscosity of the fluid, the dimensionless Schmid number of the species k, and the mass-specific net formation rate of the species k, respectively.

- Energy (expressed here in terms of sensible enthalpy h_s):
$$\begin{aligned}\rho\frac{\partial h_s}{\partial t}+\rho u_j\frac{\partial h_s}{\partial x_j}=\frac{\partial p}{\partial t}+u_j\frac{\partial p}{\partial x_j}+t_{ij}\frac{\partial u_i}{\partial x_j}+\frac{\partial}{\partial x_j}\left(\rho\frac{\nu}{\mathrm{Pr}}\frac{\partial h_s}{\partial x_j}\right)\\ +\dot{q}-\frac{\partial}{\partial x_j}\left(\sum_k\rho h_{s,k}Y_k\frac{\nu}{\mathrm{Sc}_k}\frac{\partial Y_k}{\partial x_j}\right)\end{aligned} \tag{3.4}$$
with Pr and $\dot{q}$ denoting the dimensionless Prandtl number and the volumetric heat source term linked to chemical reactions, respectively.

The system of equations is closed by additionally considering an equation of state. The ideal gas law is generally used when dealing with gas turbine combustion:
$$\frac{p}{\rho}=RT. \tag{3.5}$$

The common modelling tools use variants of the Navier-Stokes equations with differing simplifications and in various formulations, as will be explicated in the following.

3.1 Reactor and one-dimensional flame calculations

3.1.1 Homogeneous reactor calculations using detailed chemistry

Homogeneous reactor calculations simplify the partial differential equation (PDE) system to an ordinary differential equation (ODE) system, as no spatial dimension is taken into account. It is representative of a perfectly stirred

reactor evolving in time. The ODE system is integrated in time to yield the temporal evolution of mass fractions $Y_i(t)$ for every considered species i, taking into account all k reactions retained in the mechanism:

$$\frac{dY_i}{dt} = \sum_k \dot{\omega}_{k,i}(T, p, Y_i) \tag{3.6}$$

The species source terms are expressed using an Arrhenius expression as indicated by Eq. (2.2). Since the reactors are taken as adiabatic, the total enthalpy of the system stays constant. Furthermore, the pressure is kept constant during each iterative solution step. The temperature change due to chemical reactions is determined by a Newton iteration based on the variation of the chemical formation enthalpy of the mixture.

The calculations of homogeneous reactors were performed in the present work using the software package Cantera [31], which can be called via interfaces with Matlab, Python and C++. It asks for the input of an appropriate chemical mechanism, which provides the necessary data for the computation of reaction rates. As the main focus laid on auto-ignition calculations at elevated pressures, the Galway C3-41 mechanism [88] was used throughout this work, as it had been validated for this kind of physical problems.

Cantera uses an iterative time advancement procedure to compute the reactor evolution. However, it does not use the set of equations specific to constant-pressure reactors, but rather a network composed of the reactor itself and a surrounding reservoir, for which the pressure is set, and a separating wall. As input, one needs to specify a wall expansion parameter, which specifies the rate of change of the reactor volume as a function of the pressure difference between reactor and reservoir. In order to keep the pressure in the reactor constant, high values are to be chosen for this parameter.

Using such a setup, the evolution of constant-pressure reactors can be calculated in straightforward manner with Cantera, allowing to derive heat release and species source term evolutions over time. A reaction progress Y_c is introduced in order to simplify the description, which is defined as

$$Y_c = Y_{\mathrm{CH_2O}} + Y_{\mathrm{CO}} + Y_{\mathrm{CO_2}} - \left(Y_{\mathrm{CH_2O}} + Y_{\mathrm{CO}} + Y_{\mathrm{CO_2}}\right)_{t=0}. \tag{3.7}$$

The reaction progress can also be written in normalised form:

$$c = \frac{Y_{CH_2O} + Y_{CO} + Y_{CO_2} - \left(Y_{CH_2O} + Y_{CO} + Y_{CO_2}\right)_{t=0}}{\left(Y_{CH_2O} + Y_{CO} + Y_{CO_2}\right)_{max} - \left(Y_{CH_2O} + Y_{CO} + Y_{CO_2}\right)_{t=0}}. \tag{3.8}$$

This composite progress variable allows a proper description of both induction and heat release period, as it contains intermediate (CH_2O, CO) as well as product species (CO_2). At equilibrium the normalised progress variable reaches unity. Typical time evolutions of the normalised progress variable and its source term are shown in Fig. 3.1.

For thermoacoustic analysis, the source term evolution under time-varying pressure and temperature conditions is of main interest. Unfortunately, Cantera does not allow to vary these conditions externally during the advancement of the reactor. Instead, for such dynamic simulations, the thermodynamic state is modified in between the advancement steps, by isentropic state changes. As a result, a piecewise constant pressure evolution is obtained with this method. Such an approximation can be regarded as valid as long as the time advancement step size is small with respect to the period of the acoustic oscillation.

Reactor simulation setups with constant and varying pressure are used in this study to investigate dynamic effects in auto-igniting reactors, quantify relevant sensitivities, and validate model predictions for the ignition delay in perturbed reactors. The detailed procedure and the results obtained will be shown in chapter 4.

3.1.2 Premixed flame calculations with detailed chemistry

Since flame propagation also plays a role in sequential combustors, the sensitivity of reaction rates in premixed flame configurations is also investigated in this work. For that purpose, the chemistry solver is used again with the Galway C3-41 reaction mechanism. The Navier-Stokes equations are solved iteratively in a single spatial dimension, without considering volumetric forces, radiation effects, or external heat sources.

As will be explained in section 4.4.6, such one-dimensional flame calculations are used to compare the sensitivities of chemical reaction rates in ho-

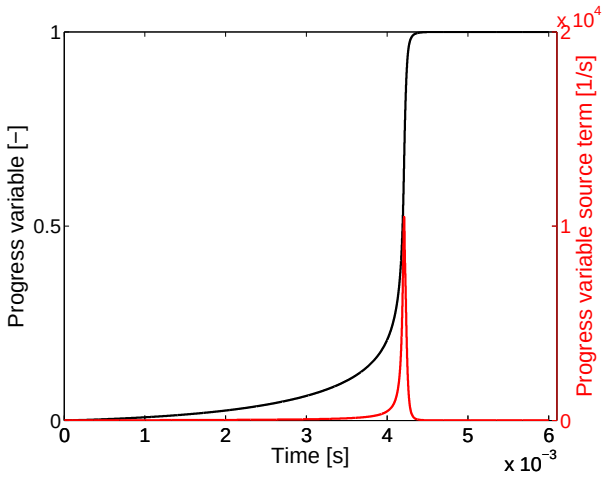

Figure 3.1: Temporal evolutions of c and $\dot{\omega}_c = \frac{dc}{dt}$ in a homogeneous reactor (air-excess ratio λ=3)

mogeneous reactors and premixed flames. All simulations were conducted at steady pressure levels.

3.1.3 Plug flow reactor modelling

A *plug flow* reactor is defined as a sequence of *plugs* which are injected at different instants into a straight tube and evolve independently of each other. Each plug is hereby moving at a convective speed $\overline{u}_c$, as illustrated in Fig. 3.2. A perfectly premixed auto-ignition flame can be approximated by such a setup; this will be explained in detail in section 4.1.1. Such a highly idealised model configuration is very convenient for the fundamental description of the flame dynamics linked to the sensitivity of chemical kinetics to acoustic perturbations, as indicated in the sketch by the acoustic waves f and g.

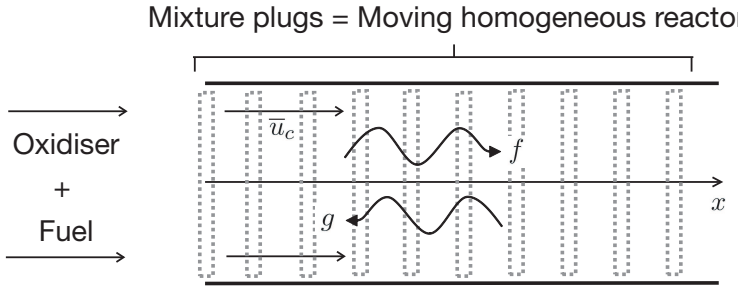

Figure 3.2: Sketch of plug flow reactor model

The temporal evolution of this setup is calculated by the joint simulation of convectively transported homogeneous reactors (representing the plugs) and acoustic wave propagation. Standard chemical reaction solvers like Cantera do, however, not allow such calculations. Instead, this scenario is modelled in Matlab [71] by calculating the temporal evolution of a multitude of homogeneous reactors, injected at different instants and subjected to acoustic excitation. In order to reduce the computational effort, tabulated chemistry is employed. Interpolation data were provided for the chemical source term at reference pressure as a function of progress variable. Pressure sensitivity can be taken into account either via an interpolation for a varying sensitivity factor $\varphi_p(c)$ or via a constant factor φ_p. The actual definition of this factor will be given in section 4.2.2.

Running the simulation over time, an instantaneous reaction rate can be calculated for each convected homogeneous reactor, and the total heat release rate results as the sum over all plugs. The results are used for the verification of the analytical model developed.

3.2 Large eddy simulation (LES) of sequential combustors

An important part of the present work relies on LES of turbulent sequential combustor flows. Two different configurations are investigated, a perfect premix and a technical premix combustor. LES has been increasingly used in the engineering and scientific community in recent years, as it allows better predictions of flow fields than standard RANS calculations. This is specially true when complex flows are concerned, e.g. with swirl and/or recirculation zones. The flow configurations to be studied in this work contain such flow patterns; the use of more expensive LES was therefore without alternative. Moreover, one of the investigated feedback mechanisms is coherent vortex formation, which definitely cannot be described properly with a RANS approach.

3.2.1 Conservation equations in LES

Turbulent flows can be calculated by applying the conservation equations in their original form. This is done in Direct Numerical Simulation (DNS)

and is prohibitively expensive for technical applications, as all relevant scales down to the Kolmogorov level have to be resolved. Whereas RANS simulations model all turbulent scales, LES proceeds to a separation between resolved and subgrid scales. The separation depends on the selected mesh element size and hence corresponds to a spatial filtering of the turbulent fluctuations.

A spatial, mass-weighted filtering is introduced (using vector notation) [91]:

$$\langle \rho f \rangle = \langle \rho \rangle \widetilde{f}(\vec{x}) = \int \rho f(\vec{x}') F(\vec{x} - \vec{x}') d\vec{x}' \tag{3.9}$$

with $\langle \cdot \rangle$ and $\widetilde{\cdot}$ denoting Reynolds and Favre filtered values, respectively. Instantaneous values of a variable can thus be decomposed into a sum $f = \widetilde{f} + f^\star$, where $f^\star$ is the subgrid scale fluctuation term. Applied on the conservation equations this yields the following filtered transport equations (again omitting volumetric forces, radiation and external heat sources):

- Continuity:

$$\frac{\partial \langle \rho \rangle}{\partial t} + \frac{\partial}{\partial x_i} \left(\langle \rho \rangle \widetilde{u}_i \right) = 0. \tag{3.10}$$

- Momentum:

$$\langle \rho \rangle \frac{\partial \widetilde{u}_i}{\partial t} + \langle \rho \rangle \widetilde{u}_i \frac{\partial \widetilde{u}_j}{\partial x_j} = -\frac{\partial \langle p \rangle}{\partial x_i} + \frac{\partial \langle t_{ij} \rangle}{\partial x_j} - \frac{\partial}{\partial x_j} \left(\langle \rho \rangle \widetilde{u_j^\star u_i^\star} \right), \tag{3.11}$$

- Species:

$$\langle \rho \rangle \frac{\partial \widetilde{Y}_k}{\partial t} + \langle \rho \rangle \widetilde{u}_j \frac{\partial \widetilde{Y}_k}{\partial x_j} = \frac{\partial}{\partial x_i} \left(\langle \rho \rangle \widetilde{\frac{\nu}{\mathrm{Sc}_k} \frac{\partial Y_k}{\partial x_i}} \right) + \langle \rho \rangle \widetilde{\dot{\omega}}_k - \frac{\partial}{\partial x_j} \left(\langle \rho \rangle \widetilde{u_j^\star Y_k^\star} \right), \tag{3.12}$$

- Energy:

$$\begin{aligned} \langle \rho \rangle \frac{\partial \widetilde{h}_s}{\partial t} + \langle \rho \rangle \widetilde{u}_j \frac{\partial \widetilde{h}_s}{\partial x_j} = \frac{\partial \langle p \rangle}{\partial t} + \left\langle u_j \frac{\partial p}{\partial x_j} \right\rangle + \left\langle t_{ij} \frac{\partial u_i}{\partial x_j} \right\rangle + \frac{\partial}{\partial x_j} \left(\langle \rho \rangle \widetilde{\frac{\nu}{\mathrm{Pr}} \frac{\partial h_s}{\partial x_j}} \right) \\ + \langle q \rangle - \frac{\partial}{\partial x_j} \left(\sum_k \left\langle \rho h_{s,k} Y_k \frac{\nu}{\mathrm{Sc}_k} \frac{\partial Y_k}{\partial x_j} \right\rangle \right) \\ - \frac{\partial}{\partial x_j} \left(\langle \rho \rangle \widetilde{u_j^\star h_s^\star} \right), \end{aligned} \tag{3.13}$$

The numerical solution of this set of partial differential equations requires the following modelling steps:

1. to perform additional approximations regarding the laminar diffusive fluxes and the pressure correction term,

2. to model the subgrid fluctuation terms,

3. to determine the filtered reaction source term values.

The additional approximations (point 1) are generally formulated as follows [91]:

$$\langle t_{ij} \rangle \approx -\langle \rho \rangle \frac{2}{3} \langle \nu \rangle \frac{\partial \widetilde{u}_k}{\partial x_k} \delta_{ij} + \langle \rho \rangle \langle \nu \rangle \left(\frac{\partial \widetilde{u}_i}{\partial x_j} + \frac{\partial \widetilde{u}_j}{\partial x_i} \right) \tag{3.14}$$

$$\widetilde{\frac{\nu}{\mathrm{Sc}_k} \frac{\partial Y_k}{\partial x_i}} \approx \frac{\langle \nu \rangle}{\mathrm{Sc}_k} \frac{\partial \widetilde{Y}_k}{\partial x_i} \tag{3.15}$$

$$\widetilde{\frac{\nu}{\mathrm{Pr}} \frac{\partial h_s}{\partial x_i}} \approx \frac{\langle \nu \rangle}{\mathrm{Pr}} \frac{\partial \widetilde{h}_s}{\partial x_i} \tag{3.16}$$

$$\sum_k \left\langle \rho h_{s,k} Y_k \frac{\nu}{\mathrm{Sc}_k} \frac{\partial Y_k}{\partial x_j} \right\rangle \approx \langle \rho \rangle \sum_k \widetilde{h}_{s,k} \widetilde{Y}_k \frac{\langle \nu \rangle}{\mathrm{Sc}_k} \frac{\partial \widetilde{Y}_k}{\partial x_j} \tag{3.17}$$

$$\left\langle u_j \frac{\partial p}{\partial x_j} \right\rangle \approx \widetilde{u}_j \frac{\partial \langle p \rangle}{\partial x_j} \tag{3.18}$$

The subgrid fluctuation terms (point 2) can be modelled in different ways, as explained in [91]. For the present work, a dynamic Smagorinsky-Lilly approach was chosen, introducing a subgrid scale turbulent viscosity ν_{SGS}, which is determined as a function of the local flow conditions. For details regarding the computation of ν_{SGS}, please refer to the book of Poinsot and Veynante [91] or the Fluent user manual [1]. Using a Boussinesq approximation, the corresponding subgrid terms can be modelled as follows:

- Momentum:

$$\widetilde{u_j^\star u_i^\star} - \frac{\delta_{ij}}{3} \widetilde{u_k^\star u_k^\star} = -\nu_{SGS} \left(\frac{\partial \widetilde{u}_i}{\partial x_j} + \frac{\partial \widetilde{u}_j}{\partial x_i} \right) + \frac{1}{3} \langle \nu \rangle \frac{\partial \widetilde{u}_k}{\partial x_k} \delta_{ij} \tag{3.19}$$

- Species:

$$\widetilde{u_j^\star Y_k^\star} = \frac{\nu_{SGS}}{\mathrm{Sc}_{k,t}} \frac{\partial \widetilde{Y}_k}{\partial x_i} \tag{3.20}$$

- Energy:

$$\widetilde{u_j^\star h_s^\star} = \frac{\nu_{SGS}}{\mathrm{Pr}_t}\frac{\partial \widetilde{h}_s}{\partial x_i} \tag{3.21}$$

At this point, only the reactive source terms in species and energy transport equations are still missing to close the system of equations (point 3). They are provided by a combustion model, which has to describe the reaction chemistry, including the impact of temperature and composition fluctuations at the subgrid scale. The latter aspect is generally referred to as the modelling of *turbulence-chemistry interaction*, and represents a field of intense research work. Extensive reviews of turbulence-chemistry interaction models can be found in the literature for RANS and LES; e.g. in the books of Poinsot and Veynante [91], Echekki and Mastorakos [25], or in the works of Hoffmann [41] and Kulkarni [57]. The next subsection presents the modelling approach used in the present work, which is specifically designed for the calculation of gas turbine reheat combustors, but might as well as be used for all types of processes with MILD or flameless combustion, as explained by Kulkarni [57].

3.2.2 Combustion modelling for reheat combustors

The use of an appropriate combustion model is essential for the present work, since it aims at elucidating the dynamic behaviour of distinct flame stabilisation mechanisms, which therefore need to be properly captured by the simulation.

Therefore, an important objective was to develop an LES combustion model suitable for both auto-ignition and flame propagation, building on earlier work in the RANS context [10]. The model shall be computationally efficient, since it should be also suitable for the calculation of industrial burners. A description of the model for LES of auto-ignition in turbulent hydrogen flames can be found in [59] including a validation with experiments. Here it is used for methane; a validation of the method for this fuel is reported in [58].

For the chemistry representation, the model uses a progress variable / mixture fraction / lookup-table approach based on detailed chemistry calculations [8, 89], which requires an adaptation to the fuel/oxidiser pair considered. The progress variable and the mixture fraction are defined as previously.

The tables are generated offline using spatially homogeneous 0D reactor simulations at various mixture fractions and are stored as a function of mixture fraction and progress variable. The detailed chemistry solver Cantera and the reaction mechanism Galway C3-41 [88] are also employed for the chemistry table generation.

The turbulence-chemistry interaction is modelled by a Eulerian fields approach [116], which uses a system of stochastic differential equations. Each stochastic field represents a statistical (but not physical) realisation of a field distribution. This method of turbulence-chemistry modelling was successfully applied for autoignition simulations in LES with detailed chemistry [50, 51, 78]. In these works, a number of eight fields was judged to be sufficient when applying LES; a study (unpublished) conducted at the authors' institute involving up to 40 stochastic fields supports this conclusion. Some perfect premix simulations presented in chapter 5 have also been conducted with 16 fields, yielding no noticeable differences in the results. As a consequence, eight fields were used for all perfect premix simulations presented in this work. However, for the calculation of the technical premix case, only one field was considered, the turbulence-chemistry interaction at the subgrid scale is thus neglected. This was due in order to limit the computational effort and will be discussed in more detail in chapter 6.

The Ito formulation was employed for the stochastic calculus in this work. The detailed derivation and description of the method is subject of the work of Valino [116]. Equations (3.23)-(3.26) are formulated as done in [116] for an arbitrary scalar.

Stochastic partial differential equations (PDE) are solved for progress variable and for the required number of mixture fractions (one for binary mixing and two for ternary mixing):

$$\frac{\partial Z^{(n)}}{\partial t} + u_j \frac{\partial Z^{(n)}}{\partial x_j} = \frac{1}{\langle\rho\rangle}\frac{\partial}{\partial x_j}\left(\Gamma \frac{\partial Z^{(n)}}{\partial x_j}\right) + \dot{\omega}^{(n)}_{Z,stoch} - \dot{\omega}^{(n)}_{Z,mix} \tag{3.22}$$

$$\frac{\partial Y_c^{(n)}}{\partial t} + u_j \frac{\partial Y_c^{(n)}}{\partial x_j} = \frac{1}{\langle\rho\rangle}\frac{\partial}{\partial x_j}\left(\Gamma \frac{\partial Y_c^{(n)}}{\partial x_j}\right) + \dot{\omega}^{(n)}_{Y_c,chem} + \dot{\omega}^{(n)}_{Y_c,stoch} - \dot{\omega}^{(n)}_{Y_c,mix} \tag{3.23}$$

The effective diffusivity is given by $\Gamma = \langle\rho\rangle(\nu + \nu_t)/\mathrm{Sc}$. The chemical source term $\dot{\omega}^{(n)}_{Y_c,chem}$ is read from the chemistry tables as a function of $c^{(n)}$. The two

additional source terms $\dot{\omega}^{(n)}_{Z(Y_c),stoch}$ and $\dot{\omega}^{(n)}_{Z(Y_c),mix}$ describe the effects of dispersion and micro-mixing on the subgrid scale. The dispersion term leads to a scattering into all three spatial dimensions; it depends on the scalar gradient and is modelled as (given here for the mixture fraction):

$$\dot{\omega}^{(n)}_{Z,j,stoch} = \underbrace{\sqrt{dt}\,\eta^{(n)}_j}_{\text{Wiener process}} \sqrt{2\frac{\Gamma}{\langle\rho\rangle}\frac{\partial Z^{(n)}}{\partial x_j}\frac{1}{dt}}. \tag{3.24}$$

The term $\eta^{(n)}_j$ is a random number switching between -1 and 1 [116]. In order to ensure isotropy of the dispersion process, the sum of all $\eta^{(n)}_j$ should equal zero. The mutual interaction of the different fields is represented by a micro-mixing term $\dot{\omega}^{(n)}_{c,mix}$ according to the "Interaction by exchange with the mean" (IEM) model [117]:

$$\dot{\omega}^{(n)}_{Z,mix} = \frac{C_{mix}(\nu+\nu_t)}{\Delta^2}\left(Z^{(n)} - \widetilde{Z}\right), \tag{3.25}$$

with the filtered mixture fraction given by

$$\widetilde{Z} = \frac{\sum_{n=1}^{N} Z^{(n)}}{N}. \tag{3.26}$$

For the present work, a constant value of $C_{mix} = 2$ was chosen for the mixing constant. This allows closure of the stochastic PDEs for the progress variable in each field.

However, these need to be linked to the remaining non-stochastic PDEs of the flow, i.e. enthalpy, to describe the heat release. One possibility would be to include temperature data in chemistry tables, and to calculate a resulting filtered temperature as an average over all stochastic fields. However, this would only be appropriate for incompressible flows. Instead, transport equations are solved for main species, which are determining the standard formation enthalpy of the mixture, as suggested by Galpin et al. [29]. In the present work, the following species were selected: CH_4, O_2, CO_2, CO, H_2O, and N_2. As commonly done, no transport equation is solved for nitrogen, its mass fraction being defined as $Y_{N_2} = 1 - \Sigma Y_i$. Hence, values for mass fractions of the transported species $Y_{k,tab}$ are included in the chemistry tables, and the cor-

responding species mass fractions $\widetilde{Y_k}$ are driven via relaxation (see [15, 75]) toward their target values, which result from an averaging over all fields:

$$\langle \dot{\omega} \rangle = \frac{\frac{1}{N}\sum_{n=1}^{N} Y_{k,tab}^{(n)} \left(Y_c^{(n)} + \dot{\omega}_{Y_c,chem}^{(n)} dt \right) - \widetilde{Y_k}}{dt}. \tag{3.27}$$

Equation (3.27) defines a filtered species source term, which closes the species transport equations and which is formulated such that the filtered species mass fractions closely follow the tabulated values computed from the reaction progress fields. Great care has to be exercised on the correct formulation of Eq. (3.27), in particular when periodic excitation is applied. It is hence very important to formulate the source term in forward direction with $\widetilde{Y_k}$ at time t and the estimated $Y_{k,tab}$ at time $t + dt$, in order to avoid any inconsistencies.

Eventually, the volumetric heat release rate can be derived from the resulting change in formation enthalpy:

$$\langle \dot{q} \rangle = -\langle \rho \rangle \sum_k \widetilde{\dot{\omega}}_k \, h_k^\circ. \tag{3.28}$$

In that manner, a fully compressible formulation is obtained, which avoids divergence between CFD and tabulated data through the relaxation of main species. It shall be mentioned that the tabulation was done for reference pressure conditions. Hence, the combustion model as presented here does not capture the effect of acoustic perturbations on the chemistry. This effect can be added in an efficient, approximate manner with a pressure sensitivity factor as will be shown in section 4.4.6.

3.2.3 Flame configurations studied with LES

3.2.3.1 Perfect premix case setup

The LES allows to investigate setups which are more alike real configurations than those used for the analytical description of the chemical dynamics. Nevertheless, it was also chosen to proceed to a stepwise increase of the complexity for the LES study. Hence, a generic perfect premix combustor was defined first, for investigating the flame dynamics in the absence of mixing inhomogeneities. It was furthermore very helpful during the development of the com-

bustion model, because physical inconsistencies and programming errors can be easily detected in homogeneous mixing cases.

The corresponding geometry is shown in Fig. 3.3 and consists of two coaxial cylindrical tubes of non-equal diameter, connected by a sudden area jump. The diameter at the inlet is 80 mm, a value of 2.5 was chosen for the area expansion ratio. The geometry has a total length of 250 mm. The main simplification compared to a real combustor is the perfect premixture of cold fuel and hot oxidiser at the inlet. For such mixture configurations, the shortest ignition delay times are obtained for very lean conditions. For this reason a mixture fraction of $Z = 0.01$ was selected, in order to have a realistic representation of the interaction between auto-ignition in lean regions and flame propagation in the shear layers. The oxidiser composition corresponds to lean methane-air combustion in a first stage and was computed using detailed chemistry calculations with Cantera and the detailed Galway C3-41 mechanism [88]. For the arbitrary operating conditions used in the present study, only main species O_2, CO_2, H_2O, and N_2 were retained at the inlet. The oxidiser temperature is 1300 K, the temperature of the fuel consisting of pure methane is 300 K. For the premixed inlet, the boundary conditions can be obtained from the mixture fraction, yielding a mixture composition as given in Table 3.1. Different inlet velocities were imposed, ranging from 40 to 55 m/s; the reference pressure was set to 18 bar.

Compressible LES was performed with the commercial software Fluent 13, using the coupled pressure-based solver. Temporal discretisation was set to second-order, spatial discretisation was performed with a second-order upwind scheme. A timestep of 3 μs was used throughout all simulations. Subgrid scale viscosity was modelled with a dynamic Smagorinsky approach.

The computational mesh consists of 1.16 million hexahedral elements, and includes refined layers close to the adiabatic duct walls and along the shear layer axis. In the shear layer region, the subgrid filter length lies within a range of 1.3 up to 3.4 times the laminar flame thickness obtained from 1D detailed chemistry calculations. The resulting LES quality index as defined by Celik et al. [13] ranges between 0.5 and 0.9 in the flame region. Lower values going down to 0.3 are only observed at the downstream part of the corner recirculation zone, and should not have a significant impact on the flame dynamics. The mesh independence of the presented results could be stated by running

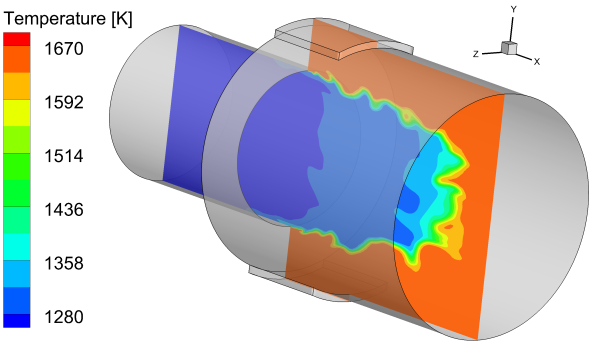

Figure 3.3: 3D view of investigated geometry with temperature distribution in symmetry plane

Y_{CH_4}	Y_{O_2}	Y_{CO_2}	Y_{H_2O}	T
0.01	0.145	0.0555	0.0455	1270.7 K

Table 3.1: Summary of inlet boundary conditions for perfect premix case

additional simulations on finer meshes with 2.22 and 4.74 million cells. These two yielded the same qualitative flame behaviour and comparable quantitative distributions of mean and fluctuation values as those shown in the remaining of this work.

3.2.3.2 Technical premix case

The technical premix case is inspired by a test rig installed at the Lehrstuhl für Thermodynamik of the TU München, which is used for the experimental investigation of transverse mode instabilities in reheat combustors. However, the geometry used in the present work corresponds to a previous test rig configuration, which slightly differs from the actual one. The computational geometry is shown in Fig. 3.4; in comparison to the original geometry, the area change is located more upstream and shows a larger expansion ratio. The calculations were again run with Fluent 13, with the same discretisation and time-step settings as for the perfect premix case.

The reference pressure level in the calculation is set to 4.3 bar, since the combustor is installed inside a high pressure cell on the test rig. A lean mixture of burnt products is imposed at the inlet, at a temperature of 1253 K. An inlet tur-

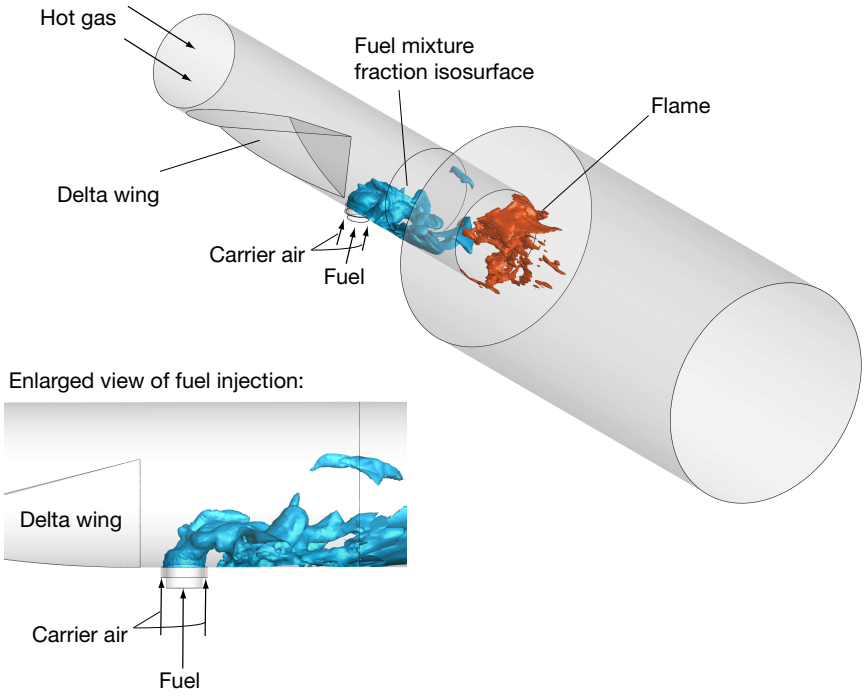

Figure 3.4: 3D view of technical premix test case, with enlargement of fuel injection

Hot gas inlet	$\overline{u}_{in}$	18.5 m/s
	T	1253 K
	Y_{CH_4}	0
	Y_{O_2}	0.143
	Y_{CO_2}	0.0578
	Y_{H_2O}	0.0473
	Y_{CO}	$3.8 \cdot 10^{-7}$
Fuel inlet	$\dot{m}_F$	0.0017 kg/s
	T	300 K
	Y_{CH_4}	1
Carrier air inlet	$\dot{m}_{CA}$	0.0052 kg/s
	T	300 K
	Y_{O_2}	0.232

Table 3.2: Summary of inlet boundary conditions for technical premix case

bulence of 5 % is imposed, which however plays a secondary role, since most turbulence is produced by the delta wing that acts as a vortex generator and is located upstream of the fuel injector. Similar to Alstom's SEV configuration,

the wing generates a counter-rotating vortex pair, where the fuel stream is injected into. The fuel addition is made by a concentric jet-in-crossflow, with shielding air surrounding the methane injection. All inlet boundary conditions are summarised in Table 3.2.

The computational mesh consists of tetrahedral, hexahedral, and pyramid elements. The block-structured hex domain is used for the downstream part of the geometry, i.e. the downstream end of the burner and the combustion chamber. The hexahedral mesh topology is very similar to the one used for the perfect premix case, with grid refinements close to the walls and, in particular, in the shear layer after the area expansion. The tetrahedral mesh is used for the upstream volume around the delta wing and the injection, being more suitable for such complex geometries and allowing a refinement region closely following the streamlines of the fuel injection. The interface between tetrahedral and hexahedral regions contains pyramid elements, which shape the transition between the different element types. Special care must be addressed to this aspect, as highly skewed tetrahedral elements can appear in the interface region and might give rise to the appearance of flow discontinuities over the interface. This has to be avoided, and should be checked during each calculation.

The resulting mesh consists of 2.22 million cells in total and ensures a continuous transition over the hybrid mesh interface. A thorough mesh independence study could not be executed for the present study due to the high computational cost of the simulations. However, the technical premix test case can be regarded as less critical than the perfect premix one, due to the far lower velocities applied at the inlet. Indeed, when looking at the turbulent viscosity ratio distributions, one can recognise much lower values for the technical premix setup, with values below 20 (this corresponds approximately to a quality index of over 0.8) in nearly the entire domain. Maximum values beyond this limit mostly appear behind the area expansion in the recirculation zone, and can thus be considered of negligible impact on the flame.

3.2.4 Acoustic boundary conditions and excitation

In order to ensure a stable stationary solution, non-reflecting boundary conditions (NRBC) were applied to inlet and outlet, using the state-space approach

developed by Schuermans et al. [105]. Anechoic ends are characterised by a zero acoustic impedance and hence by the relation $p' = \overline{\rho}\overline{a}u'$, with $\overline{a}$ denoting the average speed of sound in the mixture. This relation can be easily applied to velocity-inlet and pressure-outlet boundary conditions. However, to obtain a steady state of the mean flow, the boundary condition signal needs to be high-pass filtered. The cut-off frequency is generally chosen to lie below all relevant acoustic frequencies. Low-frequency fluctuations related to the mean flow are thus fully reflected, in contrary to the acoustic fluctuations. A first-order high-pass filter is implemented through a discrete state-space system, which intrinsically "filters" out turbulent fluctuations. The calculated inlet velocity can finally be superposed with turbulent fluctuation terms, as obtained from the standard inlet turbulence generator in Fluent.

The use of NRBCs at the inlet and outlet avoids the generation of low-frequency, longitudinal instabilities, which are not of interest for the present work. Such boundary conditions do however not affect purely transverse modes. When running such a compressible LES, the time evolutions of pressure and velocity should be monitored, in order to assess whether transverse instabilities are self-excited or not. If that is the case, no additional excitation is needed, and the flame can be analysed, as long as a stable, limit-cycle fluctuation regime establishes. This was the case for the technical premix flame, where an initial perturbation linked to the ignition of the mixture led to a stationary, fluctuating state, where in particular the first transverse mode was excited. The corresponding Fourier transform of a pressure probe located in the shear layer is shown in Fig. 3.5 , together with a snapshot of the pressure contour filtered around the peak frequency of 3000 Hz. One can clearly recognise the presence of the first transverse mode in this setup. The original perturbation was in this case due to the rather strong mixture stratification in the setup, which will be discussed in more detail in chapter 6. For the simulated conditions, the jet penetration depth is low, and hence much more fuel is concentrated on the lower side of the combustor.

For the perfect premix case, after initial ignition, no noticeable fluctuations could be observed at frequencies representative of the first transverse mode, which was evaluated to be around 3838 Hz using FEM simulations with mean temperature distributions obtained from LES. Some decaying fluctuation amplitudes could, however, be observed in the Fourier transform of pressure time series at higher frequencies close to 7450 Hz.

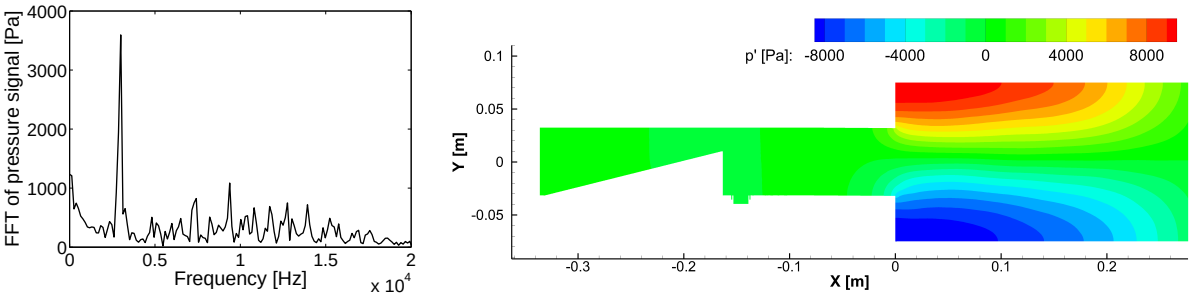

Figure 3.5: Left: FFT of pressure signal in technical premix combustor. Right: Instantaneous pressure disturbance field filtered at peak frequency

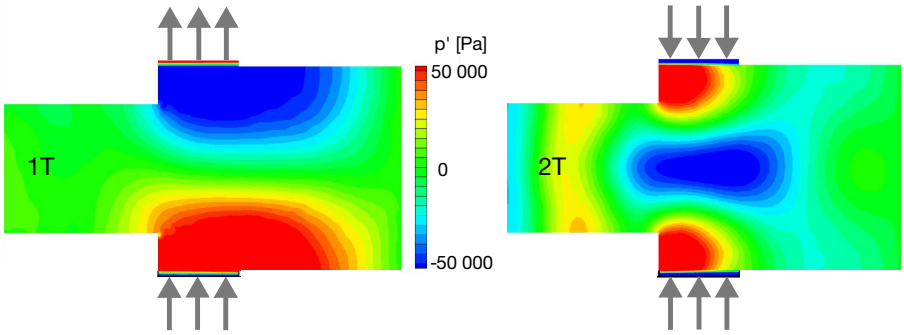

Figure 3.6: Orientation of momentum source terms used for the excitation of transverse modes; instantaneous snapshots of resulting pressure contours

In order to investigate the flame response to transverse modes, it was thus necessary to provide additional means of acoustic excitation. Therefore, momentum source terms were applied in transverse direction in the porous zones located on top and bottom of the combustor (see Fig. 3.3). To force a specific mode type, one has to choose a suitable excitation frequency and source term direction. The excitation direction simply depends on the mode type: the first transverse mode (1T) asks for an asymmetric excitation at top and bottom (same direction), whereas the second transverse mode (2T) is excited symmetrically, as illustrated in Fig. 3.6. A 1T mode was excited at a frequency of 3838 Hz, while a 2T mode appeared when exciting at 7450 Hz. Snapshots of the resulting pressure fields are shown in Fig. 3.6. One can observe that the 2T mode is not purely transverse, as axial variations also appear.

The momentum sources were applied in porous zones outside the combustor domain. High porous loss coefficients were applied, such that the interface between the fluid and porous domains behaves similarly to a wall with re-

spect to the mean flow. Indeed, without excitation, the presence of the porous zones does not have a noticeable impact on the mean flow. Contrary to a wall boundary condition, the porous zones allow an efficient excitation of acoustic waves in the fluid domain, as it acts like a variable pressure boundary condition. As was shown by Guillozet [36] in a diploma thesis supervised by the author of the present work, periodic momentum source terms lead to periodic, phase-shifted pressure fluctuations. The mode shapes shown in Fig. 3.6 point out an additional phase shift between the pressure signals in the porous and in the fluid domain. The existence of phase shifts do not have any consequences on the subsequent analysis, as only acoustic fluctuations in the fluid domain are of interest. Guillozet [36] also showed that the excitation could be applied directly in the fluid domain, without significantly altering the results. Thereby, the excitation regions should be defined close to the pressure maximum, in order to get the most efficient excitation.

3.3 Acoustic solver tools for stability prediction

The computational methods described above mainly aim at characterising the response of the flame to a certain acoustic perturbation. The stability of the acoustics are not of main interest, even though LES also allows conclusions regarding this aspect. In the literature, the LES-based investigation of acoustic mode stability is widely referred to as a "brute-force approach", as it is extremely costly in terms of computational demand. Hence, such an approach cannot be used during an industrial design process, where different design variants shall be evaluated regarding stability in limited time.

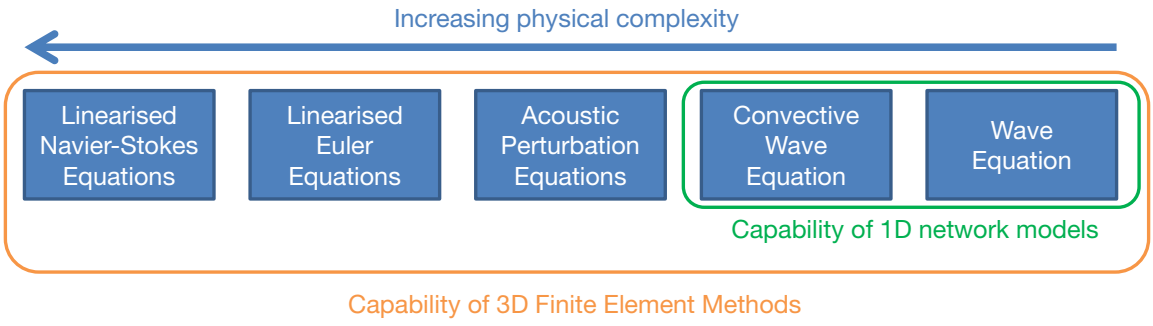

Figure 3.7: Graphical overview of computational methods used for the prediction of acoustic mode stability (adapted from Huber [44])

To this end, various acoustic solvers are commonly used in gas turbine industry; a graphical representation of the different solver types is shown in Fig. 3.7. The different solvers can be categorised on the basis of two characteristics: the geometrical dimensionality (1D/3D) and the types of equations solved (see Fig. 3.7). Only the solver types relevant to the present work shall be explained here, further information can be found in the works of Huber [44] and Pieringer [90].

The simplest mathematical description of acoustic disturbances can be made using the Helmholtz equation. It can be derived from the Navier-Stokes equations by expanding every flow parameter into a mean and a fluctuating value (see chapter 2). Furthermore, convective and viscous effects as well as entropy waves are neglected, and fluid properties are assumed to be constant. With these simplifications, the following wave equation holds true:

$$\frac{\partial^2 p'}{\partial t^2} - \overline{a}^2 \frac{\partial^2 p'}{\partial x_i \partial x_i} = 0 \tag{3.29}$$

with

$$\overline{\rho} \frac{\partial u_i'}{\partial t} = -\frac{\partial p'}{\partial x_i} \tag{3.30}$$

and $\overline{a}$ denoting the average speed of sound in the mixture. The wave equation can be extended in order to account for low Mach mean flow and thus for convective effects. The resulting equation is known as the convective wave equation and reads as follows:

$$\left(\frac{\partial}{\partial t} + \overline{u_i} \frac{\partial}{\partial x_i} \right)^2 p' - \overline{a}^2 \frac{\partial^2 p'}{\partial x_i \partial x_i} = 0 \tag{3.31}$$

These equations allow an analytical solution for one-dimensional acoustics, which is given in the complex space by a linear combination of characteristic wave terms f and g defined as:

$$\check{p}(x,t) = \overline{\rho}\,\overline{a}\left[f(x,t) + g(x,t) \right], \tag{3.32}$$

$$\check{u}(x,t) = f(x,t) - g(x,t), \tag{3.33}$$

with

$$f(x,t) = \hat{f} \exp\left(i\omega t - i k_+ x\right), \tag{3.34}$$

$$g(x,t) = \hat{g} \exp\left(i\omega t - i k_- x\right). \tag{3.35}$$

The different propagation directions and velocities in upstream and downstream direction are given by the wave numbers:

$$k_{\pm} = \frac{\pm\omega/\overline{a}}{1 \pm M} \tag{3.36}$$

One-dimensional network models use these analytical solutions in order to discretise the geometry into distinct elements. This allows a very efficient calculation of acoustic eigenmodes and eigenvalues, yielding the frequency and the growth rate. Each geometry element is attributed a transfer matrix in terms of characteristic waves. The characteristic waves at upstream (1) and downstream (2) ends of a straight duct of length L can, for example, be related to each other as follows:

$$f_2 = f_1 \exp(-i\,k_+ L) \tag{3.37}$$

$$g_2 = g_1 \exp(-i\,k_- L) \tag{3.38}$$

Such connecting relations can be found for various types of elements in the literature, such as e.g. area changes or junctions. Flames can also be described by such connecting relations, which are given by the Rankine-Hugoniot relations, as described in [106]:

$$p_2' = p_1' - \left(\frac{\overline{T}_2}{\overline{T}_1} - 1\right)\overline{\rho}_1\overline{u}_1^2\left(\frac{\dot{Q}'}{\overline{\dot{Q}}} + \frac{u_1'}{\overline{u}_1}\right) \tag{3.39}$$

$$u_2' = u_1' + \left(\frac{\overline{T}_2}{\overline{T}_1} - 1\right)\overline{u}_1\left(\frac{\dot{Q}'}{\overline{\dot{Q}}} - \frac{p_1'}{\overline{p}_1}\right) \tag{3.40}$$

These relations can be expressed in the complex space using f and g:

$$\varsigma f_2 + \varsigma g_2 = f_1 + g_1 - \left(\frac{\overline{T}_2}{\overline{T}_1} - 1\right) M_1\left(\overline{u}_1\frac{\check{\dot{Q}}}{\overline{\dot{Q}}} + f_1 - g_1\right) \tag{3.41}$$

$$f_2 - g_2 = f_1 - g_1 + \left(\frac{\overline{T}_2}{\overline{T}_1} - 1\right)\left[\overline{u}_1\frac{\check{\dot{Q}}}{\overline{\dot{Q}}} - \gamma M_1(f_1 + g_1)\right] \tag{3.42}$$

with $\varsigma = \frac{\overline{\rho}_2\overline{a}_2}{\overline{\rho}_1\overline{a}_1}$.

At this point, the link between heat release rate fluctuations and acoustic perturbations appears. For predicting the stability of acoustic eigenmodes, one

needs to provide an accurate description of heat release rate fluctuations as a function of pressure and velocity perturbations. This is generally provided in the form of flame transfer functions (FTF), as introduced earlier. For longitudinal modes, they are generally put into relation with velocity disturbances, but they can also be formulated with respect to pressure disturbances, as e.g.:

$$\mathrm{FTF}_{p'} = \frac{\check{\dot{Q}}}{\overline{\dot{Q}}} \frac{\overline{p}}{\check{p}} \tag{3.43}$$

Network analyses will be performed in chapters 4 and 7, mainly to illustrate how some of the investigated feedback mechanisms might affect the system stability. The execution of extensive stability analyses is not the aim of the present work, but rather part of future work, based on the theoretical description of flame dynamics proposed here.

Nevertheless, a short outlook shall be given with respect to a more complex acoustic solver, namely the 3D solution of the convective wave equation. Using finite elements methods (FEM), three-dimensional acoustic eigenmodes can e.g. be computed on the basis of Eq. (3.30) for the case of zero mean flow. When dealing with thermoacoustic problems, this relation needs to be extended in order to account for unsteady heat release of the flame. This leads to the inhomogeneous wave equation for reacting flow, which reads as follows when neglecting turbulent flow noise, see Poinsot and Veynante [91]:

$$\frac{\partial^2 p'}{\partial t} - \frac{\partial}{\partial x_i}\left(\overline{a}^2 \frac{\partial p'}{\partial x_i}\right) = (\gamma - 1)\frac{\partial \dot{q}'}{\partial t} \tag{3.44}$$

The solution again requires models for heat release rate fluctuations, as these cannot be calculated by the acoustic solver itself. FEM tools offer great advantages for the analysis of transverse modes, since they do not impose a compactness assumption for the flame. Hence, if one provides accurate spatial distributions of flame transfer functions, transverse mode stability can be predicted, provided that acoustic losses are also correctly captured. Mean flow effects can also be considered in FEM calculations, by solving e.g. the linearised Euler equations, see Wieczorek [119], or the linearised Navier-Stokes equations, see Gikadi et al. [30].

The balancing between acoustic sources and sinks can be illustrated by introducing the transport equation for the acoustic energy

$$e_{ac} = \overline{\rho}\frac{u_i'^2}{2} + \frac{p'^2}{2\gamma\overline{p}}, \tag{3.45}$$

which can be derived from the wave equation (for zero mean flow) [104]:

$$\frac{\partial e_{ac}}{\partial t} + \frac{\partial p' u_i'}{\partial x_i} = \frac{\gamma - 1}{\overline{\rho}\overline{a}^2} p' \dot{q}'. \tag{3.46}$$

The relevance of the local Rayleigh index ri $\equiv \int_0^{\mathcal{T}} p' \dot{q}' dt$ clearly appears from this equation, since the product of pressure and heat release rate fluctuations acts as a source term. Hence, when its integral over an oscillation period is positive, i.e. ri > 0, the thermoacoustic feedback is positive. In the absence of viscous losses, the acoustic losses over the boundaries, expressed by the convective term in the equation above, need to outweigh the thermoacoustic term to ensure a stable combustion process. In industrial practice, it is hence important to correctly predict both the energy production and the acoustic losses; the present work focusses on the former.

4 Impact of Acoustic Pressure Perturbations on Auto-Ignition and Heat Release

This chapter presents a fundamental description of the thermoacoustic feedback caused by the pressure sensitivity of chemical reaction rates. This mechanism has been investigated theoretically in the context of premix flame propagation [14, 72, 98, 101, 121]. In thermoacoustic stability analysis of practical combustors, it is mostly neglected, see e.g. Ducruix et al. [24] and Huber et al. [44]. The main reason is the fact that commonly used correlations for laminar flame speed predict a comparatively small dependence on pressure and temperature variations, as concluded by Schuermans [104].

However, the previous work of Ni et al. [79] indicated that this effect would become more relevant when auto-ignition occurs due to high inlet temperatures. Indeed, auto-ignition flames do not rely on preheating of the fresh mixture by upstream diffusion of heat and therefore are generally considered to be more sensitive to pressure and temperature variations, relying solely on the Arrhenius description. In their work, Ni et al. considered only longitudinal modes and mainly focussed on variations of the ignition delay and subsequent flame movements. This approach was further developed by Zellhuber et al. in a first attempt [122], before yielding the general description introduced here, which has been published by the author in [126].

The description of the feedback mechanism is made in several steps. First, an idealised model framework is introduced, which considers auto-ignition flames as plug-flow reactors. This allows to derive a general relation between fluctuations of fuel mass flow, chemical formation rates, and heat release rate. The ansatz developed considers as well the precursor formation during the induction phase. Then, the sensitivity of chemical reaction rates to acoustic state changes is investigated using detailed chemistry calculations. The results are used in the following to derive flame transfer functions for per-

fect premix, compact auto-ignition flames and longitudinal modes. Eventually, the high flexibility of the analytical description allows to extend the description to non-linear system behaviour, technical premixing, and transverse modes. In addition, a straightforward extension of CFD methods based on tabulated chemistry is proposed to take into account the pressure sensitivity in realistic flame simulations.

4.1 General model formulation

4.1.1 Idealised auto-ignition flame structure

In Alstom's SEV combustor sketched in Fig. 2.1, cold fuel is injected as a cross-flow into the main stream of hot vitiated air coming from the high-pressure turbine. The turbulence level is high in order to achieve a fast mixing between the streams. The resulting mixture then enters the combustion chamber as a jet. Unlike in typical first-stage combustors, the mixture stream is not swirled, and therefore no central recirculation zone forms close to the burner axis, although small corner recirculation zones appear due to the area expansion behind the backward-facing step. The flow velocities are comparatively high and the flame stabilisation is ensured by the continuous auto-ignition of the fuel-air mixture.

For the fundamental description of the pressure/auto-ignition feedback mechanism, the initial mixing between fuel and oxidiser is idealised to be infinitely fast. In section 4.4.3, it will be discussed whether the model derived using this assumption can also be applied for technical premix conditions. The combustor can be modelled as a plug-flow reactor stretching along the burner axis, as sketched in Fig. 4.1. Hence, the mixture stream is represented as a series of "plugs", which are transported in space by convection [102]. The plugs are assumed to evolve independently of each other, i.e. diffusive effects are neglected, because of the high convection speed in the mixture stream. Within each plug, the temperature and composition distributions are assumed to be homogeneous. Hence, each single plug can be regarded as a homogeneous reactor evolving in time, but also in space, as it is convected downstream. The chemical reaction rates in a plug are therefore equal to those in a homoge-

neous reactor at the same conditions. This approach was already used in [122] and [95] for describing reheat combustors.

This modelling approach is rather unusual for gas turbine combustors. Instead, several studies were presented using well-stirred reactor approaches, see e.g. [49, 65]. These are well suited for premix swirl combustors, in which the intense central recirculation zone caused by the swirl breakdown forms a well-mixed region with a certain residence time, similar to the configuration of a well-stirred reactor. Such a representation is not adapted for reheat combustors without central recirculation zone; hence the plug-flow modelling was judged to be the most suitable for the present investigation of the pressure impact on chemical reaction rates.

In the model configuration shown in Fig. 4.1, the inlet is located at a position x_i, and the mixture is injected with an average velocity $\overline{u}_c$. The incoming oxidiser-fuel mixture will be subjected to plane acoustic waves f and g, which affect the build-up of radicals in the ignition delay phase and the subsequent heat release. As indicated by a standard Arrhenius description, the modulation of reaction rates is mainly due to temperature perturbations, which go along with the pressure perturbations, as explained earlier.

Rapid heat release will occur after a certain delay τ. In the simplified setup, the average flame position will thus be located at a position $\overline{x}_f = x_i + \overline{u}_c\overline{\tau}$. The auto-ignition delay is therefore the characteristic time lag of the system. Indeed, experimental and numerical investigations [59, 69] show that the auto-ignition flame position generally scales with the chemical ignition delay time and the convective velocity.

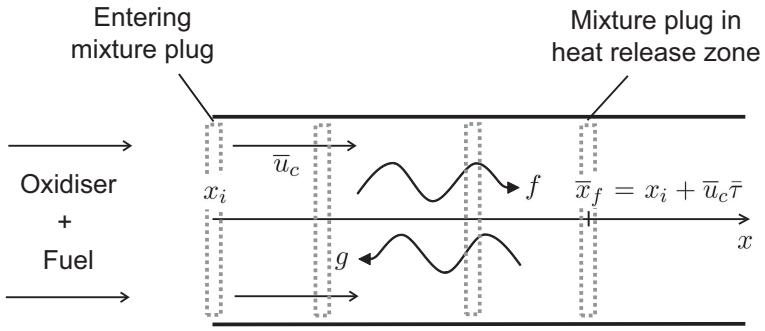

Figure 4.1: Sketch of the considered model setup

The momentary rate of heat release can be computed as a time-lagged history of fuel injection, i.e. the heat release rate at observation time t depends on the history of mass flow and ignition delay of the mixture injected at prior instants t_i. Hence, the momentary heat release is given by the integral over all plugs in the flame tube and can be expressed in terms of a Green's function:

$$\dot{Q}(t) = \int_{-\infty}^{t} G(t, t_i) d\, t_i \tag{4.1}$$

where in the simplest case of instantaneous heat release described by the Dirac δ-function:

$$G(t, t_i) = \Delta h_F^\circ \dot{m}_F(t_i) \delta\left(t - t_i - \tau(t_i)\right). \tag{4.2}$$

Under this assumption, the entire fuel quantity $\dot{m}_F(t_i) dt_i$ injected into the system at time t_i ignites and releases its reaction heat Δh_F° at time $t_i + \tau(t_i)$. The corresponding ignition delay $\tau(t_i)$ results from the entire history of perturbations encountered by the mixture and thus depends on the injection time t_i. In such a framework, heat release modulations can thus occur either by variations of the fuel mass flow or by changes in the ignition delay.

The models presented by Ni et al. [79] and Zellhuber et al. [122] used a description of this kind and directly related heat release rate fluctuations to changes in ignition delay. However, it does not allow to reproduce the modulation of the heat release intensity by acoustic perturbations, a fact that could be relevant for the flame response at higher frequencies, as discussed in [122].

Therefore, a more realistic description is introduced in the present work, based on the source term $\dot{\omega}_c(t, t_i)$ of a normalised progress variable c:

$$G(t, t_i) = \Delta h_F^\circ \dot{m}_F(t_i) \dot{\omega}_c(t, t_i). \tag{4.3}$$

This source term evolution can be obtained from homogeneous reactor calculations and is depicted in Fig. 3.1.

In [122], the source term evolution was approximated by a normal distribution centered around the time $t_i + \tau(t_i)$ and of spread σ, which is much shorter than the ignition delay ($\sigma \ll \tau$). This approximation allowed to explicitly include a fluctuating ignition delay; the spread was hereby assumed to be constant.

In the present work, the derivation is generalised for an arbitrary source term evolution $\dot{\omega}_c(t, t_i)$, which is split into an average and a fluctuating part. It is

shown later how this approach allows to retain both ignition delay and heat release intensity modulations.

4.1.2 Heat release rate modulations

In the context of thermoacoustic stability, perturbation terms affecting the heat release rate of the flame are of special interest. Looking at Eqs. (4.1) and (4.3), one can easily reckon that variations of fuel mass flow and progress variable source term will have such an effect. These two equations can be combined and rewritten including such perturbation terms:

$$\dot{Q}(t) = \int_{-\infty}^{t} \Delta h_F^\circ \left[\overline{\dot{m}}_F + \dot{m}'_F(t_i)\right] \left[\overline{\dot{\omega}}_c(t,t_i) + \dot{\omega}'_c(t,t_i)\right] dt_i. \tag{4.4}$$

It is emphasised that the mean source term $\overline{\dot{\omega}}_c(t,t_i)$ is not constant in time, but describes the evolution of an unperturbed reactor, which develops toward ignition under constant average conditions.

In thermoacoustic stability analysis, relative heat release rate modulations are generally used, which can be deduced from the previous equation[1]:

$$\frac{\dot{Q}'(t)}{\overline{\dot{Q}}} = \frac{\dot{Q}(t) - \overline{\dot{Q}}}{\overline{\dot{Q}}} = \int_{-\infty}^{t} \left\{ \left[1 + \frac{\dot{m}'_F(t_i)}{\overline{\dot{m}}_F} \right] \left[\overline{\dot{\omega}}_c(t,t_i) + \dot{\omega}'_c(t,t_i)\right] - \overline{\dot{\omega}}_c(t,t_i) \right\} dt_i. \tag{4.5}$$

Retaining only first order terms yields the following linearised form:

$$\frac{\dot{Q}'(t)}{\overline{\dot{Q}}} \approx \int_{-\infty}^{t} \left[\frac{\dot{m}'_F(t_i)}{\overline{\dot{m}}_F} \overline{\dot{\omega}}_c(t,t_i) + \dot{\omega}'_c(t,t_i) \right] dt_i. \tag{4.6}$$

Acoustic fluctuations can thus alter the heat release rate in two ways; either by modulating the fuel mass flow $\dot{m}_F$ and/or by influencing the chemical kinetic rates. For auto-ignition flames, the latter mechanism has the characteristic that it is not depending on the perturbations at a specific position and instant, but that it depends on the cumulated history of acoustic perturbations

[1] using the relation $\overline{\dot{Q}} = \overline{\dot{m}}_F \Delta h_F^\circ$ and the fact that the integral over the normalised progress variable source term curve equals unity, see also Sec. 4.2

to which a given volume element of premixture is subjected during the induction period. This results from the influence of the local acoustic perturbation level on the formation rate of radical species.

Equations (4.5) and (4.6) can be regarded as a general description, since it is not restricted to a certain type of perturbation. In the present work, the focus lies on the impact of acoustic pressure waves, for which a detailed chemistry study was performed. This will be presented in the following section. The description can nevertheless be also applied to mixture perturbations for example, as indicated by Zellhuber et al. in [128].

4.2 Detailed chemistry study on auto-ignition

In order to determine the heat release rate modulations, one has to compute the progress variable source term of homogeneous reactors, both unperturbed and perturbed, using the numerical tools introduced in section 3.1.1. All calculations in the present chapter were made for a mixture of fuel (pure methane, T=300 K) and lean combustion products (T=1300 K, $Y_{O_2} = 0.147$, $Y_{H_2O} = 0.0459$, $Y_{CO_2} = 0.0560$). Unless stated otherwise, the air-excess-ratio was chosen to be equal to $\lambda = 3$. The reference pressure was set to 18 bar.

4.2.1 Dynamics of auto-ignition processes under pressure variations

According to Eq. (4.6), the instantaneous disturbance of the progress variable source term is needed for obtaining the momentary heat release rate. As a consequence, the response of the source term to a perturbation is of special interest. Therefore a preliminary study was conducted by submitting chemical reactors to pressure disturbances in the form of rectangular impulse functions with an arbitrary window size of $t_{win} = 0.5 \cdot 10^{-3}$ s:

$$p'(t) = \begin{cases} \hat{p}, & t_{start} < t < t_{start} + t_{win} \\ 0, & \text{else} \end{cases} \tag{4.7}$$

The aim of this preliminary study is not to study explicitly the response to rectangular impulses, but to find a way to track the evolution of the reaction

progress source term as a function of the momentary perturbation. Therefore, two perturbation signals, that are shifted with respect to each other, were applied, with $t_{\text{start,early}} = 2.75 \cdot 10^{-3}$ s and $t_{\text{start,late}} = 3.25 \cdot 10^{-3}$ s. The recorded source term evolutions are compared to the ones obtained at constant pressure levels $p_{\text{low}} = \overline{p}$ and $p_{\text{high}} = \overline{p} + \hat{p}$. The four pressure signals considered are shown in Fig. 4.2.

The recorded source term evolutions are shown in Fig. 4.3, where they are plotted vs. time and progress variable. For better clarity only the relevant portions of the curves are shown. It is apparent that when plotted against time, the source term dynamics appear to be complex, as they significantly differ from the constant pressure reactors. However, this can be put into perspective when plotting the source terms vs. progress variable. The system dynamics can be described in good approximation as quasi-stationary, i.e. the source term in a reactor with varying pressure behaves as a constant pressure reactor of same reaction progress:

$$\dot{\omega}_{c,\text{var}}\left(p(t), c\right) \approx \dot{\omega}_{c,\text{stat}}\left(p = p(t), c\right). \tag{4.8}$$

This quasi-stationary behaviour significantly simplifies the description of the system dynamics, as only constant pressure data are needed for determining the instantaneous source term response. It has been confirmed for varying pressure and temperature levels, as well as for different starting times of the step signal. It is suitable in particular for linear analysis at small amplitudes, which is the main focus of this work. However at very high amplitudes and

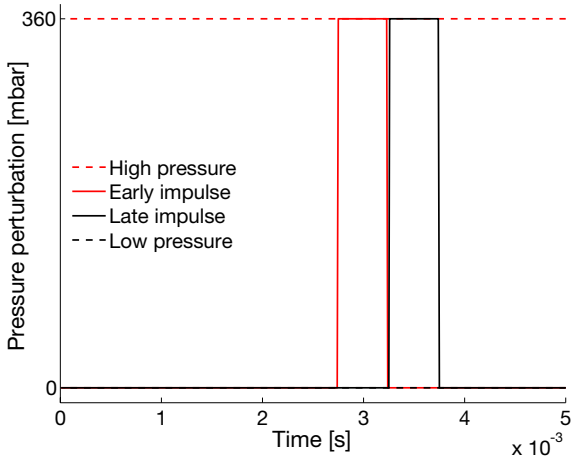

Figure 4.2: Time evolutions of pressure perturbations in reactors with constant pressure signals (low and high levels) and impulse pressure signals (early and late impulse)

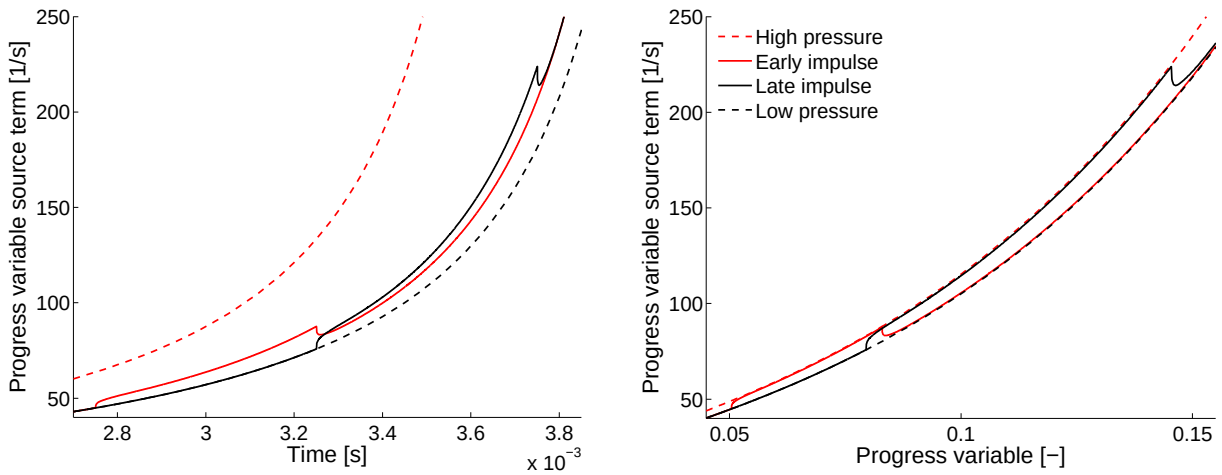

Figure 4.3: Details of progress source term evolutions in reactors with constant pressure signals (low and high levels) and impulse pressure signals (early and late impulse), plotted vs. time (left) and progress variable (right)

frequencies, strong temporal gradients of the acoustic pressure might limit the applicability of the approximation.

One can observe in the left plot of Fig. 4.3 an adaptation delay of around 2×10^{-5} s for the rectangular excitation with an amplitude $\hat{p}$ =360 mbar (2% of the reference pressure). At this amplitude range, deviations from the quasi-stationary behaviour can be estimated to significantly affect the flame response only in the frequency range above 10 kHz. This will be verified in section 4.2.4. Possible implications at higher amplitudes will be further addressed when treating the non-linear flame behaviour in section 4.4.2.

4.2.2 Pressure sensitivity

Following the observation of quasi-stationary behaviour, homogeneous reactors at constant pressure are investigated in detail. A pressure sensitivity is measured by comparing the formation rates of reaction progress $\dot{\omega}_c$ in reactors evolving at different constant pressure levels $\overline{p} + \hat{p}$. To this end, a non-dimensional pressure sensitivity parameter $\varphi_p(\hat{p}, c, \lambda)$ is introduced:

$$\varphi_p\left(\hat{p}, c, \lambda\right) = \frac{\dot{\omega}'_c\left(\hat{p}, c, \lambda\right)}{\dot{\omega}_c\left(\overline{p}, c, \lambda\right)} \frac{\overline{p}}{\hat{p}}, \tag{4.9}$$

with λ denoting the air-excess ratio (viz. the inverse function of equivalence ratio). Figure 4.4 shows the variations of this sensitivity factor vs. reaction progress for various levels of pressure deviation and lean mixing conditions. Lean conditions are of special interest for the industrial application in low NO_X gas turbine combustors.

The evolutions of φ_p are plotted vs. a normalised time and the progress variable, respectively. Looking at the temporal evolutions, it appears that for all mixing conditions a similar, nearly constant level is obtained throughout the induction period. Furthermore, comparing two different amplitude levels for $\lambda = 3$, the linearity of the process can be well established. However, it can be noted that the pressure sensitivity drops down during the short heat release phase, especially for richer conditions. This becomes very much apparent when plotting vs. progress variable, since this representation allows to better resolve the heat release phase. The influence of this bending will be investigated at a later point.

In particular during the induction period, the pressure sensitivity factor does not show a strong dependence on the air-excess-ratio. This observation is used in section 4.4.3 when discussing the applicability of the model framework to technical premix cases. In the meantime, as an approximation, a con-

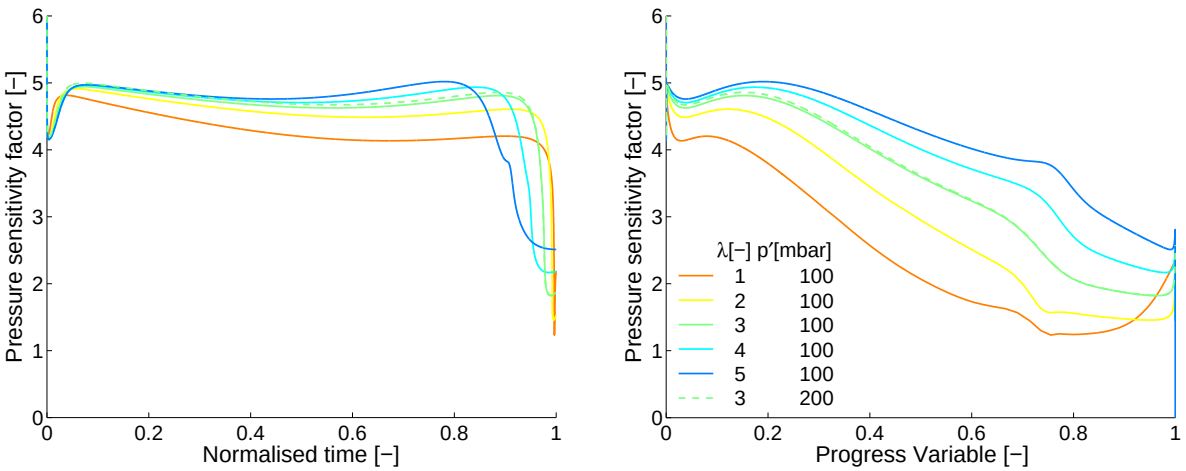

Figure 4.4: Evolutions of pressure sensitivity in homogeneous reactors of varying air-excess ratio and pressure disturbance amplitudes, plotted vs. normalised time (left) and progress variable (right)

stant specific pressure sensitivity factor φ_p can thus be defined for a given oxidiser/fuel pair.

The numerical values shown in Fig. 4.4 are comparable to the ones that can be obtained from the semi-empirical correlations of Spadaccini and Colket [114], as used by Ni et al. [79]. One obtains pressure sensitivity factors between 3.3 and 3.4 using the correlations for the mixture range considered here.

4.2.3 Heat release of perturbed homogeneous reactors

The sensitivity factor can now be used in a model to predict ignition delays of homogeneous reactors subjected to time-varying pressure conditions. This corresponds to the analysis of a single mixture plug streaming along the straight tube in the presence of acoustic perturbations, as shown in Fig. 4.1. Hence, in the present section, the reaction source term is not expressed as a function of global time t and injection instant t_i, but merely as a function of the lifetime t^+ of the single plug considered. This is done in order to improve the readability.

The description relies on the temporal evolution equation of the ignition progress in such a plug or homogeneous reactor:

$$\overline{\dot{\omega}}_c\left(t^+\right) + \dot{\omega}'_c\left(t^+\right) = \overline{\dot{\omega}}_c\left(c\right)\left[1 + \varphi_p \frac{p'(t^+)}{\overline{p}}\right] \tag{4.10}$$

As mentioned earlier, the instantaneous source term $\dot{\omega}_c(t^+)$ can be expressed as the sum of the source term in the reference reactor at time t^+ and a fluctuation term, see the LHS of Eq. (4.10). Furthermore, the previous study on chemical reactors showed that the instantaneous source term can be expressed using the pressure sensitivity and a progress variable based mapping of the source term in the reference reactor, see the RHS of Eq. (4.10). The reaction progress in the perturbed reactor at time t^+ is denoted by c. Hence, in the reference reactor, this reaction progress value will be attained at a different time $T^+ \neq t^+$. This is also shown schematically in Fig. 4.5. One can thus conclude that

$$\overline{\dot{\omega}}_c\left(c\right) = \overline{\dot{\omega}}_c\left(T^+\right) \neq \overline{\dot{\omega}}_c\left(t^+\right). \tag{4.11}$$

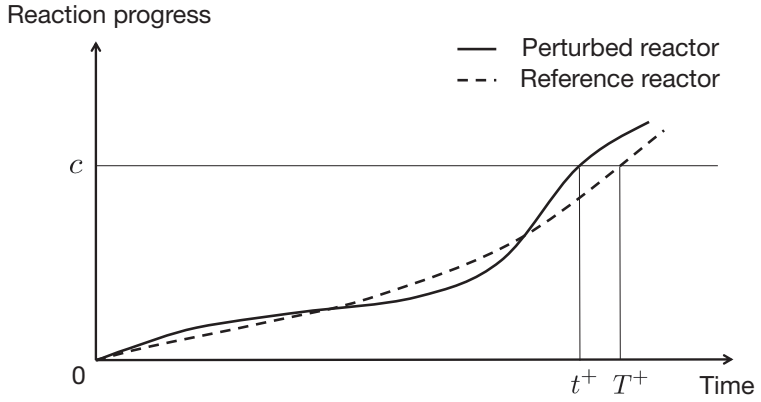

Figure 4.5: Schematical description of time delay between perturbed and reference reactor

In order to be able to use Eq. (4.10) in an analytical model, one needs to establish the relation between time instants t^+ and T^+. Therefore, Eq. (4.10) can be reformulated as a separable differential equation using $\frac{dc}{dt^+} = \overline{\dot{\omega}}_c\left(t^+\right) + \dot{\omega}'_c\left(t^+\right)$:

$$\frac{dc}{\overline{\dot{\omega}}_c(c)} = \left[1 + \varphi_p \frac{p'(t^+)}{\overline{p}}\right] dt^+, \tag{4.12}$$

which can be integrated over the lifetime t^+:

$$\int_0^c \frac{dc}{\overline{\dot{\omega}}_c(c)} = \int_0^{t^+} \left[1 + \varphi_p \frac{p'(t)}{\overline{p}}\right] dt. \tag{4.13}$$

The LHS of Eq. (4.13) is equal to the time T^+, i.e. the time at which the reference reactor reaches a progress level of c, thus:

$$T^+ = t^+ + \int_0^{t^+} \varphi_p \frac{p'(t)}{\overline{p}} dt. \tag{4.14}$$

Hence, one obtains using Eqs. (4.11) and (4.14) in Eq. (4.10):

$$\overline{\dot{\omega}}_c\left(t^+\right) + \dot{\omega}'_c\left(t^+\right) = \overline{\dot{\omega}}_c\left(t^+ + \int_0^{t^+} \varphi_p \frac{p'(t)}{\overline{p}} dt\right)\left[1 + \varphi_p \frac{p'(t^+)}{\overline{p}}\right]. \tag{4.15}$$

After a first order Taylor expansion and assuming small perturbation amplitudes, the requested source term deviation of a perturbed reactor reads as follows:

$$\dot{\omega}'_c\left(t^+\right) \approx \overline{\dot{\omega}}_c\left(t^+\right) \varphi_p \frac{p'(t^+)}{\overline{p}} + \int_0^{t^+} \varphi_p \frac{p'(t)}{\overline{p}} dt \frac{d\overline{\dot{\omega}}_c\left(t^+\right)}{dt^+}. \tag{4.16}$$

Physically speaking, the chemical kinetics respond in a twofold manner to a pressure disturbance: The first term on the RHS of Eq. (4.16) modulates the

intensity of the heat release by responding to the instantaneous pressure disturbance. The second term accounts for the accumulation of previous perturbations and the corresponding time shift $T^+ - t^+$ between the perturbed and the reference reactors. Pressure variations can therefore affect both intensity and timing of the heat release in a considerable manner, since pressure sensitivity factors much larger than unity were computed (see Fig. 4.4).

At this point, a short remark on the linearity requirement needed for deriving Eq. (4.16) from Eq. (4.15) is called for. The linear approximation is made for a function featuring large gradient values, since the heat release phase is very short. Thus, linear behaviour can only be expected for delay disturbances $T^+ - t^+ \ll \sigma$. As a consequence, non-linear flame response might appear already at moderate perturbation amplitudes of a few percent, as was already pointed out in [128]. Nevertheless, the linear assumption is valid, when dealing only with system stability. Limit cycle predictions will on the contrary ask for special non-linear treatment of the flame response, as will be presented later.

4.2.4 Validation and interpretation

The relations obtained for delay and heat release disturbances need to be validated with actual reactor calculations, before making further use of them in the derivation of heat release rate modulations. As a validation case, it was chosen to study how chemical reactors respond to sinusoidal pressure signals of varying frequency. At first the delay relation of Eq. (4.14) shall be tested. Therefore, the ignition delay τ is defined as the point at which a reaction progress of $c = 0.5$ is reached. The delay in the reference reactor shall be denoted by $\overline{\tau}$; according to Eq. (4.14) the delay in the perturbed reactor reads as

$$\overline{\tau} + \tau' = \overline{\tau} - \int_0^{\overline{\tau}} \varphi_p \frac{p'(t)}{\overline{p}} dt. \tag{4.17}$$

The delay perturbation τ' can hence be calculated explicitly for any type of time-dependent pressure excitation signal. The validation can be made by comparing it to homogeneous reactor calculations performed under varying pressure, as used in section 4.2.1. The comparison is made in Fig. 4.6 for the ignition delay response to the sinusoidal pressure excitation with varying fre-

quency. In addition, the plot shows the result obtained when accounting for a pressure sensitivity depending on the ignition progress $\varphi_p(c)$. The latter result can be obtained from a time integration of Eq. (4.10) and allows to check whether it is acceptable to assume a constant pressure sensitivity.

This assumption clearly does not affect the prediction of delay disturbances, since no significant variation can be observed between both model predictions. When comparing the model predictions with the reactor calculations, one can see that the global trend is correct. The ignition delay variation results as the cumulative integral of positive and negative pressure variations, which explains the reduced amplitudes at higher frequencies. Similar results were obtained by Bansal et al. [4], who studied the response of ignition delays to temperature variations only.

A small vertical shift can however be observed between the results of the analytical model and the numerical simulation. This vertical shift appears also for sinusoidal excitations with different phase. This indicates a slightly non-linear behaviour of excited reactors, as the positive modulations seem to outweigh the negative ones. Such a behaviour could be explained by the exponential temperature dependence in the Arrhenius relation. For the remainder of this work, this continuous shift does however not have any significance, since it only leads to a shift of the reference level, and hence does not affect fluctuation terms. It is further emphasised that the model accuracy is equally

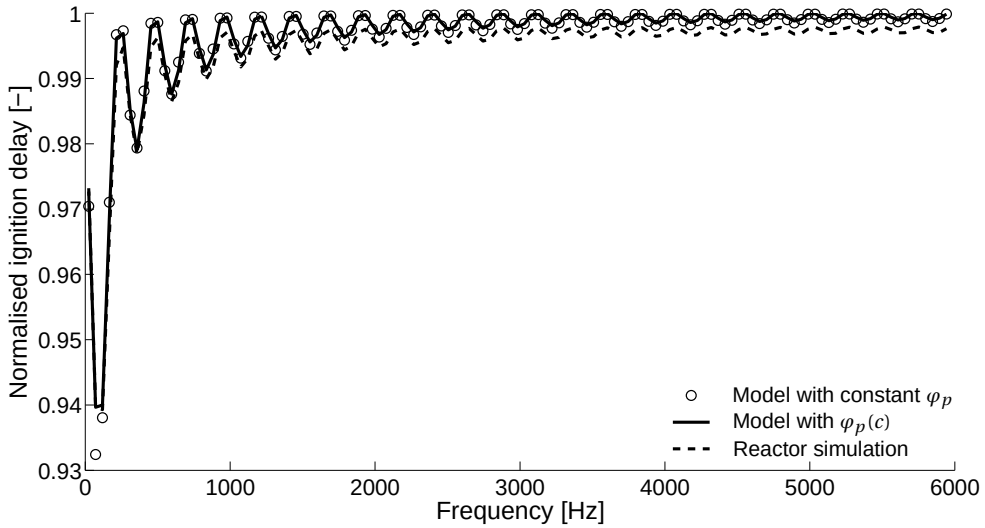

Figure 4.6: Comparison of ignition delays obtained from reactor simulations and model predictions (2% excitation amplitude)

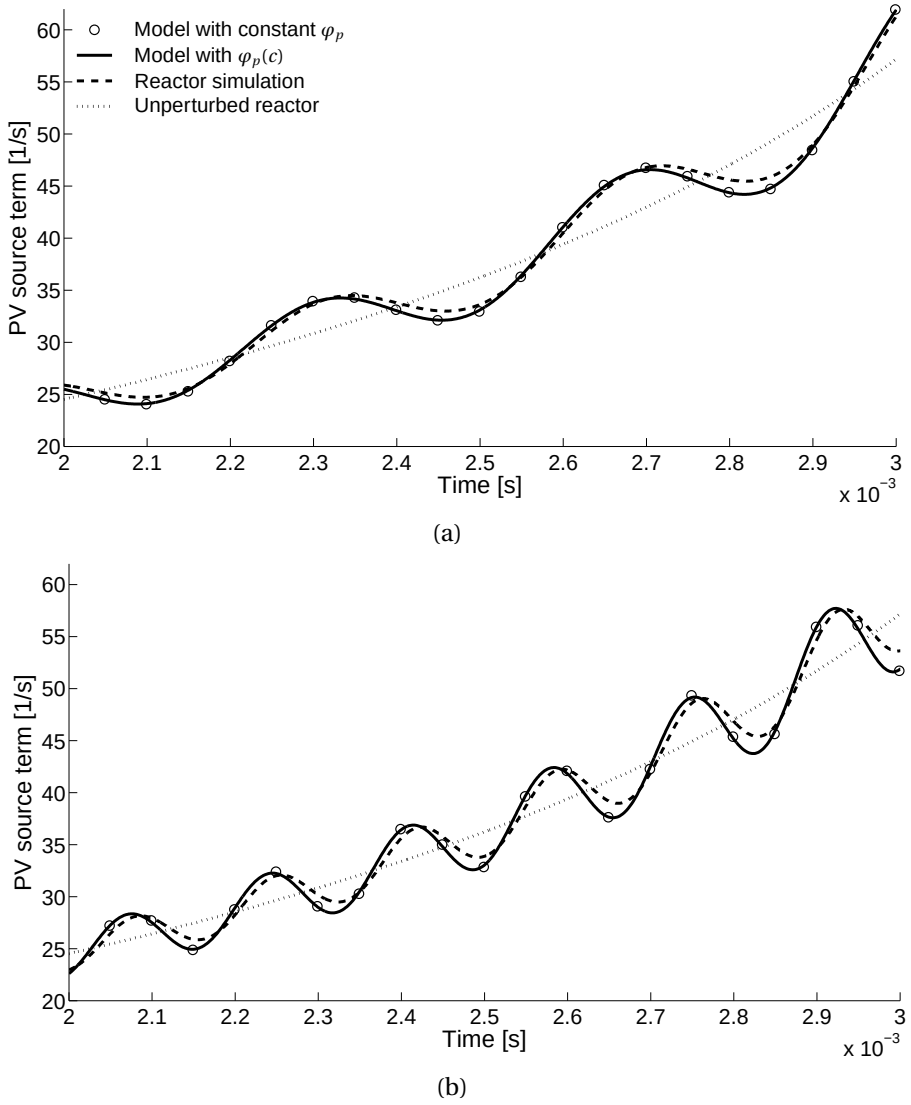

Figure 4.7: Comparison of progress variable source terms obtained from reactor simulations and model predictions (2% excitation amplitude, a: $f = 2960$ Hz, b: $f = 5920$ Hz)

good at high frequencies. Unlike the model prediction, the simulation of excited homogeneous reactors does not make use of the assumption of quasi-stationary behaviour. If this approximation was not fulfilled anymore at high frequencies, one would expect larger deviations between model and simulation, which are not observed here.

The time delaying effect and hence the second term on the RHS of Eq. (4.16) are thus correctly predicted by the model. The verification of the global expression of Eq. (4.16) can as well be conducted by comparing the temporal evolutions of the progress variable source term. This was also made for the sinusoidal excitation and the results are shown for two distinct frequencies

in Fig. 4.7. For better clarity, only a short lapse of time is depicted. Source term evolutions are again plotted for a full reactor calculation, as well as for the model predictions with constant and varying φ_p. A further comparison is made with the reference source term evolution in the unperturbed reactor. The model predictions capture accurately the source term modulations. This is consistent with the successful comparison of the delay predictions made before. The evolutions also nicely illustrate how the chemical reaction rates are modulated by the isentropic state changes.

The deviations appearing in particular during low pressure periods are in line with the previously commented discrepancies of ignition delay predictions, which are probably due to the exponential Arrhenius formulation. Comparing the two plots of Fig. 4.7, it is observed that deviations tend to grow for increasing frequencies. This indicates a limitation of the quasi-stationary assumption; nevertheless, the resulting inaccuracies are small in the frequency range of interest.

The previous analysis of chemical reactor evolutions under fluctuating pressure conditions yielded the requested relation of heat release deviations for the calculation of flame transfer functions of auto-ignition flames. The quantification relies on the definition of a pressure sensitivity factor φ_p, which shows little variations for wide ranges of mixture and reaction states, and allows a simplified mathematical description of the disturbed system dynamics.

4.3 Derivation of flame transfer functions

4.3.1 Inclusion of detailed chemistry data

A general expression for heat release modulations at observation time t can be obtained from the combination of Eqs. (4.6) and (4.16):

$$\frac{\dot{Q}'(t)}{\overline{\dot{Q}}} = \int_{-\infty}^{t} \left\{ \frac{\dot{m}'_F(t_i)}{\overline{\dot{m}}_F} \overline{\dot{\omega}}_c(t-t_i) + \overline{\dot{\omega}}_c(t-t_i)\,\varphi_p \frac{p'\left(x_i+(t-t_i)\overline{u}_c, t\right)}{\overline{p}} + \int_{t_i}^{t} \varphi_p \frac{p'\left(x_i+(t^+-t_i)\overline{u}_c, t^+\right)}{\overline{p}} dt^+ \frac{d\overline{\dot{\omega}}_c(t-t_i)}{dt} \right\} dt_i. \quad (4.18)$$

This equation holds for a one-dimensional setup as shown in Fig. 4.1, where the unburnt fluid is convected with constant velocity $\overline{u}_c$. Higher order terms are neglected, thus the instantaneous pressure level is calculated along the convective characteristic $x = x_i + (t - t_i)\overline{u}_c$ as done in Eq. (4.18). For constant premixing, the variations of fuel mass flow can be expressed as a function of the acoustic perturbations at the inlet position x_i:

$$\frac{\dot{m}'_F(t_i)}{\overline{\dot{m}}_F} = \frac{u'(x_i,t_i)}{\overline{u}_c} + \frac{1}{\gamma}\frac{p'(x_i,t_i)}{\overline{p}}. \tag{4.19}$$

4.3.2 Application to planar acoustic waves

Whereas the previous expressions were all expressed in the time domain with real fluctuation values, the complex notation is employed in the following to derive flame transfer functions. In the framework of plane harmonic waves with mean flow, the complex acoustic fluctuations $\check{p}$ and $\check{u}$ are expressed using Riemann invariants:

$$\check{p}(x,t) = \overline{\rho}_c \overline{a}_c \left[f(x,t) + g(x,t) \right], \tag{4.20}$$

$$\check{u}(x,t) = f(x,t) - g(x,t), \tag{4.21}$$

with

$$f(x,t) = \hat{f} \exp\left(i\omega t - \frac{i\omega x}{(1+M_c)\overline{a}_c} \right), \tag{4.22}$$

$$g(x,t) = \hat{g} \exp\left(i\omega t + \frac{i\omega x}{(1-M_c)\overline{a}_c} \right). \tag{4.23}$$

Herein, the mean density, the speed of the sound, and the corresponding Mach number in the cold mixture are denoted by $\overline{\rho}_c$, $\overline{a}_c$, and M_c, respectively.

Since Eq. (4.18) is composed of additive terms, the respective contributions of the left and right running waves can be calculated separately. The contribution of the left running wave to heat release modulations $\left.\frac{\check{\dot{Q}}(t)}{\overline{\dot{Q}}}\right|_f$ can be calcu-

lated by setting $\hat{g}$=0. When doing this, the acoustic disturbance terms read as follows:

$$\left.\frac{\check{\dot{m}}_F(t_i)}{\overline{\dot{m}}_F}\right|_f = \left(\frac{\hat{f}}{\overline{u}_c} + \frac{\overline{\rho}_c \overline{a}_c \hat{f}}{\gamma \overline{p}}\right) \exp\left(i\omega t_i - \frac{i\omega x_i}{(1+M_c)\overline{a}_c}\right) \tag{4.24}$$

$$\left.\varphi_p \frac{\check{p}\left(x_i + (t-t_i)\overline{u}_c, t\right)}{\overline{p}}\right|_f = \varphi_p \frac{\overline{\rho}_c \overline{a}_c \hat{f}}{\overline{p}} \exp\left(\frac{i\omega}{1+M_c}\left(t + M_c t_i - M_c \frac{x_i}{\overline{u}_c}\right)\right) \tag{4.25}$$

$$\begin{aligned}\left.\int_{t_i}^{t} \varphi_p \frac{\check{p}\left(x_i + (t^+ - t_i)\overline{u_c}, t^+\right)}{\overline{p}} dt^+\right|_f = {} & \varphi_p \frac{\overline{\rho}_c \overline{a}_c \hat{f}}{\overline{p}} \frac{1+M_c}{i\omega} \\ & \cdot \exp\left(\frac{i\omega}{1+M_c}\left(M_c t_i - M_c \frac{x_i}{\overline{u}_c}\right)\right) \\ & \cdot \left[\exp\left(\frac{i\omega t}{1+M_c}\right) - \exp\left(\frac{i\omega t_i}{1+M_c}\right)\right].\end{aligned} \tag{4.26}$$

The calculation of heat release modulations asks for an integration over the history of fuel injection, which appears to be very tedious only at first sight. Actually, it can be solved in a fairly simple way by introducing the Fourier transform of the progress variable source term, centered around the mean ignition delay $\overline{\tau}$:

$$\mathscr{F}_{\dot{\overline{\omega}}_c}(\omega) = \int_{-\infty}^{+\infty} \exp(-i\omega t^+) \dot{\overline{\omega}}_c(t^+ + \overline{\tau}) dt^+. \tag{4.27}$$

Hence, using Eqs. (4.24) to (4.27) in Eq. (4.18) and applying the integration rules of the Fourier transform, one obtains:

$$\begin{aligned}\left.\frac{\check{\dot{Q}}(t)}{\overline{\dot{Q}}}\right|_f = {} & \left(\frac{\hat{f}}{\overline{u}_c} + \frac{\overline{\rho}_c \overline{a}_c \hat{f}}{\gamma \overline{p}}\right) \exp\left(i\omega t - \frac{i\omega x_i}{(1+M_c)\overline{a}_c}\right) \mathscr{F}_{\dot{\overline{\omega}}_c}(\omega) \exp\left(-i\omega\overline{\tau}\right) \\ & + \varphi_p (1+M_c) \frac{\overline{\rho}_c \overline{a}_c \hat{f}}{\overline{p}} \exp\left(i\omega t - \frac{i\omega x_i}{(1+M_c)\overline{a}_c}\right) \\ & \cdot \mathscr{F}_{\dot{\overline{\omega}}_c}\left(\frac{\omega M_c}{1+M_c}\right) \exp\left(-\frac{i\omega M_c}{1+M_c}\overline{\tau}\right) \\ & - \varphi_p (1+M_c) \frac{\overline{\rho}_c \overline{a}_c \hat{f}}{\overline{p}} \exp\left(i\omega t - \frac{i\omega x_i}{(1+M_c)\overline{a}_c}\right) \mathscr{F}_{\dot{\overline{\omega}}_c}(\omega) \exp\left(-i\omega\overline{\tau}\right).\end{aligned} \tag{4.28}$$

This relation can be rewritten in the following form by introducing the mean flame position $\overline{x}_f = x_i + \overline{u}_c\overline{\tau}$:

$$\begin{aligned}\left.\frac{\check{\dot{Q}}(t)}{\overline{\dot{Q}}}\right|_f &= \left(\frac{1}{\overline{u}_c} + \frac{\overline{\rho}_c\overline{a}_c}{\gamma\overline{p}}\right) f(x_i,t)\mathscr{F}_{\overline{\dot{\omega}}_c}(\omega)\exp\left(-i\omega\overline{\tau}\right)\\ &\quad + \varphi_p(1+M_c)\frac{\overline{\rho}_c\overline{a}_c}{\overline{p}} f(\overline{x}_f,t)\mathscr{F}_{\overline{\dot{\omega}}_c}\left(\frac{\omega M_c}{1+M_c}\right)\\ &\quad - \varphi_p(1+M_c)\frac{\overline{\rho}_c\overline{a}_c}{\overline{p}} f(x_i,t)\mathscr{F}_{\overline{\dot{\omega}}_c}(\omega)\exp\left(-i\omega\overline{\tau}\right). \end{aligned} \tag{4.29}$$

A graphical representation of the flame transfer function follows in section 4.3.4, as well as a discussion of its frequency response.

The contribution of the left running wave can be calculated in an analogous manner:

$$\begin{aligned}\left.\frac{\check{\dot{Q}}(t)}{\overline{\dot{Q}}}\right|_g &= \left(-\frac{1}{\overline{u}_c} + \frac{\overline{\rho}_c\overline{a}_c}{\gamma\overline{p}}\right) g(x_i,t)\mathscr{F}_{\overline{\dot{\omega}}_c}(\omega)\exp\left(-i\omega\overline{\tau}\right)\\ &\quad + \varphi_p(1-M_c)\frac{\overline{\rho}_c\overline{a}_c}{\overline{p}} g(\overline{x}_f,t)\mathscr{F}_{\overline{\dot{\omega}}_c}\left(\frac{\omega M_c}{1-M_c}\right)\\ &\quad - \varphi_p(1-M_c)\frac{\overline{\rho}_c\overline{a}_c}{\overline{p}} g(x_i,t)\mathscr{F}_{\overline{\dot{\omega}}_c}(\omega)\exp\left(-i\omega\overline{\tau}\right). \end{aligned} \tag{4.30}$$

The total heat release modulations caused by plane harmonic waves thus read as the sum of the two previous equations:

$$\begin{aligned}\frac{\check{\dot{Q}}(t)}{\overline{\dot{Q}}} &= \left(1-\varphi_p\gamma M_c^2\right)\frac{\check{u}(x_i,t)}{\overline{u}_c}\mathscr{F}_{\overline{\dot{\omega}}_c}(\omega)\exp\left(-i\omega\overline{\tau}\right)\\ &\quad - \left(\varphi_p - \frac{1}{\gamma}\right)\frac{\check{p}(x_i,t)}{\overline{p}}\mathscr{F}_{\overline{\dot{\omega}}_c}(\omega)\exp\left(-i\omega\overline{\tau}\right)\\ &\quad + \varphi_p(1+M_c)\frac{\overline{\rho}_c\overline{a}_c}{\overline{p}} f(\overline{x}_f,t)\mathscr{F}_{\overline{\dot{\omega}}_c}\left(\frac{\omega M_c}{1+M_c}\right)\\ &\quad + \varphi_p(1-M_c)\frac{\overline{\rho}_c\overline{a}_c}{\overline{p}} g(\overline{x}_f,t)\mathscr{F}_{\overline{\dot{\omega}}_c}\left(\frac{\omega M_c}{1-M_c}\right). \end{aligned} \tag{4.31}$$

4.3.3 Interpretation of the heat release modulations

Equation (4.31) can be used in network models for the stability assessment of 1D configurations. It only asks for the Fourier transform of the progress

variable source term and the mean value of the pressure sensitivity, which can be obtained from only two homogeneous reactor calculations.

In order to facilitate the physical interpretation of this relation, it can additionally be assumed that the Mach number is very small, such that only first order Mach number terms are retained. Then, Eq. (4.31) simplifies to:

$$\frac{\check{\dot{Q}}(t)}{\overline{\dot{Q}}} = \left[\frac{\check{u}(x_i,t)}{\overline{u}_c} - \left(\varphi_p - \frac{1}{\gamma}\right) \frac{\check{p}(x_i,t)}{\overline{p}} \right] \mathscr{F}_{\overline{\dot{\omega}}_c}(\omega) \exp\left(-i\omega\overline{\tau}\right) + \varphi_p \frac{\check{p}(\overline{x}_f,t)}{\overline{p}} \mathscr{F}_{\overline{\dot{\omega}}_c}(\omega M_c) \,. \tag{4.32}$$

The last term herein plays a tremendous role concerning the stability of the configuration, since it introduces a direct proportionality between the pressure fluctuations at the flame and the heat release. As mentioned in section 4.2, the progress variable source term can be approximated by a normal distribution centered around $\overline{\tau}$ and of spread σ. The corresponding Fourier transform according to Eq. (4.27) is given by $\mathscr{F}_{log}(\omega) = \exp(-\frac{\omega^2\sigma^2}{2})$.

Still assuming that $M_c \ll 1$, one can write $\mathscr{F}_{log}(\omega M_c) = \exp(-\frac{\omega^2\sigma^2 M_c^2}{2}) \approx 1$ and thus get the following approximation of the heat release modulations:

$$\left.\frac{\check{\dot{Q}}(t)}{\overline{\dot{Q}}}\right|_{log} \approx \left[\frac{\check{u}(x_i,t)}{\overline{u}_c} - \left(\varphi_p - \frac{1}{\gamma}\right) \frac{\check{p}(x_i,t)}{\overline{p}} \right] \exp\left(-i\omega\overline{\tau} - \frac{\omega^2\sigma^2}{2}\right) + \varphi_p \frac{\check{p}(\overline{x}_f,t)}{\overline{p}}. \tag{4.33}$$

The first term on the RHS of Eq. (4.33) decays exponentially with increasing frequency. Hence, at medium to high frequencies the second term will clearly dominate and lead to high positive values of the Rayleigh index in this range.

The upcoming section will proceed to a verification of the derived flame transfer functions and to a parameter study for the impact of air excess ratio.

4.3.4 Verification of heat release modulations

The derived expressions were verified against the output of the 1D, time-domain simulation of the plug flow reactor introduced in section 3.1.3.

For simplicity, the acoustic excitation only consisted of a f-wave. Simulation runs were performed for varying frequencies, and the flame response was analysed using a Fourier transform of the time series at the excitation

frequency. The flame transfer function in the simulation $\mathrm{FTF}_{p',sim}(\omega)$ reads as the ratio between the FFTs of heat release and pressure at the mean flame position:

$$\mathrm{FTF}_{p'(\overline{x}_f),sim}(\omega) = \left.\frac{\check{\dot{Q}}_{sim}}{\overline{\dot{Q}}_{sim}}\right|_{\omega} \left.\frac{\overline{p}_{sim}}{\check{p}_{sim}(\overline{x}_f)}\right|_{\omega}^{-}. \tag{4.34}$$

The model prediction can be compared to these results by rewriting Eq. (4.29) as a flame transfer function $\mathrm{FTF}_{p,mod}(\omega)$, i.e. dividing it by the pressure at the flame position. This corresponds to a conversion into frequency domain:

$$\mathrm{FTF}_{p'(\overline{x}_f),mod}(\omega) = \left.\frac{\check{\dot{Q}}(t)}{\overline{\dot{Q}}}\right|_{f} \frac{\overline{p}}{\overline{\rho}_c \overline{a}_c f(x_f,t)} \tag{4.35}$$

$$\begin{aligned}\mathrm{FTF}_{p'(\overline{x}_f),mod}(\omega) = &\left[\frac{\overline{\rho}_c \overline{a}_c}{\overline{u}_c \overline{p}} + \frac{1}{\gamma} - \varphi_p(1+M_c)\right] \mathscr{F}_{\dot{\overline{\omega}}_c}(\omega) \exp\left(\frac{-i\omega\overline{\tau}}{1+M_c}\right) \\ &+ \varphi_p(1+M_c)\mathscr{F}_{\dot{\overline{\omega}}_c}\left(\frac{\omega M_c}{1+M_c}\right).\end{aligned} \tag{4.36}$$

The comparison between the two results is shown for amplitude and phase in Fig. 4.8 for an arbitrary flame setup with a Mach number set to $M_c = 0.058$. As before, the mixture is composed of pure methane and vitiated air, with the air-excess-ratio first set to $\lambda = 3$. For these conditions, the average pressure sensitivity is equal to 4.84 and the ignition delay to 4.19×10^{-3} s. An approximate spread σ can be estimated from the full width at half maximum (FWHM) of the source term curve using $\sigma = \mathrm{FWHM}/\left(2\sqrt{2\ln 2}\right)$. This yields a value of $\sigma = 2.16 \times 10^{-5}$ s.

Two different curves are given for the simulation results, for varying and constant φ_p. One can observe that the variation of the pressure sensitivity along the reactor evolution indeed has an impact on the flame response: by assuming a constant φ_p, the phase prediction is fairly well reproduced, whereas the amplitude is slightly overestimated. This is an important result regarding industrial burner design, since the presented model relies on the assumption of a constant pressure sensitivity. By doing this, no significant error is made on the phase prediction, which is of particular importance for thermoacoustic stability. The overestimation of the response amplitude can be regarded as a

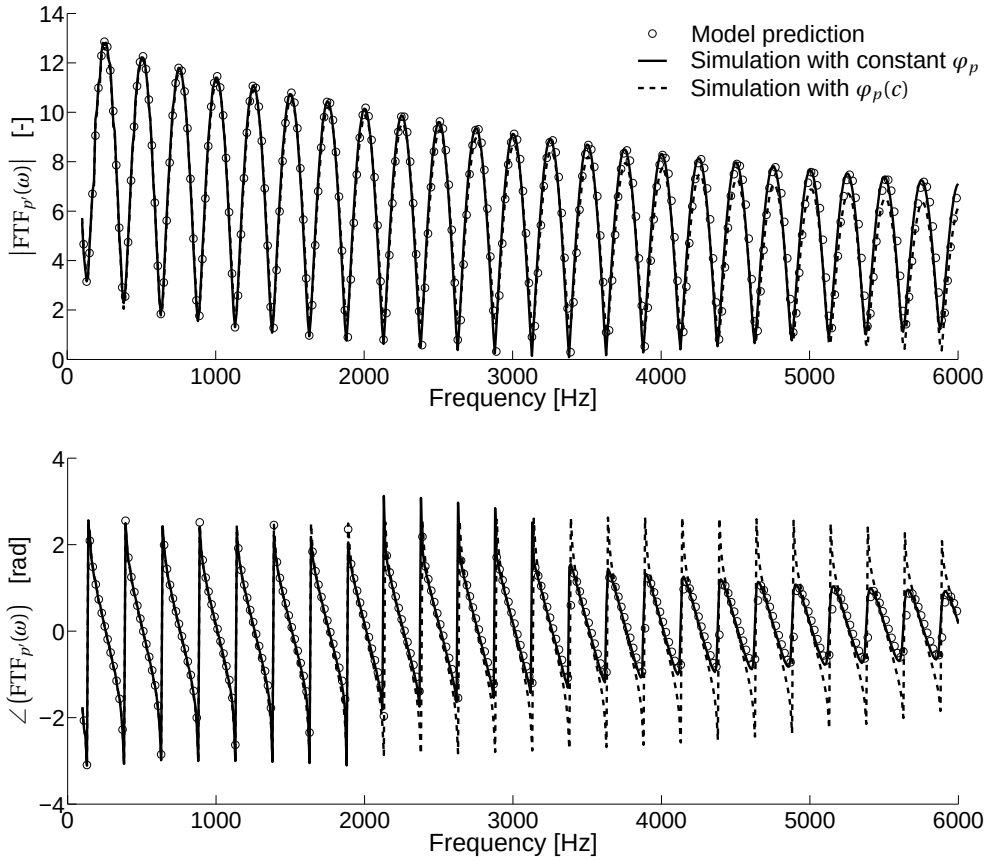

Figure 4.8: Comparison between model predictions and simulation results for FTF regarding f-waves (top: amplitude, bottom: phase)

worst-case scenario, and thus leads to a safety margin regarding the stability prediction.

The model prediction of Eq. (4.36) delivers a nearly perfect match with the simulation results using a constant pressure sensitivity. The presented mathematical description of modulations of heat release intensity and ignition delay therefore properly captures the physics in a one-dimensional auto-ignition flame, as it is simulated here. The model thus allows to precisely predict the flame response by doing only two constant pressure reactor calculations, in order to retrieve the evolution of the mean chemical source term and the average value of the pressure sensitivity factor.

For the sake of completeness, Fig. 4.9 shows the real parts of the flame transfer functions obtained for various lean air-excess ratios. It can be regarded as a direct measure for the Rayleigh criterion, and thus for the thermoacoustic

source term. As a reminder, the Rayleigh index RI of a compact flame over the period of oscillation $\mathcal{T}$ is defined as follows using real fluctuation values:

$$\mathrm{RI} = \int_0^{\mathcal{T}} p'(\overline{x}_f, t)\dot{Q}'(t)\,dt. \tag{4.37}$$

It can be shown that RI and $\Re(\mathrm{FTF}_{p'(\overline{x}_f)})$ are of the same sign (see e.g. Schuermans [104]), hence cases with $\Re(\mathrm{FTF}_{p'(\overline{x}_f)}) > 0$ indicate a positive thermoacoustic source term.

All evolutions shown in Fig. 4.9 are similar in shape, and the model prediction works fine in all cases. As mentioned earlier, the assumption of a constant pressure sensitivity generally leads to a slight overestimation of the coupling at high frequencies, which appears acceptable regarding the high degree of simplification of the model.

One can observe that for leaner mixtures the flame response converges more quickly to a constant high level. This tendency can be explained by the different terms constituting the flame response and the mixture dependence of the progress variable source term. In Eq. (4.36), one can recognise one delayed and one immediate pressure response term at the flame position. When changing the reference of the flame transfer function to the pressure at the inlet position, two delayed terms appear, one with a convective delay $\overline{\tau}$ and one with an acoustic delay $\frac{\overline{\tau}M_c}{1+M_c}$:

$$\begin{aligned}\mathrm{FTF}_{p'(x_i),mod}(\omega) = &\left[\frac{\overline{\rho}_c\overline{a}_c}{\overline{u}_c\overline{p}} + \frac{1}{\gamma} - \varphi_p(1+M_c)\right]\mathscr{F}_{\overline{\dot{\omega}}_c}(\omega)\exp\left(-i\omega\overline{\tau}\right)\\ &+ \varphi_p(1+M_c)\mathscr{F}_{\overline{\dot{\omega}}_c}\left(\frac{\omega M_c}{1+M_c}\right)\exp\left(\frac{-i\omega\overline{\tau}M_c}{1+M_c}\right).\end{aligned} \tag{4.38}$$

The second additive term represents the instantaneous response of the reaction rate to the perturbation at the flame; in Eq. (4.38) it is now characterised by an acoustic delay time $\frac{\overline{\tau}M_c}{1+M_c}$. The first term, on the other hand, describes the impact of fuel mass flow perturbations and the history effect of the pressure sensitivity, which acts with a convective delay time $\overline{\tau}$. This can be nicely illustrated by evaluating the flame response to unit impulse excitations at the inlet position, which can be obtained from time domain simulations and is shown in Fig. 4.10 for different mixtures. As expected, the response is characterised by two peaks: a very distinct peak with high values at the acoustic delay time $\frac{\overline{\tau}M_c}{1+M_c}$ and a broader peak with lower absolute values at the convective delay time $\overline{\tau}$. The sharpness of the peaks is inversely proportional to the

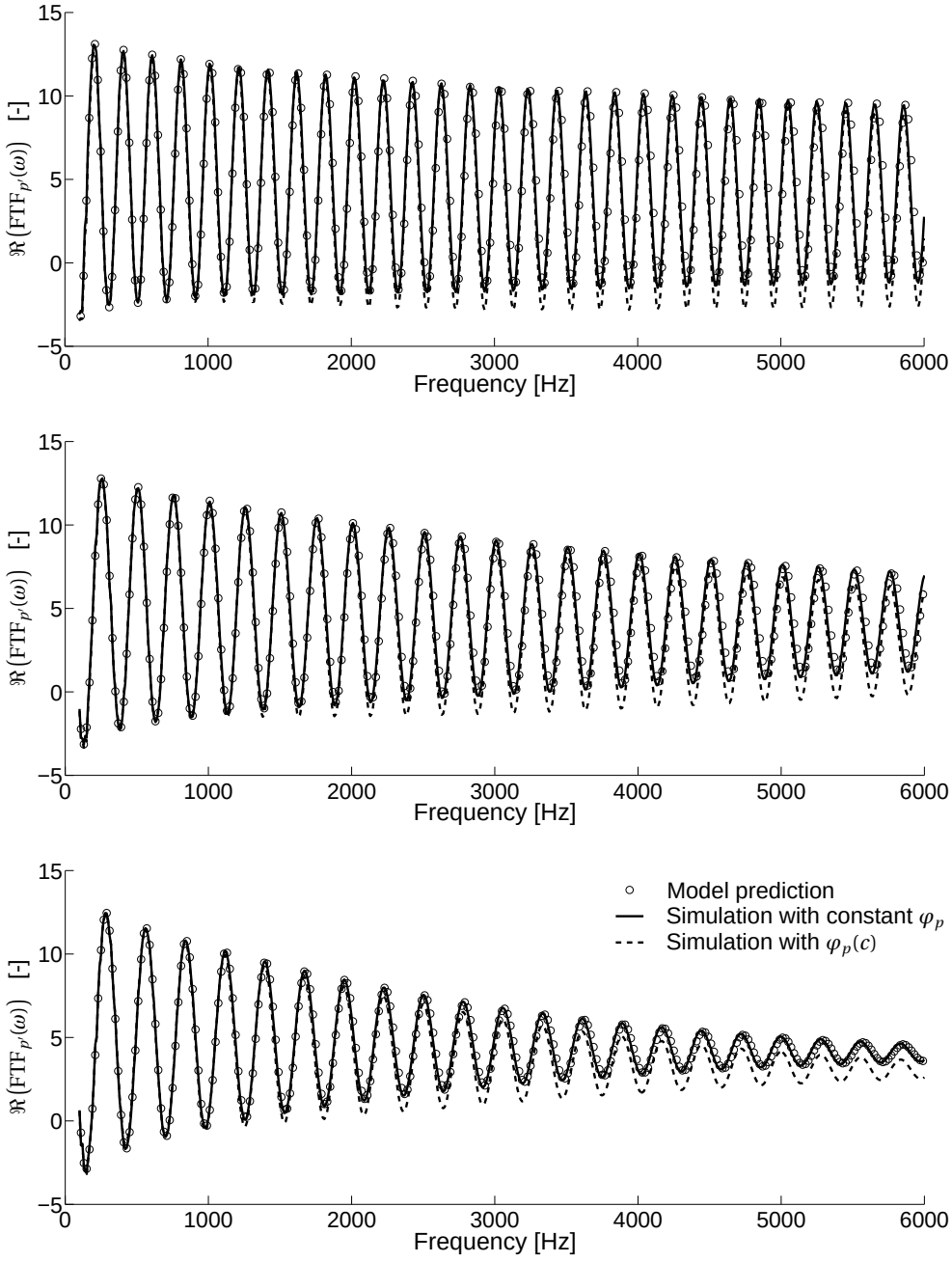

Figure 4.9: Comparison between model predictions and simulation results for FTF real part regarding f-waves (from top to bottom: $\lambda = 2$, $\lambda = 3$, $\lambda = 4$)

degree of dispersion that a response component is subjected to. This explains why at high frequencies, when dispersion becomes increasingly relevant, the convectively transported terms are more strongly attenuated and the flame response converges toward the instantaneous response component characterised by constant, high positive values.

Looking at Fig. 4.10, one can recognise that both peaks become wider for leaner mixtures. This results from the fact that the heat release occurs more slowly at leaner conditions; indeed, progress variable source term curves as the one shown in Fig. 3.1 tend to have a broader peak at lean conditions. Hence, both signal components will be subjected to a stronger dispersion. Nevertheless, the first peak still remains very sharp; the corresponding response term hence remains relatively unaffected by dispersion in the frequency range of interest. However, the dispersion of the term with convective delay is further enhanced for lean mixtures. As a consequence, the frequency response approaches constant, high positive values already at lower frequencies.

At the same time, ignition occurs earlier, as can also be seen in the unit impulse response (UIR) signals in Fig. 4.10. This affects the interference between the two response components, since the time shift in between them is proportional to the ignition delay, see Eq. (4.38). This explains why slower variations of the frequency response are observed for leaner mixtures in Fig. 4.9. The frequency gap between two neighboring response peaks can for instance be estimated to lie around $\frac{1}{(1-M_c)\overline{\tau}}$.

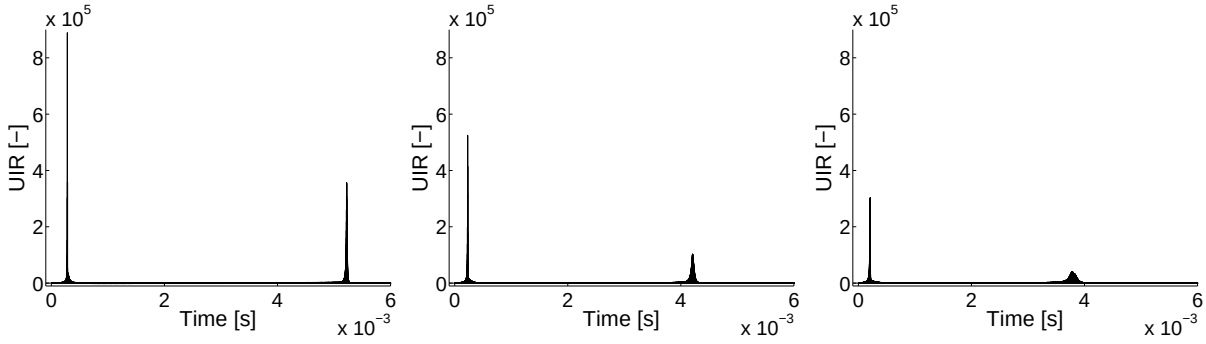

Figure 4.10: Comparison between unit impulse responses to f-wave excitation at the inlet position (from left to right: $\lambda = 2$, $\lambda = 3$, $\lambda = 4$)

In general, one can conclude that, especially at higher frequencies and lean conditions, auto-ignition flames can cause a positive thermoacoustic coupling throughout wide frequency ranges ($\Re(\mathrm{FTF}_{p'(\overline{x}_f)}) > 0$). This represents a concern for technical systems, in which ignition kernels do preferably appear in lean regions. It can thus be supposed that the flame transfer function of a technically premixed auto-ignition flame is more likely to resemble those of lean perfectly premixed flames, as will be discussed later.

4.4 Consequences for system stability and further model extensions

4.4.1 Impact on longitudinal mode stability

The analysis of the resulting flame transfer function suggested that auto-ignition flames might become unstable at elevated frequencies. In order to investigate this in more detail, the expressions of Eq. (4.31) are used in an acoustic network model. Such tools are commonly employed for the prediction of thermoacoustic stability, see section 3.3 and [20, 22, 56, 106].

In the present case, a one-dimensional network model based on the equations given in section 3.3 is used, yielding the frequency and the growth rate of the longitudinal eigenmodes in a straight tube with a total length of one

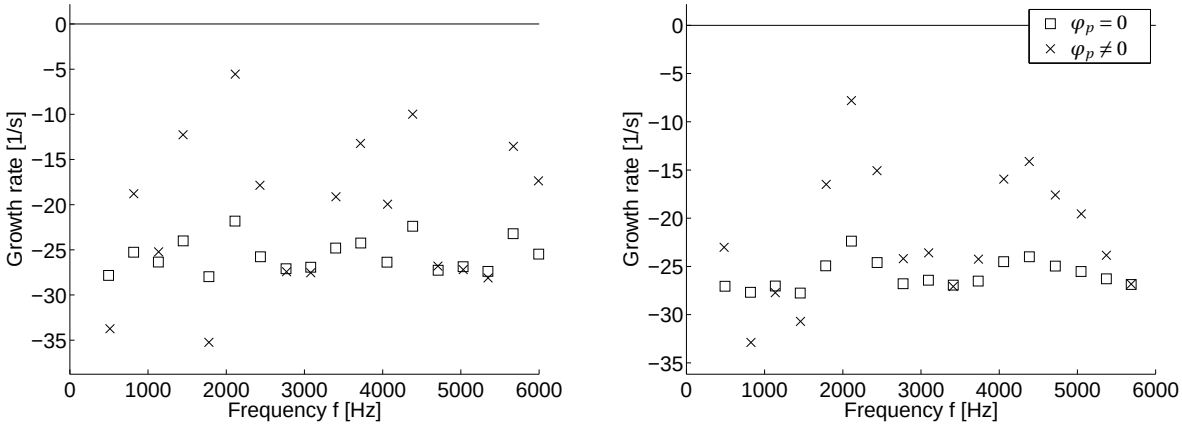

Figure 4.11: Impact of pressure sensitivity on longitudinal mode stability for exemplary flame setup (left: $\lambda = 3$, right: $\lambda = 4$)

meter. The results are shown in Fig. 4.11 for two different compositions, with the same mean flow Mach number $M_c = 0.058$ as for the calculation of the flame transfer functions in section 4.3.4. In one case, real and imaginary part of the eigenmodes are determined using a constant pressure sensitivity φ_p computed from reactor calculations, in the other using a pressure sensitivity value of zero. The comparison between the two calculations allows to assess the impact of pressure waves on chemical kinetics and thermoacoustic stability. When no pressure sensitivity is considered, heat release modulations only appear through the modulation of entering mixture mass flow, which is calculated according to Eq. (4.19).

One can clearly observe that the inclusion of pressure sensitivity has a strong influence on the stability prediction. Indeed, the growth rates obtained generally increase when including the pressure sensitivity. The real part of the eigenfrequencies, i.e. the wavelength of the acoustic mode, shows only small variations, since it is mostly determined by the geometry of the burner.

The observed behaviour is very much in line with the previous analysis of the flame transfer function. Especially for lean mixtures, the pressure sensitivity terms generally shift the modes toward the unstable region. This appears clearly in the mode stability plot for $\lambda = 4$, where the pressure sensitivity significantly reduces the stability margin in nearly the entire frequency range. For richer mixtures, the behaviour is similar, however a stronger damping effect of the pressure sensitivity can occur at lower frequencies. Eventually, the onset of instability always depends on the acoustic losses in the system, which are, in the present setup, determined by the reflection coefficients at the boundaries. These were set to arbitrary values of 0.8 and -0.8 for inlet and outlet, respectively. The presence of a mean temperature jump at the flame represents a further sink of acoustic energy.

The eigenmode calculations with the newly derived model for the pressure sensitivity show that the impact of pressure waves on chemistry cannot be neglected for auto-ignition flames with high oxidiser temperatures. This feedback mechanism hence promotes thermoacoustic pulsations, as it most often reduces the stability margin, especially at elevated frequencies and lean conditions.

This needs to be taken into account during the design stage of gas turbine combustors with high oxidiser temperatures. However, in industrial practice,

the complexity of the problem goes beyond the example of linear stability analysis of purely longitudinal modes shown here. During the design process, it is of high interest to obtain reliable predictions for limit cycle amplitudes in a non-linear context. Moreover, since the driving effect appears mostly at elevated frequencies, one has to consider complex-shaped modes with transverse components.

The next subsections will suggest how the model can be extended in a straightforward manner to capture non-linear effects, technical premixing, and transverse mode shapes. Additionally, the impact of pressure sensitivity is investigated using transient LES calculations in chapters 5 and 6. An easy-to-use extension of common combustion models based on tabulated chemistry is proposed in section 4.4.6, in order to capture the pressure impact at low computational cost.

4.4.2 Extension to non-linear flame description

Non-linearities in thermoacoustic theory have received growing attention in past years, as they deliver very important results, in particular for the prediction of limit-cycle amplitudes and bifurcation diagrams, see e.g. the works of Noiray et al. [81], Dowling [23], or Moeck et al. [76]. The concept of flame describing function (FDF), i.e. a flame transfer function depending on excitation amplitude, proved to be very useful, namely for the experimental assessment of non-linear flame behaviour and the subsequent use in prediction tools such as network models [81].

In an analytical framework as used here, an FDF can be obtained when considering higher order terms. For verification purposes, plug flow time-domain simulations are used as previously, but with varying excitation amplitudes.

In the derivation of the linear flame transfer function, higher order terms have been neglected at two calculation steps: Firstly, in the transition from Eq. (4.5) to Eq. (4.6), when the interaction between the modulations of mixture flow rate and disturbances of the chemical source term is neglected. Secondly, in the transition of Eq. (4.15) to Eq. (4.16), when the modulation of the chemical source term is calculated. At this point, higher order terms come into play by two different mechanisms, namely by the interference between the modu-

lations of heat release intensity and shifts in delay (see section 4.2.3), and by the extension of the Taylor series used for the impact of the delay shifts. The latter effect is of high relevance, since the chemical source term curves show very high gradient values. Hence, for this type of flames, non-linearities are expected to appear already at rather low excitation amplitudes, as presented in [128].

The non-linearity can be expressed as follows in an expanded expression for heat release modulations:

$$\left.\frac{\dot{Q}'(t)}{\overline{\dot{Q}}}\right|_{nl} \approx \int_{-\infty}^{t} \left[\frac{\dot{m}'_F(t_i)}{\overline{\dot{m}}_F} \overline{\dot{\omega}}_c(t-t_i) + \dot{\omega}'_c(t-t_i) + \frac{\dot{m}'_F(t_i)}{\overline{\dot{m}}_F} \dot{\omega}'_c(t-t_i) \right] dt_i, \tag{4.39}$$

with

$$\begin{aligned}
\dot{\omega}'_c(t-t_i) \approx\ & \overline{\dot{\omega}}_c(t-t_i)\,\varphi_p \frac{p'(x_i+(t-t_i)\overline{u}_c,t)}{\overline{p}} \\
& + \int_{t_i}^{t} \varphi_p \frac{p'(x_i+(t^+-t_i)\overline{u}_c,t^+)}{\overline{p}} dt^+ \frac{d\overline{\dot{\omega}}_c(t-t_i)}{dt} \\
& \quad \cdot \left[1+\varphi_p \frac{p'(x_i+(t-t_i)\overline{u}_c,t)}{\overline{p}} \right] \\
& + \frac{1}{2!} \left[\int_{t_i}^{t} \varphi_p \frac{p'(x_i+(t^+-t_i)\overline{u}_c,t^+)}{\overline{p}} dt^+ \right]^2 \frac{d^2\overline{\dot{\omega}}_c(t-t_i)}{dt^2} \\
& \quad \cdot \left[1+\varphi_p \frac{p'(x_i+(t-t_i)\overline{u}_c,t)}{\overline{p}} \right] \\
& + \frac{1}{3!} \left[\int_{t_i}^{t} \varphi_p \frac{p'(x_i+(t^+-t_i)\overline{u}_c,t^+)}{\overline{p}} dt^+ \right]^3 \frac{d^3\overline{\dot{\omega}}_c(t-t_i)}{dt^3}.
\end{aligned} \tag{4.40}$$

All contributions up to the third order are taken into account for the heat release modulations. The equation can be simplified easily in a manner analogous to the linear expression, making use of the calculus rules for the Fourier transform. However, in a non-linear framework, it is very important to distinguish between real and complex-valued fluctuations. Indeed all physical fluctuation values have to be written properly including their negative frequency content:

$$p'(x,t) = \frac{\overline{\rho}_c \overline{a}_c}{2} \left[f(x,t) + f^*(x,t) + g(x,t) + g^*(x,t) \right], \tag{4.41}$$

$$u'(x,t) = \frac{1}{2} \left[f(x,t) + f^*(x,t) - g(x,t) - g^*(x,t) \right], \tag{4.42}$$

with

$$f^*(x,t) = \hat{f}\exp\left(-i\omega t + \frac{i\omega x}{(1+M_c)\overline{a}_c}\right), \tag{4.43}$$

$$g^*(x,t) = \hat{g}\exp\left(-i\omega t - \frac{i\omega x}{(1-M_c)\overline{a}_c}\right). \tag{4.44}$$

The inclusion of the complex conjugate characteristic wave terms f^* and g^* becomes relevant when multiplying fluctuation terms with each other. For instance a non-linear response contribution from the higher order terms can be obtained at the fundamental frequency. This can for example happen for the one before last term in Eq. (4.40), when a 2ω term is multiplied with a $-\omega$ term. As a consequence, one obtains an expression for the flame describing function $\mathrm{FDF}_{p',mod}(\omega,\hat{p})$, composed of the flame transfer function plus additional higher order terms. Since this expression is very long and difficult to interpret, it shall not be included in this thesis. It is judged more important to explicitly write down Eq. (4.40), as it clearly shows how the non-linearity can be incorporated into the model framework.

Similarly to the linear case, a verification is performed by comparison to a Fourier analysis of the Lagrangian reactor simulations. For this purpose the flame describing function is now compared for varying excitation amplitudes. Again, only right-running characteristic waves are considered for simplicity reasons. The results are presented in Fig. 4.12. The prediction of the model (with terms up to third order) is in very good agreement with the time-domain simulations up to pressure amplitudes of approx. 10%. The derived analytical model therefore allows an accurate prediction of both linear and non-linear dynamics of auto-ignition flames. For higher amplitudes the FDF needs to be expanded to even higher order terms.

Figure 4.12 only shows a small reduced frequency window for better clarity. Nevertheless the impact of the higher order terms is similar over a wide frequency range up to 10 kHz. It can be noted that the shown FDF evolution indicates the possibility of so-called triggered instabilities, see [81]. Close to the minima depicted in Fig. 4.12, the FDF real part, and consequently the Rayleigh criterion, change sign at higher amplitudes. Hence, it is conceivable that a sufficiently strong initial perturbation triggers an instability at a linearly stable frequency.

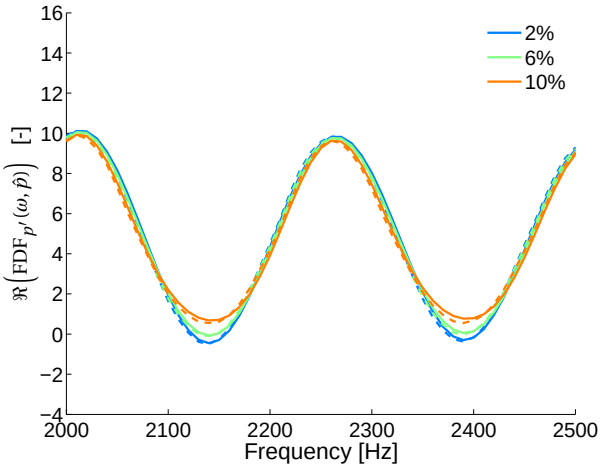

Figure 4.12: Verification of FDF real part evolution for varying amplitude levels - Comparison between time domain simulations (dashed lines) and model prediction (continuous lines)

In general, although deviations from the linear response start to appear at rather low fluctuation amplitudes of a few percent, the non-linearity is rather weak, since the flame response remains strong. The establishment of a limit cycle regime is thus not likely to be due to the saturation of the heat release rate at the fundamental frequency as it is shown in Fig. 4.12.

However, additional attenuation could be caused by non-linear mode coupling, when several acoustic modes are excited in the setup, see e.g. [112]. The non-linear extension of the presented model also allows to properly describe such effects, but this goes beyond the scope of the present paper. Moreover, as mentioned before, the assumption of quasi-stationary behaviour might not hold true anymore at very high amplitudes and frequencies; this could induce a non-linear flame response and needs to be investigated more in detail if one wants to provide limit-cycle predictions.

4.4.3 Applicability for technical premix cases

The presented model relies on a very strong assumption regarding the fuel premixing, which is supposed to be perfect. Hence, no dispersion effects linked to inhomogeneous mixing are included in the model. Such effects are commonly modelled by multiplying delayed terms in flame transfer functions by a dispersive factor, as proposed by Sattelmayer et al. [99]. This dispersive factor generally assumes a normal distribution of the time delay, see Polifke

et al. [92], and leads to an exponential attenuation of the flame response at higher frequencies. For the auto-ignition flames considered in the present work, the inclusion of dispersion effects needs to be consistent with the developed model framework. Therefore the physical effects caused by mixture inhomogeneities will first be discussed, before suggesting a suitable mathematical description.

The fuel addition in auto-igniting setups is mostly achieved either by co-flow (see [11, 69]) or cross-flow injection (as in Alstom's SEV configuration). During the induction period, strong mixing between fuel oxidiser streams is thus running in parallel with the radical build-up. As a result, heat release does not occur at a determined ignition location as for the perfect premix case but at varying positions (random-spots regime).

The ignition kernel formation is mostly governed by turbulent fluctuations in the burner, which are generally random noise characterised by a broadband frequency spectrum. For a thermoacoustic instability to develop, there must however be a coherent response of the flame to an acoustic perturbation. Acoustic velocity fluctuations could for instance modulate the fuel injection process and cause such a coherent response, by inducing periodic fluctuations of the mixture fraction. This feedback mechanism will be discussed in chapter 6. The present section shall instead indicate how the modelling of the feedback linked to pressure sensitivity needs to be adapted when inhomogeneous mixing conditions appear.

When dealing with inhomogenous mixing conditions, one first needs to make sure that the progress variable used can correctly describe the radical build-up until ignition even in the presence of mixing. This is indeed the case for the composite progress variable used in the present work, which was employed with success by Kulkarni and Polifke [58] for describing the auto-ignition of a fuel jet in hot oxidiser co-flow.

Regarding the pressure impact on auto-ignition kinetics, it was observed in section 4.2.2 that the pressure sensitivity factor φ_p varies only moderately over a wide range of air-excess ratios. Indeed it was approximated as constant in the analysis presented. In the case of a stratified mixture, the chemical kinetics in the different mixture layers will thus be affected in similar manner by acoustic perturbations, since the pressure sensitivity is the guiding parameter in the flame transfer functions derived before. As an approximation, the

response of a technical premix flame can thus be described by the same formalism, as the sum of one instantaneous and one delayed term, depending on the constant pressure sensitivity factor.

Nevertheless, in a technical premix setup, heat release will be more distributed and at a different position than for the perfect premix case. If a Gaussian shape is assumed for the source term evolution, the distribution parameters τ_{tech} and σ_{tech} need to be adapted with respect to the perfect premix case. Previous results indicated that the resulting time delay will be larger than the minimum τ_{MR} obtained for the most reactive mixture, depending e.g. on the turbulence conditions as shown by Kulkarni et al. [59], where the delay exceeded the reference value by max. 12 %. The spread corresponds here to the flame thickness, and needs to be determined from experiments or simulations.

Furthermore, the fuel mass flow will now depend on the acoustic pressure level at the injection point, as a function of the pressure drop δp through the injector hole [79]:

$$\frac{\dot{m}'_F(t_i)}{\overline{\dot{m}}_F} = -\frac{p'(x_i,t_i)}{2\delta p}, \tag{4.45}$$

This can be incorporated easily into the model framework, when a Gaussian shape is assumed for the heat release distribution, yielding a relation similar to the one of Eq. (4.33) for very low Mach numbers :

$$\left.\frac{\check{\dot{Q}}(t)}{\overline{\dot{Q}}}\right|_{tech} = -\left(\varphi_p + \frac{\overline{p}}{2\delta p}\right)\frac{\check{p}(x_i,t)}{\overline{p}}\exp\left(-i\omega\tau_{tech} - \frac{\omega^2\sigma_{tech}^2}{2}\right) + \varphi_p\frac{\check{p}(\overline{x}_f,t)}{\overline{p}}. \tag{4.46}$$

In order to give an idea of the possible flame response for technical premix cases, the flame transfer function was calculated using this relation, with values of $\tau_{tech} = 1.05\tau_{MR}$ and $\sigma_{tech} = 0.1\tau_{MR}$. In terms of UIR signals, this can be interpreted as a translation and a thickening of the response peaks. The results are shown in Fig. 4.13, yielding a smoother evolution than for the perfect premix case (see Figs. 4.8 and 4.9) with a quicker approach to a constant, positive value. Similar implications regarding system stability can thus be followed for technical premix cases, the tendency toward a generally high positive coupling at elevated frequencies is even enhanced.

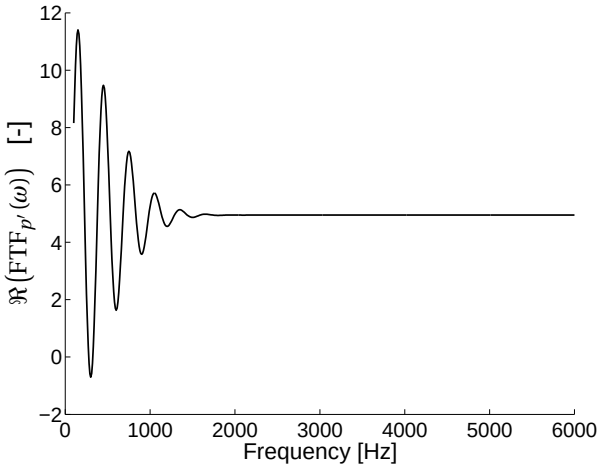

Figure 4.13: Evolution of modelled FTF real part for technical premix case

4.4.4 Limitations of plug flow reactor modelling

The plug flow reactor ansatz postulates that diffusive exchanges between the convected homogeneous reactors are negligible. The validity of this assumption depends on convective speeds as well as on diffusion coefficients. In turbulent flows the latter are comparatively high and might therefore influence the flame response. In a purely analytical framework, it is difficult to assess whether these are of influence or not. Nevertheless, their impact on the flame response can be discussed in a qualitative manner. This can be done by looking more closely at Eq. (4.18) given for longitudinal modes:

$$\frac{\dot{Q}'(t)}{\overline{\dot{Q}}} = \int_{-\infty}^{t} \left\{ \frac{\dot{m}'_F(t_i)}{\overline{\dot{m}}_F} \overline{\dot{\omega}}_c(t-t_i) + \overline{\dot{\omega}}_c(t-t_i)\,\varphi_p \frac{p'\left(x_i+(t-t_i)\overline{u}_c, t\right)}{\overline{p}} + \int_{t_i}^{t} \varphi_p \frac{p'\left(x_i+\overline{u}_c(t^+-t_i), t^+\right)}{\overline{p}} dt^+ \frac{d\overline{\dot{\omega}}_c(t-t_i)}{dt} \right\} dt_i.$$

The first and the last term on the RHS represent processes, which propagate at convective speed through the domain, namely fuel mass flow fluctuations and perturbations of the radical pool formed during the induction period. These perturbations will be attenuated due to axial diffusion between neighbouring plugs. The middle term, on the other hand, describes the instantaneous perturbation of the reaction rate by the pressure wave, which occurs immediately and is therefore not affected by slower, diffusive processes.

Axial diffusion will thus tend to attenuate gradients in axial direction that are linked to convective processes. In terms of UIR signals, axial diffusion

therefore only leads to an alternation and broadening of the second peak (see Fig. 4.10), whereas the instantaneous response component remains unchanged. The consideration of axial diffusion will thus tend to increase the dispersion of the convectively transported contributions to the flame response.

In terms of frequency response, its action on the convective response component can be represented by a low-pass filter behaviour. In the high frequency range, the flame response can thus generally be approximated by an asymptotical evolution toward the limiting case of a merely instantaneous response:

$$\left.\frac{\check{\dot{Q}}(t)}{\overline{\dot{Q}}}\right|_{HF} \approx \varphi_p \frac{\check{p}(\overline{x}_f, t)}{\overline{p}}. \tag{4.47}$$

This conclusion needs to be verified either by experiment or by simulation. The latter can be performed at reduced computational cost by making use of the pressure sensitivity parameter introduced in the present work, see section 4.4.6.

4.4.5 Extension to transverse acoustic modes

4.4.5.1 Transverse acoustic modes in a straight duct

Eventually, the model framework shall also be extended to transverse acoustic modes. This is of particular practical interest, since a constantly driving effect is predicted especially for high frequency modes, which often contain transverse components. The flame response to a purely transverse mode in a straight tube shall first be derived using the same analytical approach as before.

As for longitudinal modes, the heat release rate results from the history of the disturbances over the entire induction period and during heat release phase. However, two adaptations have to be made. The heat release zone is split in transversal direction as shown in Fig. 4.14. Hence, one plug flow reactor is considered for each streamline. Furthermore, the acoustic pressure is now constant in axial direction, but varies in transverse direction:

$$\check{p}(x, y, t) = \hat{p}(y) \exp(i\omega t). \tag{4.48}$$

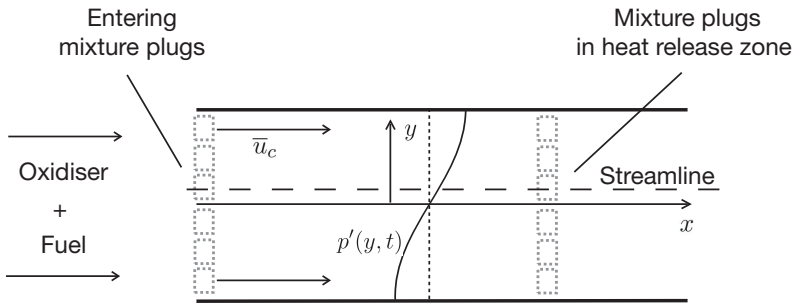

Figure 4.14: Sketch of the model setup used for the consideration of transverse modes

Using Eq. (4.48) in Eq. (4.18) yields the following expression for heat release modulations caused by transverse modes:

$$\frac{\int \check{\dot{\omega}}_h(x,y,t)dx}{\int \overline{\dot{\omega}}_h(x,y)dx} = \varphi_p \frac{\hat{p}(y)}{\overline{p}} \exp(i\omega t)\left[1 - \mathscr{F}_{\overline{\dot{\omega}}_c}(\omega)\exp\left(-i\omega\overline{\tau}\right)\right]. \tag{4.49}$$

with $\int \check{\dot{\omega}}_h(x,y,t)dx$ denoting the complex-valued fluctuations of the mass specific heat release rate integrated over the streamline, which is used here instead of the global heat release in order to account for the non-compactness of the flame with respect to the transverse acoustic mode.

The flame transfer function with respect to the local pressure thus reads as:

$$\mathrm{FTF}_{p',trans} = \varphi_p\left[1 - \mathscr{F}_{\overline{\dot{\omega}}_c}(\omega)\exp\left(-i\omega\overline{\tau}\right)\right]. \tag{4.50}$$

As for axial modes, the response consists of the sum of an instantaneous and a delayed response to the disturbance at the flame. The expression obtained is very similar to the one shown in Eq. (4.33), which was derived for longitudinal modes under the assumptions of normal source term evolutions and very low Mach numbers. However, these assumptions are not used for the transverse case. No dispersion term dampens the first term on the RHS of Eq. (4.49), the tendency toward high-frequency instabilities is hence further increased when transverse mode shapes come into play. Consequently, in Fig. 4.15, the response converges to a constantly high amplitude level at elevated frequencies.

The flame response to a unit pressure impulse is again determined from time domain simulations and yields the curves shown in Fig. 4.16. The instantaneous response occurs without delay, since the pressure is constant along the axis, whereas the convective response occurs at $t = \overline{\tau}$ as before. Since no fuel mass flow fluctuations occur, the second peak is now negative and relatively small.

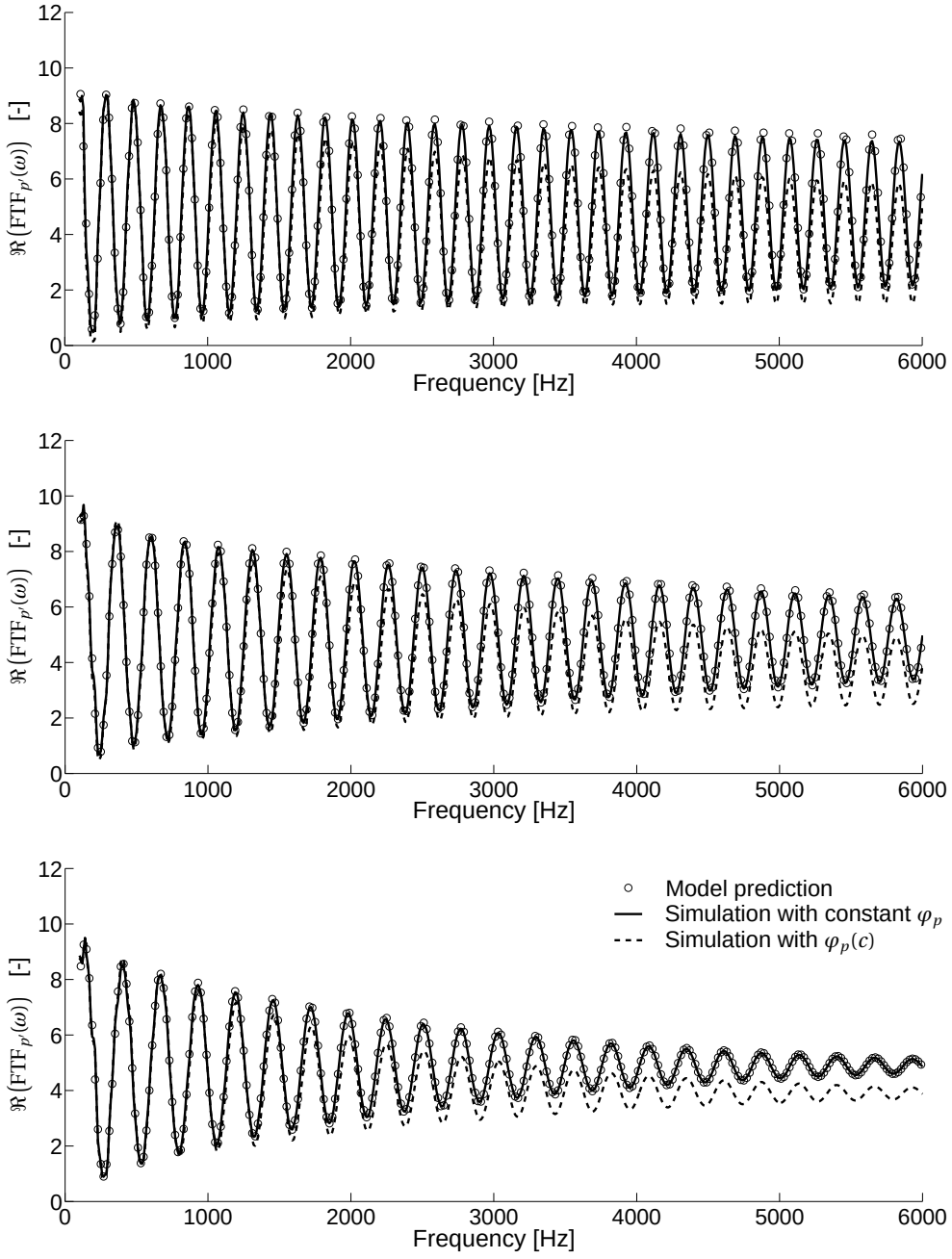

Figure 4.15: Comparison between model predictions and simulation results for FTF real part for transverse pressure excitation (from top to bottom: $\lambda = 2$, $\lambda = 3$, $\lambda = 4$)

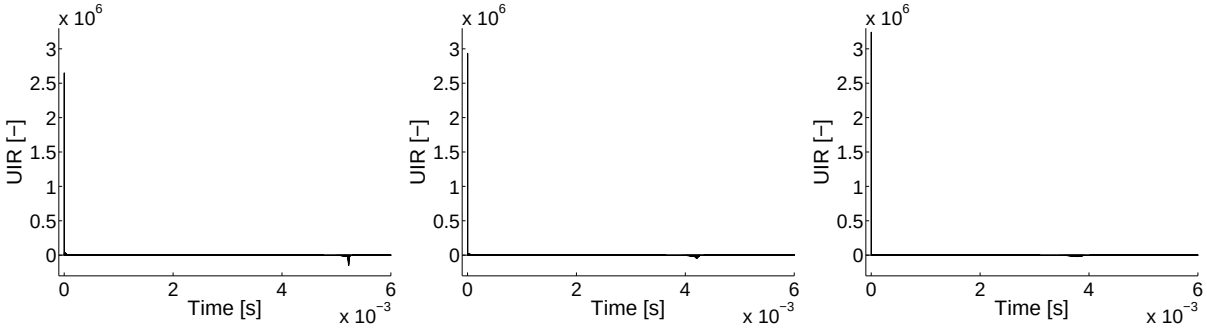

Figure 4.16: Comparison between unit impulse responses (UIRs) to transverse pressure excitation (from left to right: $\lambda = 2$, $\lambda = 3$, $\lambda = 4$)

4.4.5.2 Transverse acoustic modes in a backward-facing step configuration

For a better representation of technical applications, one should as well consider the backward facing step at the entrance into the combustion chamber. Area expansions do modify both longitudinal and transverse acoustic modes. However, the effect of an area expansion will only be included for transverse modes, since these are of main interest for this work. The corresponding model setup is shown in Fig. 4.17. Pure transverse modes in the combustion

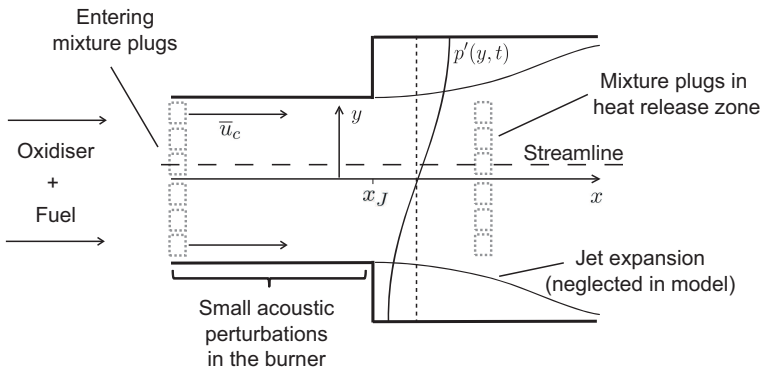

Figure 4.17: Sketch of the backward facing step setup used for the consideration of transverse modes

chamber are considered, which are strongly damped in the burner due to the smaller cross-section and the resulting difference in cut-on frequency. Hence, pressure fluctuations related to these mode will be small upstream of the area expansion and can thus be described by the following relation:

$$\check{p}(x,y,t) = \begin{cases} 0, & x < x_J \\ \hat{p}(y)\exp(i\omega t), & x \geq x_J \end{cases} \tag{4.51}$$

with x_J denoting the axial position of the backward-facing step.

Introducing the Heaviside step function $\mathscr{H}$, one can write for the heat release fluctuations on a streamline, neglecting the jet expansion in the combustion chamber:

$$\left.\frac{\int \check{\dot{\omega}}_h(x,y,t)dx}{\int \overline{\dot{\omega}}_h(x,y)dx}\right|_J = \int_{-\infty}^{t} \varphi_p \frac{\hat{p}(y)}{\overline{p}} \exp(i\omega t)\overline{\dot{\omega}}_c(t-t_i)\mathscr{H}\left(t-t_i-\frac{x_J}{\overline{u}_c}\right)dt_i + \int_{-\infty}^{t}\int_{t_i}^{t} \varphi_p \frac{\hat{p}(y)}{\overline{p}} \exp(i\omega t^+)\mathscr{H}\left(t^+-t_i-\frac{x_J}{\overline{u}_c}\right)dt^+ \frac{d\overline{\dot{\omega}}_c(t-t_i)}{dt}dt_i. \tag{4.52}$$

Therein, the step function indicates that the convected homogeneous reactors are only perturbed by the acoustics after a convection time of $x_J/\overline{u}_c$. This relation can again be solved analytically:

$$\left.\frac{\int \check{\dot{\omega}}_h(x,y,t)dx}{\int \overline{\dot{\omega}}_h(x,y)dx}\right|_J = \varphi_p \frac{\hat{p}(y)}{\overline{p}} \exp(i\omega t)\left[1-\int_0^{x_J/\overline{u}_c} \overline{\dot{\omega}}_c(t^+)dt^+\right] - \varphi_p \frac{\hat{p}(y)}{\overline{p}} \exp(i\omega t)\mathscr{F}_{\overline{\dot{\omega}}_c,J}(\omega)\exp\left(-i\omega\left(\overline{\tau}-\frac{x_J}{\overline{u}_c}\right)\right) \tag{4.53}$$

using the Fourier transform $\mathscr{F}_{\overline{\dot{\omega}}_c,J}$ of a clipped reference source term evolution $\overline{\dot{\omega}}_{c,J}$:

$$\mathscr{F}_{\overline{\dot{\omega}}_c,J}(\omega) = \int_{-\infty}^{+\infty} \exp(-i\omega t^+)\overline{\dot{\omega}}_{c,J}(t^+ + \overline{\tau})dt^+ \tag{4.54}$$

with

$$\overline{\dot{\omega}}_{c,J}(t^+ + \overline{\tau}) = \begin{cases} 0, & t^+ + \overline{\tau} < \frac{x_J}{\overline{u}_c} \\ \overline{\dot{\omega}}_c(t^+ - \overline{\tau}), & t^+ + \overline{\tau} \geq \frac{x_J}{\overline{u}_c} \end{cases} \tag{4.55}$$

The resulting flame transfer functions with respect to pressure are shown in Fig. 4.18 for three different positions of the area jump (increasing toward the bottom), together with results from the time-domain plug flow calculations. The analytical approach performs very well again. The inclusion of the area jump generally leads to a reduction of the characteristic time lag of the setup, which is now equal to $\overline{\tau} - \frac{x_J}{\overline{u}_c}$. The response generally shows less oscillations than for the straight tube, but convergences as well toward a high positive value for larger frequencies, as long as the area jump is located before the heat release zone. For the last plot shown in Fig. 4.18, this is not the case anymore and the frequency response is generally damped. This effect can be attributed

to a large extent to the first term on the RHS of Eq. (4.53), which converges toward zero for increasing x_J. Physically, this means that only the late part of the combustion process is modulated by the acoustic perturbations.

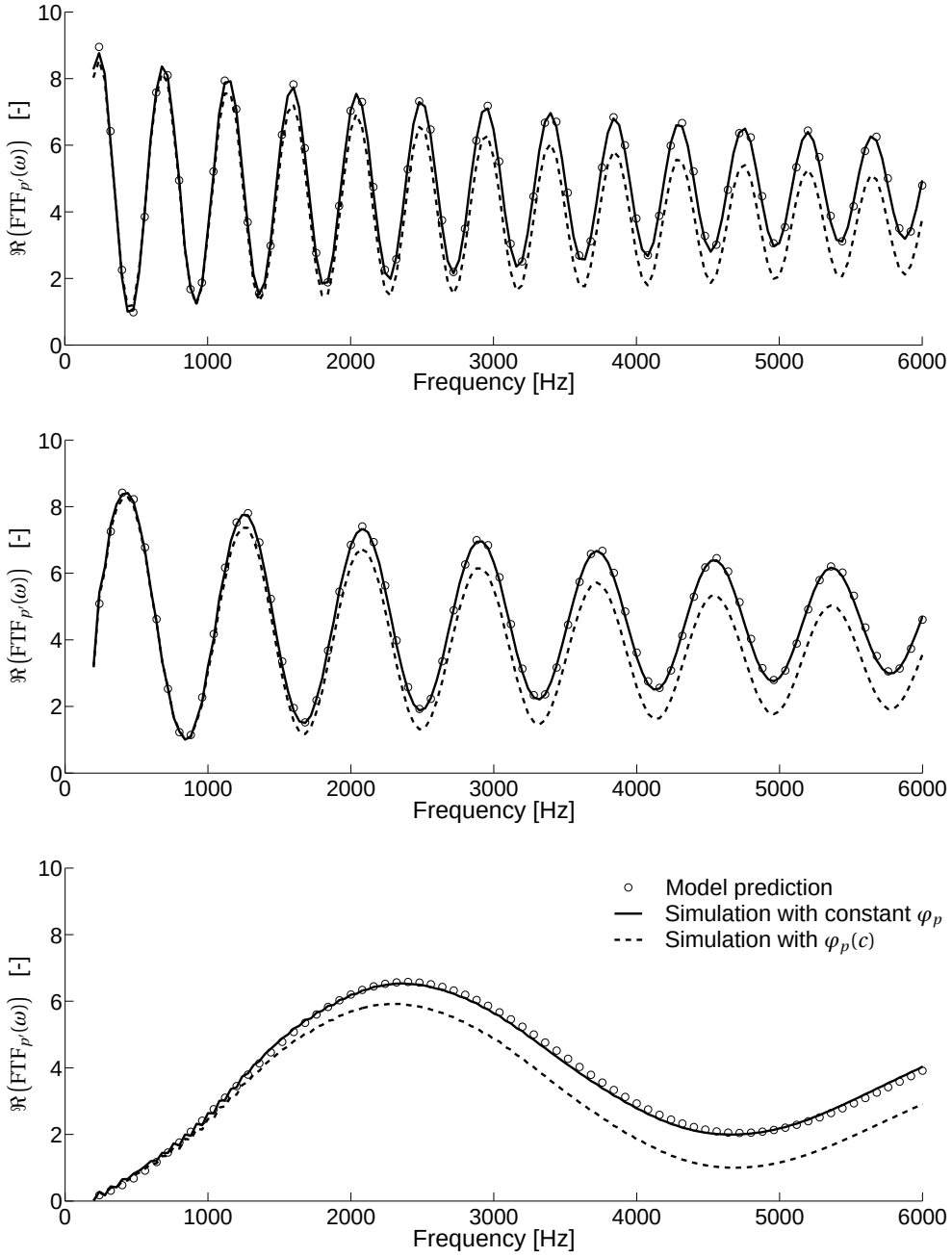

Figure 4.18: Verification of FTF real part evolution for transverse mode in backward facing step configuration - Comparison between time domain simulations and model prediction for different positions of the area jump (from top to bottom: x_j=8 cm, x_j=12 cm, x_j=16 cm)

Taking further into account inhomogeneous mixing conditions and axial diffusion as done for longitudinal methods, the same asymptotic limiting case can be found as for longitudinal modes, provided the area jump is located sufficiently far away from the heat release zone:

$$\left.\frac{\int \check{\dot{\omega}}_h(x,y,t)dx}{\int \overline{\dot{\omega}}_h(x,y)dx}\right|_{trans,HF} \approx \varphi_p \frac{\hat{p}(y)}{\overline{p}} \exp(i\omega t). \tag{4.56}$$

4.4.5.3 Local heat release rate fluctuations due to transverse excitation

One can also derive a fully non-compact description under the form of local, mass-specific heat release rate fluctuations $\check{\dot{\omega}}_h(x,y,t)$. This is shown here for purely transverse modes, and the resulting general expression is independent of the area jump position.

Therefore, the heat released at position x, y and time t corresponds to a plug flow reactor injected at time $t-(x-x_i)/\overline{u}_c$ subjected to pressure fluctuations of amplitude $\hat{p}(y)$. Using the formalism introduced, the mass-specific heat release rate fluctuations for this reactor and hence the local fluctuations can be written as:

$$\begin{aligned}
\frac{\check{\dot{\omega}}_h(x,y,t)}{\overline{\dot{\omega}}_h(x,y)} &= \varphi_p \frac{\hat{p}(y)}{\overline{p}} \exp(i\omega t) + \int_{t-(x-x_i)/\overline{u}_c}^{t} \varphi_p \frac{\hat{p}(y)}{\overline{p}} \exp(i\omega t^*) dt^* \\
&\quad \cdot \frac{1}{\overline{\dot{\omega}}_c\left(t-(x-x_i)/\overline{u}_c\right)} \frac{d\overline{\dot{\omega}}_c\left(t-(x-x_i)/\overline{u}_c\right)}{dt} \\
&= \varphi_p \frac{\hat{p}(y)}{\overline{p}} \exp(i\omega t) + \frac{\varphi_p}{i\omega} \frac{\hat{p}(y)}{\overline{p}} \left[\exp(i\omega t) - \exp(i\omega(t-(x-x_i)/\overline{u}_c))\right] \\
&\quad \cdot \frac{1}{\overline{\dot{\omega}}_c\left(t-(x-x_i)/\overline{u}_c\right)} \frac{d\overline{\dot{\omega}}_c\left(t-(x-x_i)/\overline{u}_c\right)}{dt}
\end{aligned} \tag{4.57}$$

The second additive term represents the time-delaying effect of the pressure sensitivity and converges toward zero for elevated frequencies. As a first approximation, one can thus write:

$$\left.\frac{\check{\dot{\omega}}_h(x,y,t)}{\overline{\dot{\omega}}_h(x,y)}\right|_{trans,HF} \approx \varphi_p \frac{\hat{p}(y)}{\overline{p}} \exp(i\omega t) \tag{4.58}$$

In the high frequency range, it is therefore likely that the flame shows an instantaneous response to the local pressure perturbation. As will be shown in chapter 7, this conclusion allows a straightforward formulation of a local flame transfer function. Nevertheless, it shall be borne in mind that the neglected term can be significant i.e. at the end of the ignition processes, when variations of the reaction source term $\frac{d\overline{\dot{\omega}}_c}{dt}$ are greatest.

4.4.6 Use of pressure sensitivity in CFD combustion modelling

The CFD simulation of practical flame configurations involving auto-ignition is very challenging in terms of combustion modelling. In particular for technical applications it is not possible to calculate the entire set of chemical species contained in the reaction mechanism. Hence, in order to reduce the computational effort, chemistry tabulation is often employed. Though, reactor simulations are performed beforehand and chemical reaction rates are stored in tables, e.g. as functions of mixture fraction Z and reaction progress c, as presented in section 3.2.2.

In general, the tabulation data is generated at reference pressure p_{Ref}; the pressure impact on the chemistry is thus not retained. A straightforward possibility to include it would be to add the pressure level as a further table dimension. However, this leads to large table sizes and asks for advanced interpolation routines in order to ensure low computation times. The study conducted on the pressure sensitivity in section 4.2 leads the way to a very efficient, approximate inclusion of the pressure impact. It was shown that the pressure sensitivity parameter φ_p only shows little variations over wide ranges of mixture fraction and reaction progress. Hence it is proposed to add a straightforward extension of the combustion model by including φ_p, which is formulated similarly to Eq. (4.10):

$$\dot{\omega}_c\left(Z,c,p\right) = \dot{\omega}_c\left(Z,c,p_{Ref}\right)\left(1+\varphi_p\frac{p-\overline{p}}{\overline{p}}\right), \tag{4.59}$$

where $\overline{\dot{\omega}}_c\left(Z,c,p_{Ref}\right)$ denotes the tabulated source term value at reference pressure, and $\overline{p}$ the time-averaged pressure in the computational cell. In the presence of acoustic waves, the pressure variations from the average can be approximated as isentropic state changes, leading to source term variations as described by the pressure sensitivity.

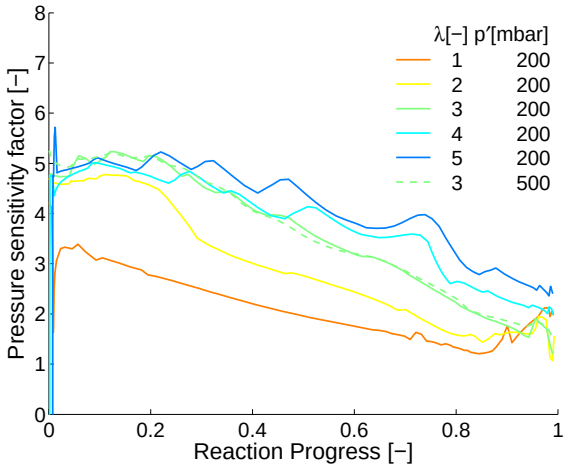

Figure 4.19: Evolutions of pressure sensitivity in premixed flames of varying air-excess ratio and pressure disturbance amplitudes, plotted against progress variable

The implementation of this extension is easy and does not lead to any significant increase in computational effort. It is of particular interest for complex configurations where analytical approaches reach their limit. The CFD simulations made in this work show that in configurations with a backward-facing step flame propagation is also important, namely in the shear layer region behind the burner exit. In chapter 3 it was shown that a tabulated chemistry ansatz based on homogeneous reactors can also be applied for the description of flame propagation, as the chemical reaction rates are similar in the reactor and in premixed flame. Before using the extension for the pressure sensitivity, one has to make sure that it affects a premix flame in the same way. Values of pressure sensitivity have thus been calculated by comparing premix flame calculations at various pressure levels. The results are shown in Fig. 4.19 and clearly indicate that similar evolutions appear for the pressure sensitivity factor, with the exception of mixtures close to stoichiometry. This limitation however can be considered of low relevance, as lean conditions are prevalent in technical applications. The extension is therefore made for the entire simulated domain, without considering the local flame stabilisation mechanism.

4.5 Conclusions and outlook regarding pressure sensitivity

The present chapter introduced a mathematical model, which allows to accurately predict heat release modulations in flames stabilised by auto-ignition.

This was achieved mainly by a physical description based on a plug flow reactor analogy, which was supported by a chemical sensitivity analysis using detailed homogeneous reactor simulations.

As a result, flame transfer functions can be predicted for a simplified 1D perfect premix configuration with high accuracy over wide frequency ranges and very little computational cost. The analysis of the expressions obtained and their use in acoustic network model calculations led to the conclusion that the presented feedback mechanism is eager to yield a positive flame-acoustics coupling, in particular in the elevated frequency range. This is especially true for transverse modes, which can also be treated using the presented model framework. At high frequencies, the flame hence appears to respond instantaneously to local pressure perturbations.

Regarding future work, a thorough experimental validation of the feedback mechanism and of the description given above is needed. Moreover, it would be interesting to investigate the impact of preheat temperature on the pressure sensitivity. Indeed, the results generally indicate that for richer mixtures, which are at lower temperatures in the present case, the values of pressure sensitivity tend to decrease. From such a parameter variation, one could try to elucidate whether the pressure sensitivity should also be taken into account for other combustion processes. However, as temperatures decrease, flame stabilisation will most likely be ensured by flame propagation. While the kinetic studies shown in the present work were mostly based on reactor simulations, one would then rather use laminar flame calculations; some transient detailed chemistry calculations of premix flames subjected to an acoustic excitation could allow some detailed understanding of the flame response.

5 Large Eddy Simulation of Perfect Premix Combustor

This chapter presents simulation results obtained with the perfect premix case setup described in section 3.2.3.1. This setup is very suitable for a fundamental investigation of the flame dynamics in reheat combustors, as the rather simple flow field and the absence of mixture inhomogeneities promise a detailed insight into the flame feedback linked to flame wrinkling and displacement, as well as to density fluctuations and pressure sensitivity. The following chapter 6 will elucidate to what extent the observations made for the perfect premix case also hold true for the more complex configuration with technical premixing.

Before having a closer look at the fluctuations of the heat release rate linked to acoustic perturbations, the flame characteristics shall first be described for the case without acoustic excitation. This is of particular interest, since it was mentioned in chapter 2 that both auto-ignition and flame propagation will contribute to the flame stabilisation in such a setup.

Most of the analysis is performed in the central (x, y)-symmetry plane of the setup (see Fig. 3.3), where the largest acoustic fluctuations appear. In the present work, the focus lies on understanding how local heat release rate fluctuations appear due to transverse perturbations; this is exemplified for the symmetry plane shown. The findings are generally valid for any other flow position, but local amplitude levels will depend on the actual probe location. For illustration, a transverse plane was analysed in addition to the central symmetry plane, the results obtained are shown in section 5.5. It was not feasible for data management reasons to perform the analysis for the entire 3D domain. This would be necessary in order to characterise the global response of the flame.

Part of the results exhibited in this chapter have been published previously by the author in [123, 124, 127].

5.1 Flame stabilisation without acoustic excitation

Distributions of the instantaneous progress variable source term $\dot{\omega}^{(n)}_{Y_c,chem}$ in an arbitrary stochastic field are shown in Fig. 5.1 for three cases with inlet velocities ranging from 40 to 55 m/s. Two characteristic zones are observed in the reaction rate distributions. In the jet core, a nearly flat, vertical flame front stabilised by auto-ignition establishes. Its position agrees with the auto-ignition length computed as the product of ignition delay τ and inlet velocity u_{in}. This is a specificity of a perfectly premixed setup, where ignition is not retarded by mixing effects. As a consequence, the impact of turbulence is small compared to non-premixed setups, and the auto-ignition zone appears to be very flat. For the case with 55 m/s, the ignition delay, the fluid residence time, and the turbulent timescale were 4, 4.5, and 2 ms, respectively.

A second characteristic region appears in the shear layers, which separate the jet core from the burnt products recirculating in the corners of the geometry. The area jump provides an anchoring point for a flame stabilisation due to kinematic balance between flame propagation and flow. Since adiabatic wall conditions are imposed, the attachment point of the flame lies directly at the edge of the burner exit. Hence, both auto-ignition and flame propagation contribute to the flame stabilisation in the presented generic reheat combustor; this is properly captured by the combustion model.

A fundamental difference between the two zones can be noticed when looking at the dependence of the flame position on the local flow characteristics. This is shown in Fig. 5.2 where an instantaneous flame shape is overlaid on the instantaneous distributions of resolved vorticity magnitude. In the flame propagation regions, the flame closely follows the vorticity contours. This agrees with expectations, since flame propagation relies on the upstream diffusion of heat from the burnt products to the fresh mixture in order to launch the chemical reactions. The auto-ignition zone, however, does not show any distinct relation between flame position and local flow structures, as the initiation of heat release does not depend on diffusion processes, but only on the residence time of the mixture.

These observations are very relevant with respect to the dynamic response of the flame to acoustic excitation. As shown by different authors [84, 110], transverse excitation in gas turbine combustors can strongly influence the flow

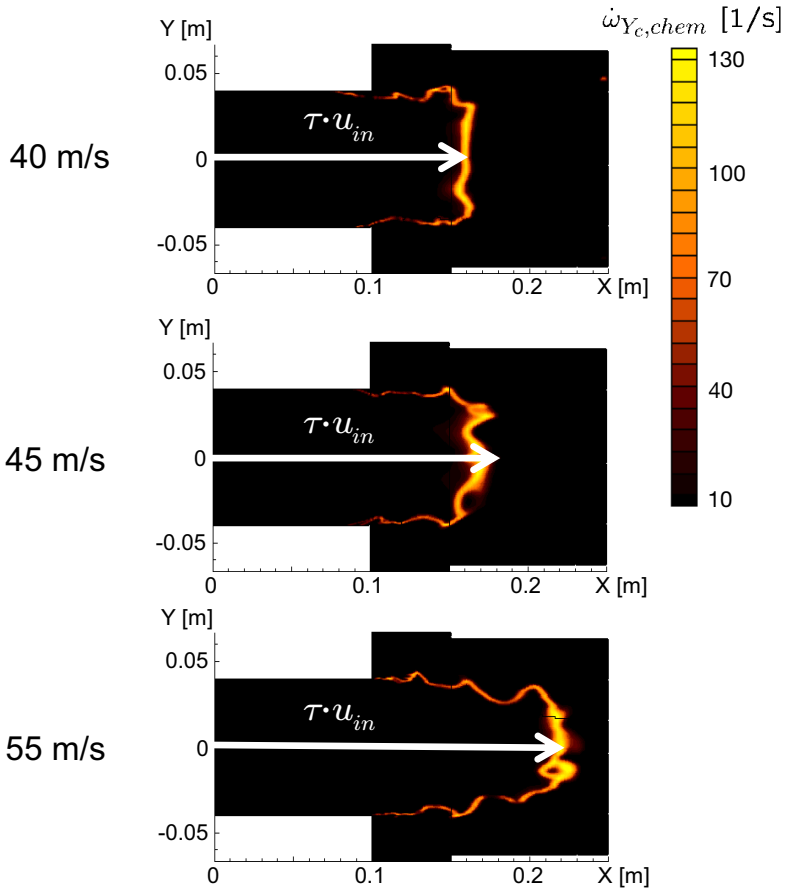

Figure 5.1: Impact of inlet velocity on flame position given by chemical source term in a single stochastic field

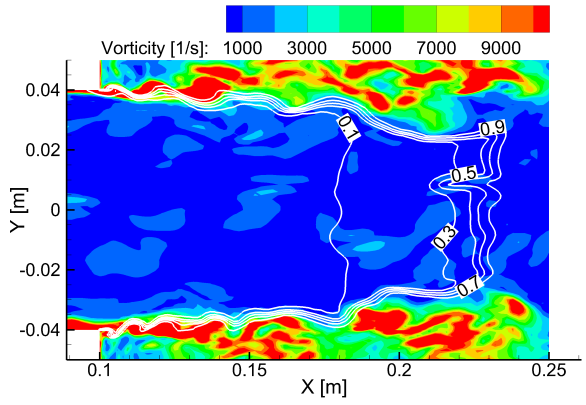

Figure 5.2: Instantaneous distribution of vorticity (filled contours) and normalised progress variable (isolines) for case without excitation

field, e.g. lead to intense vortex formation and roll-up behind the area jump. Hence, strong flame-acoustics coupling linked to coherent flame wrinkling is expected in the shear layer close to the burner exit, while possibly other feedback mechanisms might dominate the flame response further downstream.

5.2 Flame dynamics without considering pressure sensitivity

The response to acoustic excitation is investigated by exciting the transverse modes as explained in section 3.2.4. The use of single-frequency excitation offers many advantages for the post-processing and interpretation of LES data, since the acoustic fluctuations can be separated from the broadband turbulent fluctuations. As a consequence nearly all post-processing in this study relies on harmonic analysis, in order to be able to visualise the interaction of acoustics and flame only. The filter-based post-processing was performed on time series corresponding to a total flow time of 12 ms, for both 1T and 2T excitation cases. Before starting the excitation, a stable mean solution was calculated over more than ten residence times.

For transverse modes, the flame cannot be considered to be acoustically compact, as commonly done for low-frequency, axial modes. Thus, the flame dynamics cannot be analysed in terms of global heat release on the overall flame scale, but has to be characterised locally as explained in chapter 2.

5.2.1 Phenomenological description

Acoustic excitation is applied for an inlet velocity of 55 m/s. The frequency and the direction of the momentum source terms are chosen such as to excite a 1T mode at 3838 Hz and a 2T mode at 7450 Hz, with the mode shapes shown in Fig. 3.6. In both cases the flame responds to acoustic fluctuations, with a much stronger response for the 3838 Hz excitation. Apparent reasons are the reduced acoustic fluctuation amplitudes obtained for the 2T case and a higher tendency toward coherent vortex formation in the 1T case. The lower acoustic amplitude level for the 2T excitation is due to three main reasons: Firstly, despite the shorter oscillation period, the same excitation amplitude was chosen for the momentum source term. The acoustics of the system behave similarly

to a driven damped oscillator; to reach the same amplitude level at higher frequencies, one has to increase the excitation amplitude in proportion to the change in frequency. A quantitative description of acoustic amplitude dependence on the excitation amplitude at the boundary can be found in the work of Schuermans [104]. Secondly, the frequency chosen for the excitation is probably not matching exactly with the acoustic resonance frequencies of the combustor. Indeed, the frequency was chosen on the basis of a Fourier analysis of pressure signals during the initiation run, while the frequency for the 1T excitation was obtained from a FEM analysis. Thirdly, acoustic losses through the open boundaries are significantly higher for the 2T excitation, due to the longitudinal mode components.

When looking at transient evolutions, both excitation cases show coherent vortex formation and flame wrinkling behind the burner exit, while in the unexcited case vorticity distributions and flame surface shape are characterised by random, turbulent fluctuations. The periodic wrinkling can be illustrated by phase-lock average contours of the reaction progress, as illustrated in Fig. 5.3 for the 1T excitation case. A more detailed description of the coherent wrinkle formation was given by Meraner [73] in a diploma thesis supervised by the author of the present work.

The observed degree of flame wrinkling is much stronger for the 1T case. This can be clearly seen from the comparison of average heat release distributions shown in Fig. 5.4. When compared to the unexcited case, the shear layers are modulated noticeably in particular by the 1T excitation. The strong flame wrinkling results in a very thick turbulent flame brush close to the burner exit and in a steeper flame front inclined into the jet of fresh reactants. These observations are in agreement with the previous analysis of flame stabilisation: Due to the wrinkling and the increased flame surface area in the 1T case, flame propagation is promoted significantly, resulting in a steeper flame front and a smaller auto-ignition zone in the jet core. For the 2T excitation case, the flame wrinkling also results in a thickening of the mean flame shape close to the burner exit, but to a smaller extent. Hence, the flame resembles the one of the unexcited case.

In the present section, results of a frequency analysis will be shown for both the 1T and the 2T case. To this end, transient data were exported during the simulation, containing all relevant flow parameters in the vertical symmetry

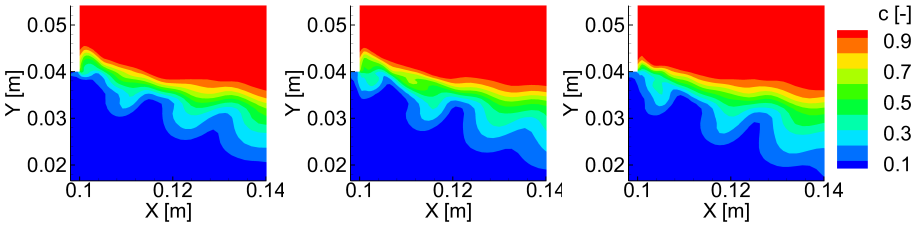

Figure 5.3: Phase lock evolution of normalised reaction progress over fluctuation period of 1T case (left: 0° phase, middle: 120°, right: 240°)

plane shown in Fig. 3.3. The frequency analysis was performed for each single cell element using the recorded time series. By this means the fluctuation amplitude and phase at the frequency of interest can be characterised locally.

Flame dynamics related to 1T excitation case The rms distribution of the heat release rate oscillations is shown on the left in Fig. 5.5 for the 1T excitation case, indicating strong fluctuations, especially close to the burner exit. Two distinct regions can be identified along each shear layer, namely two parallel bands appearing behind the burner exit on the inner and outer side of the shear layer. Each band is characterised by a periodic alternation of strong and weak fluctuations.

More insight can be obtained from the analysis of the phase distributions of heat release shown on the right side of Fig. 5.5. Therefore, a local phase lag was determined for the heat release in each cell. The pressure signal recorded in the upper shear layer 1 cm downstream of the burner exit was used as reference signal (see "Reference point" in Fig. 5.5). In order to ease the interpretation, the phase lag distributions were overlaid with a luminosity mask proportional to the rms intensity of heat release fluctuations, as previously done by Hauser et al. [37]. Hence, the phase lag distribution of Fig. 5.5 emphasises regions where significant heat release fluctuations occur.

The phase representation clearly shows the same two bands that were observed in the rms plots. Both bands appear to be influenced by vortex formation and flame wrinkling. This can be concluded from the appearance of a continuously changing phase spectrum, since the flame wrinkles formed are convected downstream and therefore lead to a non-constant phase lag with respect to the acoustic reference signal.

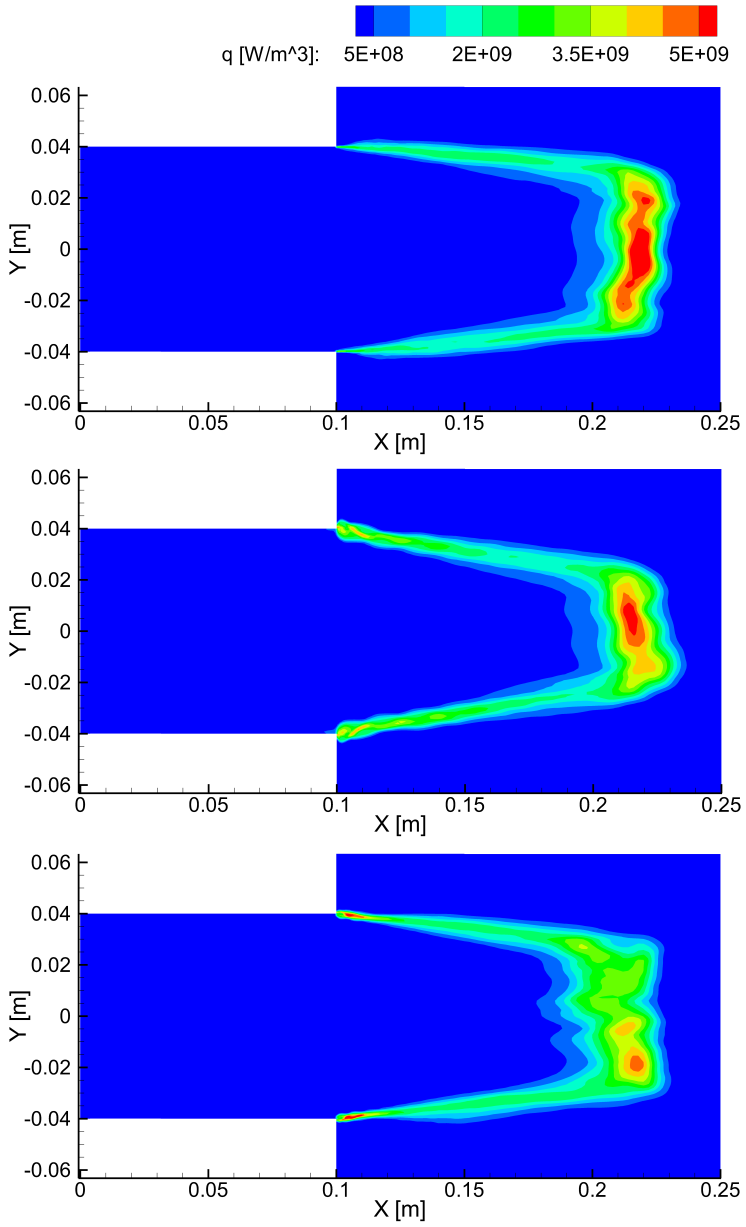

Figure 5.4: Distribution of average heat release rate in symmetry plane for unexcited case (top), 1T and 2T excitation cases (middle and bottom)

An important observation regarding the heat release rate fluctuations is the fact that the two bands within a single shear layer are phase-shifted by ±180° with respect to each other. This indicates a further characteristic flame behaviour, namely a periodic vertical displacement of the flame. Indeed, the transverse acoustic velocity fluctuations move the flame up and down. Such a displacement leads to a periodic modulation of the local heat release rate at a given spatial location and to the reported phase reversal within the flame

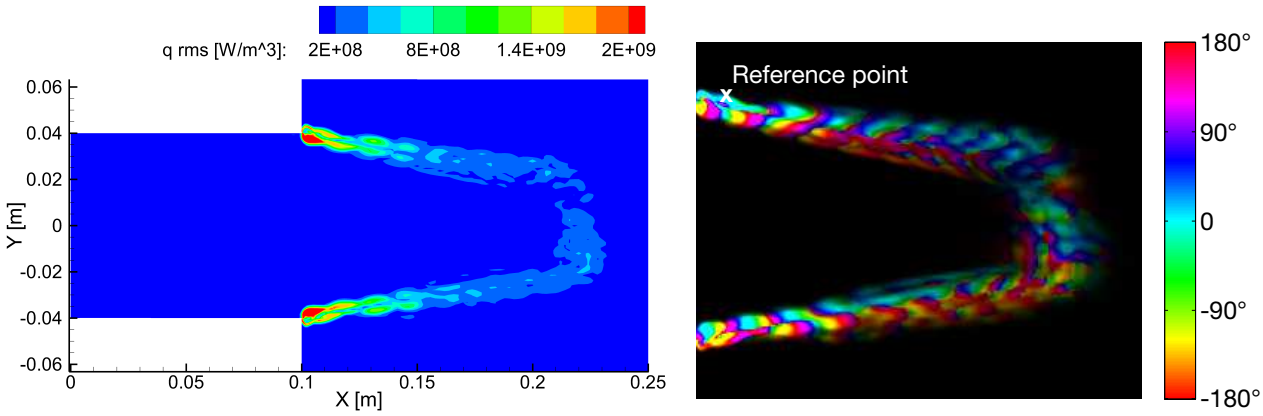

Figure 5.5: Distributions of rms values (left) and phase lag (right) of heat release rate oscillations for 1T excitation case

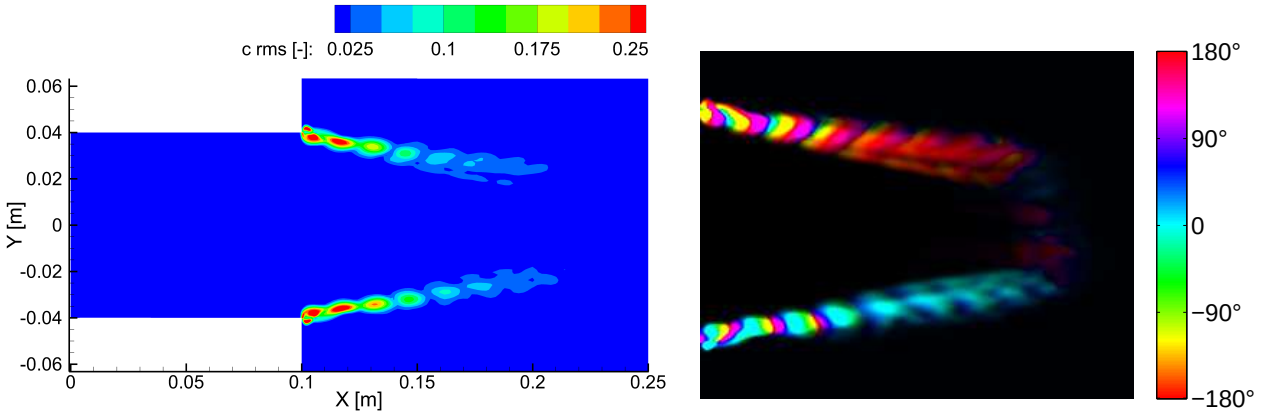

Figure 5.6: Distributions of rms values (left) and phase lag (right) of progress variable oscillations for 1T excitation case

brush. In the upper shear layer, the band lying above shows a dominant phase lag of 0° with respect to the pressure signal. Hence, it can be concluded that the flame reaches its uppermost position at the moment of maximum pressure rise. Similar observations were made by Huang et al. [43], Mery et al. [74], and Schwing et al. [109]; the latter work also developed a model for the impact of such a periodic flame displacement on thermoacoustic stability, as mentioned earlier.

This interpretation of the heat release rate fluctuations is further supported when considering the fluctuations of the reaction progress. The superposition of convected flame wrinkles and transverse displacement leads to a characteristic pattern in the amplitude distribution, as can be seen in Fig. 5.6 for

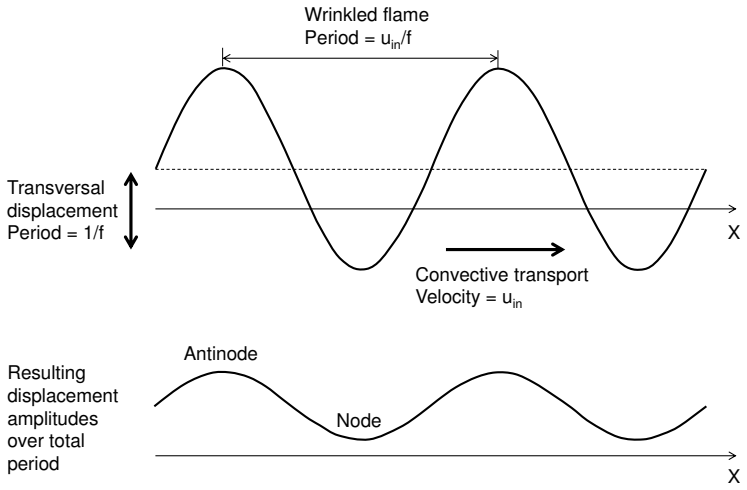

Figure 5.7: Schematic description of flame dynamics in shear layers: superposition and interference of convected flame wrinkles and acoustic displacement

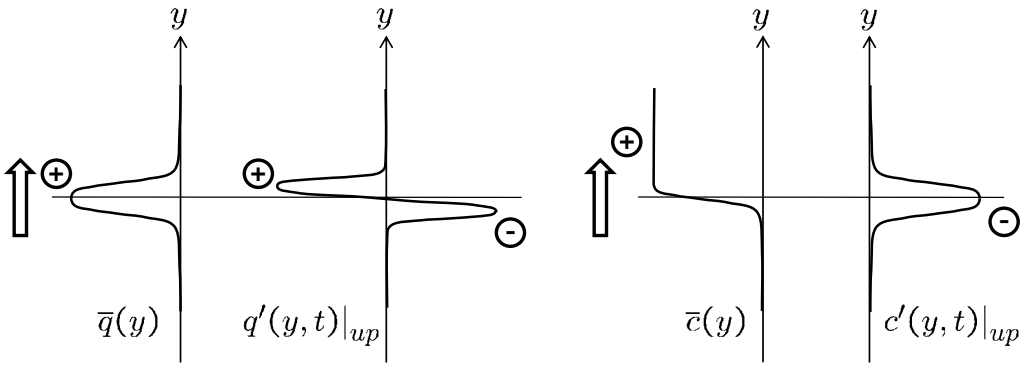

Figure 5.8: Sketch of instantaneous modulations of heat release rate and reaction progress due to upward displacement of the mean profile

the 1T case. Whereas each effect for itself would create a straight regular band of reaction progress fluctuation amplitudes, the superposition of both leads to interference and the appearance of flame displacement nodes and antinodes. The interference can be modelled by a travelling wave, representing the convectively transported wrinkled flame, which is moreover moved up and down periodically. As illustrated in Fig. 5.7, the superposition of both effects yields an amplitude evolution similar to the rms distribution observed in LES. Deviations from this pattern can only be observed close to the flame attachment point at the burner exit, where the flame wrinkling develops and a more complex interaction takes place.

The phase plot for the reaction progress is shown on the right in Fig. 5.6. Close to the burner exit, the phase distributions of reaction progress and heat release rate look similar, with the characteristic rainbow pattern indicating the convection of the flame wrinkles. But further downstream, the reaction progress in the upper shear layer has a constant phase of $\pm 180°$ over the entire flame brush. This result appears sensible considering that the flame displacement in this region is mainly due to the acoustic velocity. Indeed, the reaction progress within a flame is a monotonously growing function in contrary to the heat release rate. Figure 5.8 sketches the instantaneous fluctuations of heat release rate and progress variable when their respective mean profiles are displaced upward. This explains the differences in phase distribution observed between the heat release rate and the reaction progress.

The preceding discussion focussed strongly on the flame propagation in the shear layers. The heat release fluctuations in the auto-ignition zone are comparatively weak, as can be seen in the rms distribution. Moreover, the corresponding phase is rather uncorrelated to the pressure signal. One can conclude that for the 1T excitation case mostly random heat release fluctuations appear in the auto-ignition zone. Indeed, only density fluctuations may cause a coherent flame response in the absence of pressure sensitivity. However, since the auto-ignition zone is located close to the acoustic pressure node, the resulting amplitudes are rather weak.

Flame dynamics related to 2T excitation case The flame response to the 2T mode is generally weaker, mainly because of lower acoustic amplitudes. Regarding the shear layers, it shows the same qualitative behaviour as for the 1T mode, see for instance the rms and phase distribution of the heat release rate shown in Fig. 5.9. Again, two parallel bands can be observed in each shear layer, which are phase-shifted by $\pm 180°$ with respect to each other due to the vertical displacement. Furthermore, phase changes continuously, indicating a periodic flame wrinkling. The superposition of these two flame movements again leads to an alternation of progress variable nodes and anti-nodes, as can be seen in the progress variable plots of Fig. 5.10, but, in comparison to Fig. 5.6, with a reduced axial distance between them due to the increased frequency and the consequently smaller wrinkles.

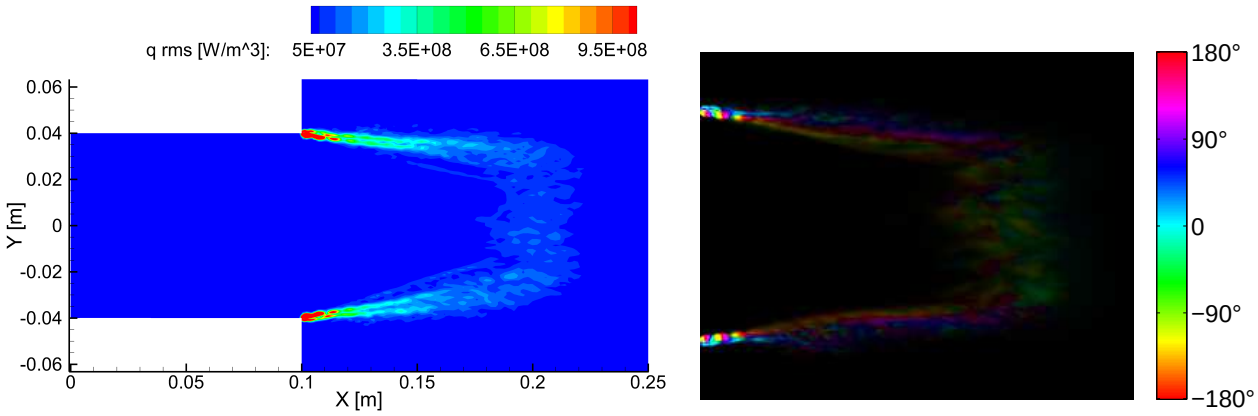

Figure 5.9: Distributions of rms values (left) and phase lag (right) of heat release rate oscillations for 2T excitation case

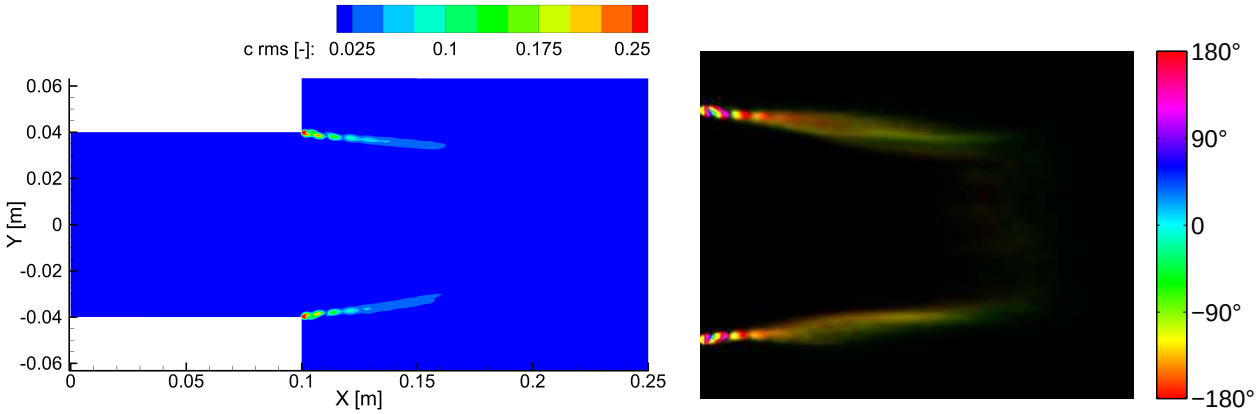

Figure 5.10: Distributions of rms values (left) and phase lag (right) of progress variable oscillations for 2T excitation case

As shown in Fig. 3.6, the axial mode components give rise to significant pressure oscillations on the burner axis, and hence in the auto-ignition zone. Consequently, the resulting density fluctuations cause a coherent response of the heat release in the auto-ignition zone. The resulting amplitudes are relatively small compared to the ones observed in the shear layer (see Fig. 5.5). The phase distribution with respect to the pressure at the reference point is nearly constant, and non-zero. Interestingly, the acoustic pressure signals at the reference point and in the auto-ignition zone show a similar phase-shift of approximately $-90°$, see Fig. 5.11. Pressure and heat release rate are thus in phase in the auto-ignition zone. A positive thermoacoustic feedback can thus be expected in this region.

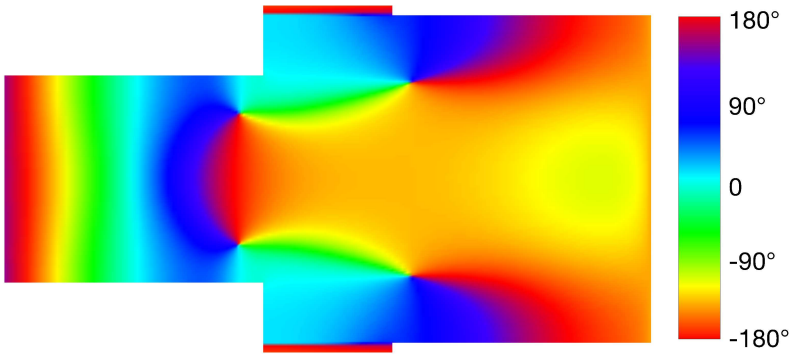

Figure 5.11: Phase distribution of pressure for 2T excitation case

In summary, the main conclusion from the local scale analysis is the observation of similar flame responses to both types of transverse excitation: periodic transverse flame displacement overlaid with the convective transport of periodic flame wrinkles. Noticeable variations of the local heat release rate appear due to these flame movements, but also due to density fluctuations. As presented in section 2.3.2, these modulations can cause a thermoacoustic feedback. A quantitative analysis thereof is made in the following.

5.2.2 Distribution of the Rayleigh index

The distribution of the thermoacoustic source term can be directly computed from the harmonic analysis of the flow variables. Such a volumetric Rayleigh index $\mathrm{ri}(x,y)$ can be calculated using its common definition, with the time series of pressure and heat release rate at each mesh element, which are bandpass-filtered around the excitation frequency:

$$\mathrm{ri}(x,y) = \int_0^{\mathcal{T}} p'(x,y,t)\dot{q}'(x,y,t)\,dt \tag{5.1}$$

The results obtained for the 1T mode are shown on the left in Fig. 5.12. On the upstream end of the shear layer, one can clearly recognise the pattern caused by the interference of wrinkling and acoustic displacement. In the displacement nodes, the Rayleigh index shows only very low absolute values, whereas in the antinode locations, it reaches positive and negative maxima on the upper and lower side of the shear layer, respectively. This pattern occurs, since the uppermost flame position is reached when the maximum pressure rise develops in the upper combustor half. Further downstream, the node and anti-

node pattern disappears. Instead, straight positive and negative bands stretch on the outer and inner side of each shear layer, respectively. This is caused by the acoustic displacement, which is predominant on the downstream end of the shear layer. The positive region is larger; the acoustic displacement thus causes a positive thermoacoustic feedback, as predicted in section 2.3.2.

The axial distribution of the Rayleigh index can be further investigated by splitting the observation plane into rectangular layers placed along the central axis and stretching over the entire combustor height. For each of these layers, an area-integrated Rayleigh index can be computed using

$$\mathrm{RI}_i = \int_{A_i} \int_0^{\mathcal{T}} p'(x,y,t)\,\dot{q}'(x,y,t)\,dt\,dA = \int_{A_i} \mathrm{ri}(x,y)\,dA. \tag{5.2}$$

The corresponding evolution for the 1T excitation case is shown on the right in Fig. 5.12. One can clearly observe the strong alternations in the upstream region due to the flame wrinkling as well as the regular positive evolution in the region dominated by the acoustic displacement. As it was postulated in the discussion of the heat release rate fluctuations, only weak thermoacoustic feedback is observed in the auto-ignition region.

Both planar and axial distributions of the Rayleigh index are further given in Fig. 5.13 for the 2T excitation case. In the upstream region of the shear layer, the evolutions are analogous to the 1T case with the same pattern caused by the flame wrinkling. Further downstream in the shear layer, the complex shape of the acoustic mode does not allow an unambiguous analysis of the feedback. However, in the auto-ignition zone, the positive contribution of density fluctuations can now be clearly observed.

The previous results only use data gathered in the central (x,y)-symmetry plane shown in Fig. 3.3. In addition, Rayleigh index distributions in a transverse monitor crossplane are shown in Fig. 5.14 for both excitation cases. No significant alterations of the thermoacoustic feedback appear along the circumference in particular for the 1T excitation case. The Rayleigh index for the 2T case shows stronger variations, that are linked to the more complex mode shape, which also contains transverse mode components in the third spatial direction. The regularity of the profiles indicates that the description of the feedback mechanisms made previously holds for the entire flame region. For the quantification of the total flame feedback, the entire 3D domain should preferably be analysed, in particular when mixed modes are of interest.

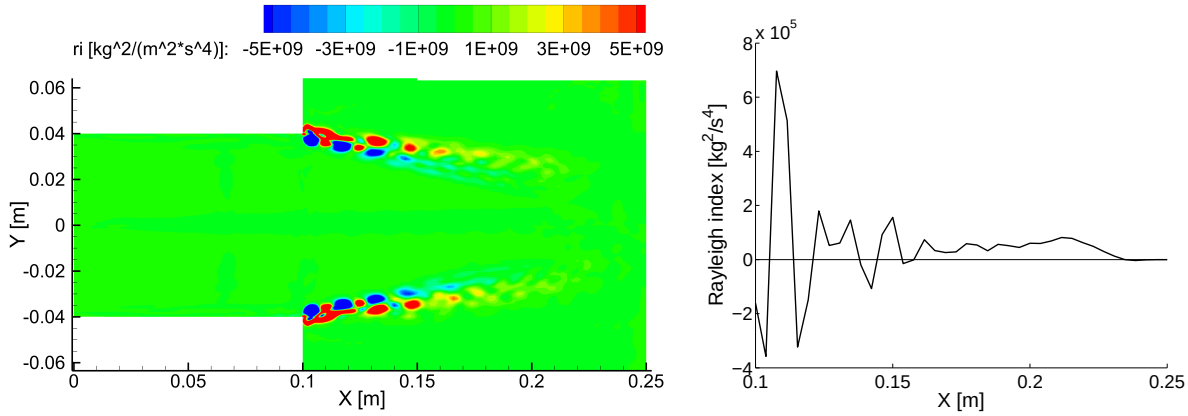

Figure 5.12: Planar (left) and axial (right) distributions of Rayleigh index for 1T excitation case. Axial distribution calculated from Eq. (5.2).

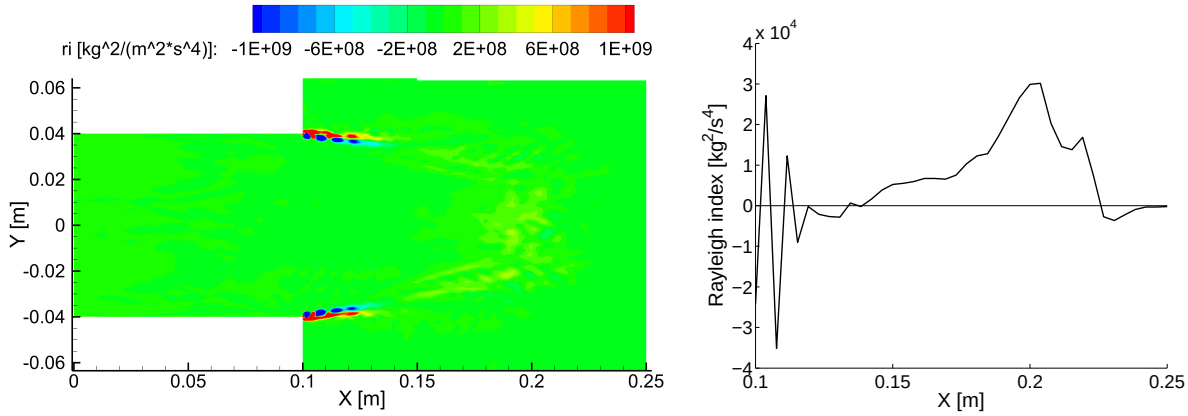

Figure 5.13: Planar (left) and axial (right) distributions of Rayleigh index for 2T excitation case. Axial distribution calculated from Eq. (5.2).

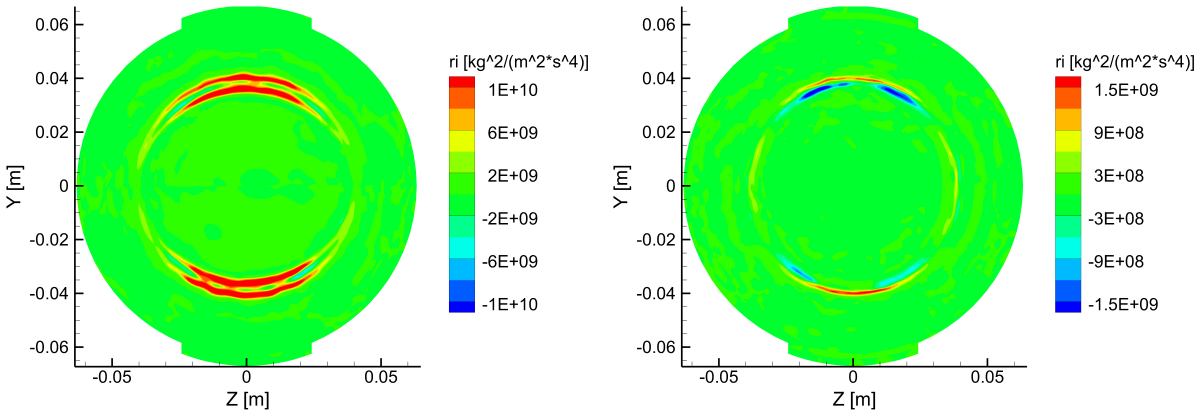

Figure 5.14: Distribution of Rayleigh index for 1T (left) and 2T (right) excitation case in crossplane at position $x = 0.11$ m

5.3 Flame dynamics including pressure sensitivity

5.3.1 Phenomenological description

Excited simulations taking into account the pressure sensitivity are also conducted using the method presented in section 4.4.6, with a constant value of $\varphi_p = 5$. Part of the results have been published by the author in [125]. As mentioned in chapter 4, this value represents a worst case scenario, as a slight decrease of the sensitivity is observed during the ignition progress. For stability predictions in industrial design processes, one ought to use a pressure sensitivity depending on reaction progress and mixture fraction; this would ask for an additional dimension of the chemistry tables. For the present work, the choice of a constant value of φ_p is considered to be sufficient for getting a correct estimation of the thermoacoustic feedback linked to the pressure sensitivity. Moreover, the assumption of a constant value was found to not alter the qualitative behaviour of the mechanism.

Comparing the weighted phase distributions of the heat release rate shown in Fig. 5.15 for both excited modes to the ones of Figs. 5.5 and 5.9, one can recognise the significant impact of the pressure sensitivity. While the upstream part of the shear layer, characterised by the intense flame wrinkling, remains rather unchanged, the phase distributions are strongly shifted toward a value in the range of $[0°;90°]$ in the downstream part of the upper shear layer for the 1T excitation case. This could be expected since the pressure sensitivity causes an

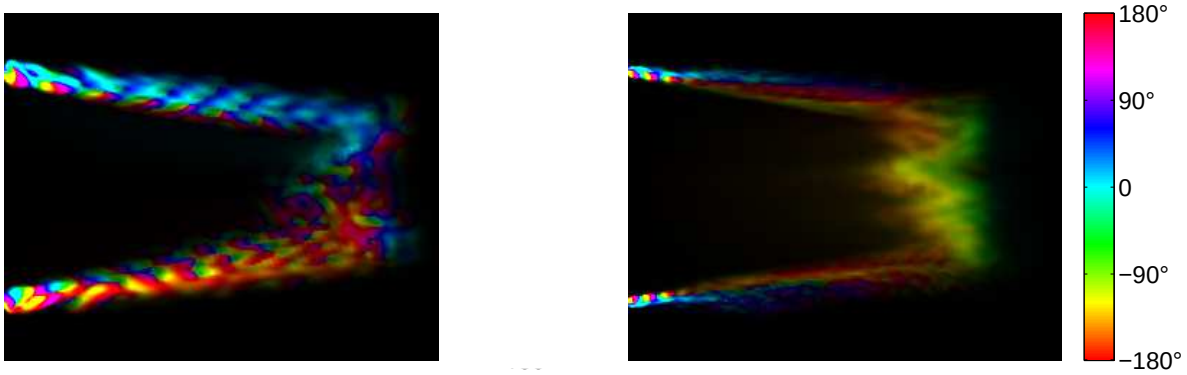

Figure 5.15: Distributions of heat release phase lag for 1T (left) and 2T (right) excitation cases with pressure sensitivity

additional signal component, which is in phase with the pressure. Hence, the observed pattern corresponds to the overlay of a constant field with a phase of 0° on top of the two bands with phases of 0° and ±180° that were observed in the case without pressure sensitivity. As before, the flame response in the auto-ignition zone remains rather uncorrelated because of the low pressure fluctuations at this location.

Noticeable differences due to the pressure sensitivity appear, however, for the 2T mode at the downstream end of the shear layer and in the auto-ignition zone, in which a very regular phase of approximately −90° is observed in a wide region. This clearly indicates the dominance of the pressure sensitivity in this zone, which drives the heat release rate oscillations to be nearly in phase with the local pressure (see Fig. 5.11). Some slight dephasing can be observed locally at the downstream end of the auto-ignition zone. It is thought to be caused by the time-delaying effect of the pressure sensitivity, as discussed in section 4.4.5.3.

5.3.2 Distribution of the Rayleigh index

The thermoacoustic feedback is determined with the same postprocessing tools. The planar and axial distributions of the Rayleigh index are shown for the 1T and 2T excitation cases with pressure sensitivity in Figs. 5.16 and 5.17, respectively. In comparison with the previous results (see Figs. 5.12 and 5.13), the feedback appears to be generally shifted toward positive values, as indicated by the phase relations. This is particularly true for the shear layer region in the 1T case and for the auto-ignition region in the 2T case.

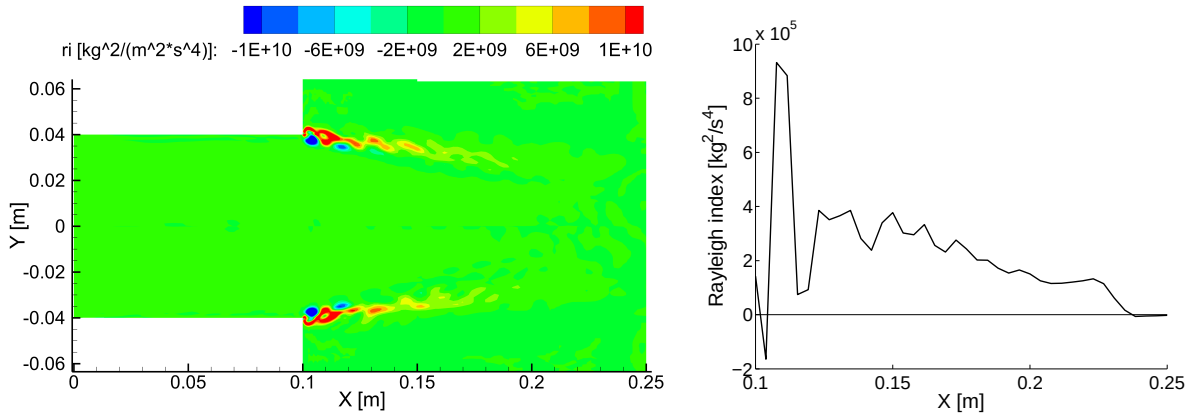

Figure 5.16: Planar (left) and axial (right) distributions of Rayleigh index for 1T excitation case with pressure sensitivity

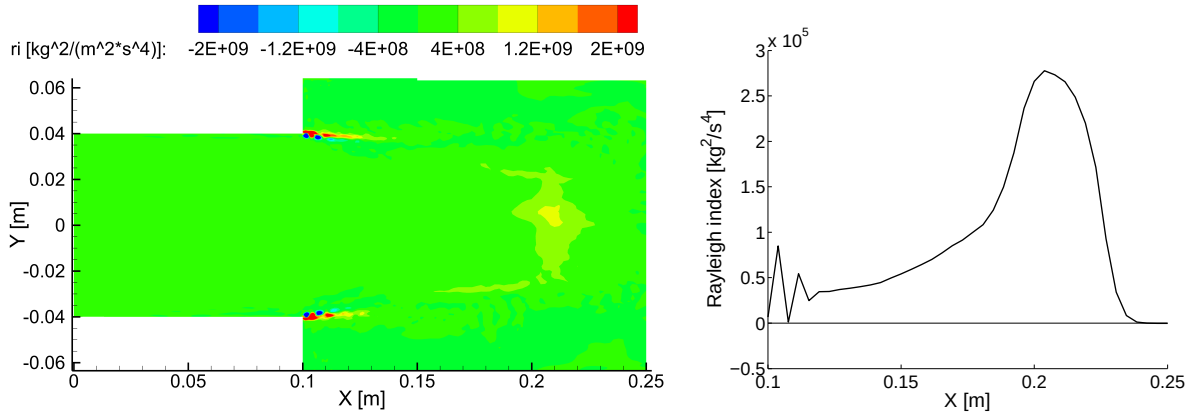

Figure 5.17: Planar (left) and axial (right) distributions of Rayleigh index for 2T excitation case with pressure sensitivity

5.4 Theoretical model for the decomposition of heat release fluctuations and flame feedback

The previous analysis focussed on the phenomenological description of the flame dynamics and gave an overall quantitative description of the thermoacoustic feedback generated by the flame. Distinct types of flame feedback have been observed and are cast in the present section into a theoretical model, which decomposes the local heat release fluctuations into individual contributions. In the following section, this will be used to quantify the individual feedback contributions observed in LES and thus allows to gain a better overall understanding of flame dynamics.

The theoretical formalism was already described by Zellhuber et al. in [127] and relies on the introduction of a moving frame ξ, ψ, ζ which sits on the displaced isocontour of heat release rate. This will be used in the following to separate between spatiotemporal and temporal fluctuations of the heat release rate. The coordinates in stationary and moving frames are related to each other by

$$x = \xi + \Delta_x(x, y, z, t), \tag{5.3}$$

$$y = \psi + \Delta_y(x, y, z, t), \tag{5.4}$$

$$z = \zeta + \Delta_z(x, y, z, t), \tag{5.5}$$

with Δ_x, Δ_y and Δ_z denoting the components of the instantaneous displacement vector. Such a displacement can be of any kind; for producing coherent, local heat release rate fluctuations it is merely required to oscillate at the frequency of interest.

Introducing vector notation with

$$\vec{x} = \begin{pmatrix} x \\ y \\ z \end{pmatrix}, \ \vec{\xi} = \begin{pmatrix} \xi \\ \psi \\ \zeta \end{pmatrix}, \ \vec{\Delta} = \begin{pmatrix} \Delta_x \\ \Delta_y \\ \Delta_z \end{pmatrix}$$

and the differential operator

$$\vec{\nabla} = \begin{pmatrix} \frac{\partial}{\partial x} \\ \frac{\partial}{\partial y} \\ \frac{\partial}{\partial z} \end{pmatrix},$$

one may introduce the heat release rate in the moving frame

$$\dot{q}_{\vec{\xi}}(\vec{\xi}, t) = \dot{q}(\vec{x}, t), \tag{5.6}$$

which can also be split into mean and fluctuating values:

$$\dot{q}_{\vec{\xi}}(\vec{\xi}, t) = \overline{\dot{q}}_{\vec{\xi}}(\vec{\xi}) + \dot{q}'_{\vec{\xi}}(\vec{\xi}, t). \tag{5.7}$$

These moving frame coordinates therefore allow to distinguish between the spatiotemporal flame displacement and the temporal variations of the burning rate. It can be seen as analogous to the distinction made between displacement and consumption speed when defining laminar flame speeds, see

Poinsot and Veynante [91]. Equations (5.6) and (5.7) can be interpreted more easily when imagining a flame with constant mass-burning rate, which is periodically moved up and down. Due to the constant burning rate, the oscillating term $\dot{q}'_{\vec{\xi}}$ in Eq. (5.7) will be zero. Hence, the heat release rate in the moving frame is constant and equal to its mean value $\overline{\dot{q}}_{\vec{\xi}}(\vec{\xi})$. However, local heat release rate fluctuations will appear in the reference frame due to the displacement of the flame. If one now considers a non-constant burning rate, there will additionally be temporal fluctuations of the heat release rate in the moving frame. The following derivation aims at expressing the local heat release rate fluctuations in the fixed reference frame as an explicit function of the displacement and of burning-rate oscillations.

To this end, the moving frame coordinates in Eq. (5.6) are expanded, yielding

$$\dot{q}(\vec{x},t) = \dot{q}_{\vec{\xi}}(\vec{x}-\vec{\Delta},t) \tag{5.8}$$

and after a first-order Taylor expansion in space assuming small displacement values:

$$\dot{q}(\vec{x},t) \approx \dot{q}_{\vec{\xi}}(\vec{x},t) - \vec{\nabla}\dot{q}_{\vec{\xi}}(\vec{x},t)\cdot\vec{\Delta}(\vec{x},t). \tag{5.9}$$

Using Eq. (5.7), one may write

$$\overline{\dot{q}}(\vec{x}) + \dot{q}'(\vec{x},t) \approx \overline{\dot{q}}_{\vec{\xi}}(\vec{x}) + \dot{q}'_{\vec{\xi}}(\vec{x},t) - \vec{\nabla}\overline{\dot{q}}_{\vec{\xi}}(\vec{x})\cdot\vec{\Delta}(\vec{x},t) - \vec{\nabla}\dot{q}'_{\vec{\xi}}(\vec{x},t)\cdot\vec{\Delta}(\vec{x},t), \tag{5.10}$$

and finally, after reordering and neglecting higher order fluctuation terms:

$$\overline{\dot{q}}(\vec{x}) + \dot{q}'(\vec{x},t) \approx \overline{\dot{q}}_{\vec{\xi}}(\vec{x}) - \vec{\nabla}\overline{\dot{q}}_{\vec{\xi}}(\vec{x})\cdot\vec{\Delta}(\vec{x},t) + \dot{q}'_{\vec{\xi}}(\vec{x},t). \tag{5.11}$$

This relation holds in a linear context only and leads to the following approximate relations between mean and fluctuating values of heat release rate in both frames:

$$\overline{\dot{q}}(\vec{x}) \approx \overline{\dot{q}}_{\vec{\xi}}(\vec{x}), \tag{5.12}$$

$$\dot{q}'(\vec{x},t) \approx \underbrace{-\vec{\nabla}\overline{\dot{q}}(\vec{x})\cdot\vec{\Delta}(\vec{x},t)}_{=\dot{q}'_{\Delta}(\vec{x},t)} + \dot{q}'_{\vec{\xi}}(\vec{x},t). \tag{5.13}$$

Equation (5.13) contains a spatiotemporal contribution $\dot{q}'_{\Delta}$ linked to the displacement and a temporal contribution $\dot{q}'_{\vec{\xi}}$. The latter can be split up as previously into a density and a mass-specific reaction rate term, such that an expression similar to Eq. (2.13) can be recovered:

$$\frac{\dot{q}'}{\overline{\dot{q}}} = \frac{\rho'_{\vec{\xi}}}{\overline{\rho}} + \frac{\dot{\omega}'_{h,\vec{\xi}}}{\overline{\dot{\omega}}_h} + \frac{\dot{q}'_{\Delta}}{\overline{\dot{q}}} \tag{5.14}$$

However, Eq. (5.14) goes one step further than Eq. (2.13) by treating mass-specific reaction rate fluctuations in the moving frame and oscillations caused by displacement separately. As shown in the next section, this asks for special treatment when performing the decomposition for actual flow data. A procedure will be proposed on how to extract the corresponding data needed for quantifying the individual terms for the perfect premix test case.

Applying the definition of the Rayleigh index, one obtains the decomposition of the thermoacoustic feedback to high-frequency modes already introduced in Eq. (2.20)

$$\mathrm{RI} = \mathrm{RI}_\rho + \mathrm{RI}_{\dot{\omega}} + \mathrm{RI}_\Delta,$$

in which the individual terms can now be determined as follows:

$$\mathrm{RI}_\rho = \iiint \int_0^{\mathcal{T}} p'(\vec{x},t) \frac{\rho'_{\vec{\xi}}(\vec{x},t)}{\overline{\rho}(\vec{x})} \overline{\dot{q}}(\vec{x}) dt\, d\vec{x}, \tag{5.15}$$

$$\mathrm{RI}_{\dot{\omega}} = \iiint \int_0^{\mathcal{T}} p'(\vec{x},t) \frac{\dot{\omega}'_{h,\vec{\xi}}(\vec{x},t)}{\overline{\dot{\omega}}_h(\vec{x})} \overline{\dot{q}}(\vec{x}) dt\, d\vec{x}, \tag{5.16}$$

$$\mathrm{RI}_\Delta = -\iiint \int_0^{\mathcal{T}} p'(\vec{x},t) \vec{\nabla} \overline{\dot{q}}(\vec{x}) \cdot \vec{\Delta}(\vec{x},t) dt\, d\vec{x}. \tag{5.17}$$

The expression for the Rayleigh index linked to displacement differs from the one given by Schwing et al. [109] for thin flames, which was already introduced earlier in Eq. (2.19):

$$\mathrm{RI}_{\Delta,\text{Schwing et al.}} = \iiint \int_0^{\mathcal{T}} p'(\vec{x}+\vec{\Delta},t) \overline{\dot{q}}(\vec{x}) dt\, d\vec{x}.$$

In [127] it is shown that for sufficiently thin flames both expressions are equivalent. However, the expression given by Eq. (5.17) is generally valid and can as well be applied for homogeneous reaction zones.

Such a separation of the local heat release rate fluctuations into different contributions is a novelty of the present work. The motivation is rather straightforward: A quantitative comparison between the single effects allows to identify one (or more) feedback mechanism(s) which are most likely to drive an instability. Moreover, it shows possibilities to impact on the feedback level by design means, as will be discussed in chapter 7.

5.5 Quantification of thermoacoustic source term contributions

In the present section, the formalism introduced will be applied to and verified by a detailed postprocessing of the LES data. Therefore, the individual feedback contributions are quantified according to the formalism; the sum of these should equal the total Rayleigh index evolutions shown before.

The quantification of all individual contributions can only be performed for the shear layer region, where the flame has a very simple shape. It uses the filtered time series recorded in each cell element, but will proceed to a resampling into windows distributed along the upper shear layer, as shown in Fig. 5.18. Each zone of index i covers a surface A_i, representing a meso-scale observation window between the mesh scale size and the total flow domain scale. The high aspect ratio of the windows is chosen in order to ensure a high resolution in axial direction and to avoid that the flame moves out of the windows. The specific reasons for this choice are linked to the quantification of the individual distributions and will be explained in the following.

5.5.1 Decomposition methods

5.5.1.1 Displacement due to acoustic velocity

As mentioned first in [74, 109], the displacement of a thin flame by the velocity field of a transverse acoustic mode always contributes positively to the thermoacoustic source term. This is due to the fact that the flame is constantly displaced toward the positive acoustic pressure region. The same observation is made here, since the phase distributions of the reaction progress show such a synchronised displacement of the flame. A nice graphical representation of the mechanism can be found in [109].

For determining the magnitude of the feedback, it is necessary to calculate the corresponding acoustic displacement. Only displacement in y-direction is considered here, as transverse acoustic motions are predominant in the shear layer.

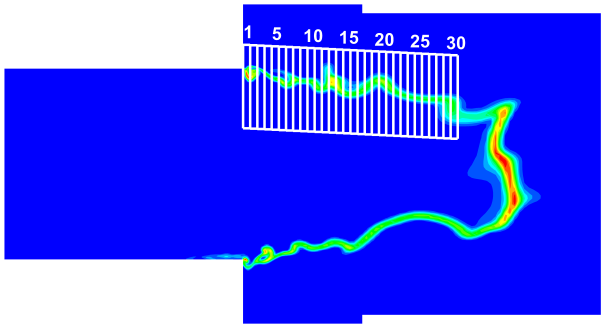

Figure 5.18: Definition of observation windows

One therefore needs to separate between acoustic and wrinkling displacement contributions. This is done by first removing the rotational part from the filtered velocity field. Indeed, the acoustic velocity field can be considered as a pure potential field. However, the vortex formation at the burner exit will also induce rotational velocity components at the excitation frequency. These are not proper acoustic fluctuations, but result from the interaction of the acoustic perturbations with the mean flow. Hence, these shall not be included for the calculation of the acoustic displacement, but will be considered separately within a residual displacement that is introduced later. The resulting potential velocity fluctuations in vertical direction v'_{pot} can be translated into a displacement by a time integration. When performing these operations on LES flow data, although most rotational components can be removed, the remaining velocity fluctuation distributions on the cell-scale are still not as smooth as typical distributions gained from FEM calculations. Therefore, an average acoustic displacement is calculated at the meso-scale for each observation window:

$$\Delta_{ac,i}(t) = \frac{1}{A_i}\int_{A_i}\int_0^t v'_{pot}(x,y,t)\,dt\,dA \tag{5.18}$$

Using Eq. (5.17), the corresponding Rayleigh index reads as

$$\mathrm{RI}_{\Delta,ac,i} = -\int_{A_i}\int_0^{\mathcal{T}} p'(x,y,t)\Delta_{ac,i}(t)\frac{\partial\overline{\dot{q}}(x,y)}{\partial y}dt\,dA. \tag{5.19}$$

Using the average displacement on the meso-scale implies that the flame brush is thin with respect to the acoustic mode. This is indeed the case when looking at the shear layer. The original formulation of Schwing et al. [109], given by Eq. (2.19), can therefore also be applied; the two expressions prove to be equivalent for the given case.

5.5.1.2 Displacement due to flame wrinkling

As mentioned earlier, there are additional displacement contributions besides the acoustic one. In the simulations made, it originates mostly from flame wrinkling in combination with convection (see Fig. 5.7), but other effects can also play a role. For instance, flame speed variations might also lead to differences between the acoustic and the actual flame displacement. For this reason, it is generally referred to as a *residual displacement*. This displacement is quantified by calculating the difference between the actual and the acoustic displacement values.

The actual or total flame displacement is directly evaluated on the meso-scale level. Therefore, a spatially averaged reaction progress $c_i(t)$ is calculated for each window and every timestep:

$$c_i(t) = \frac{1}{A_i} \int_{A_i} c(x, y, t) dA. \tag{5.20}$$

Bandpass-filtering these time series around the excitation frequency and applying simple geometric considerations, one can express the total flame displacement in one window of height H_i as:

$$\Delta_{tot,i}(t) = -c_i'(t) H_i. \tag{5.21}$$

This result can be compared to the mean acoustic displacement in a window, as introduced in Eq. (5.18). In regions of intense flame wrinkling, the total and the acoustic displacement are very likely to differ from each other. Hence, a residual displacement is introduced at window level, being defined as the difference between total and acoustic displacement values:

$$\Delta_{res,i}(t) = \Delta_{tot,i}(t) - \Delta_{ac,i}(t) \tag{5.22}$$

Computing a Fast Fourier Transform (FFT) at the excitation frequency of all three displacement signals for each window, one can directly compare them to each other, as shown in Fig. 5.19 for the real parts. The total displacement therefore appears to be strongly influenced by flame wrinkling close to the burner exit, whereas further downstream the acoustic displacement dominates. Assuming a constant residual displacement in a single window, the

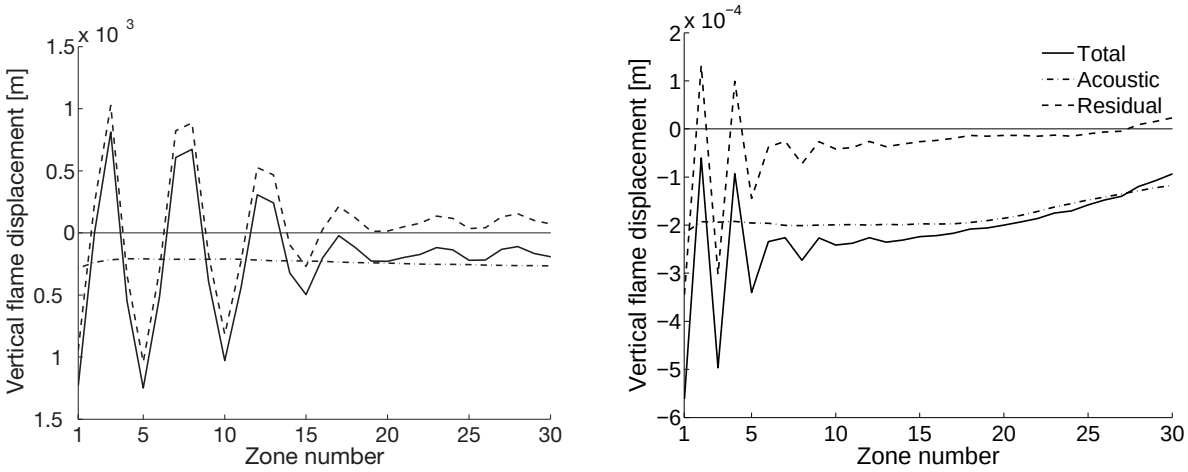

Figure 5.19: Real part of FFT for total, acoustic, and residual displacement along the shear layer for 1T (left) and 2T (right) excitation cases

source term contribution of the residual displacement can now also be computed:

$$\mathrm{RI}_{\Delta,res,i} = -\int_{A_i}\int_0^{\mathcal{T}} p'(x,y,t)\Delta_{res,i}(t)\frac{\partial\overline{\dot{q}}(x,y)}{\partial y}dt\,dA \tag{5.23}$$

5.5.1.3 Heat release modulations due to density fluctuations

The Rayleigh criterion is based on the fluctuations of volumetric heat release rate. Hence, density variations will play a role, since more mixture will be located in regions of higher density. In the (x,y) coordinate system, variations of density $\rho'(x,y)$ result from the acoustic compression as well as from the displacement, since the density is varying over the flame front. In order to derive the variations in the moving frame, which are needed to compute $\dot{q}'_{\vec{\xi}}$ (see Eq. (5.14)), a simplifying assumption is made, deriving the density variation directly from the pressure variation using the isentropic exponent. Indeed for isentropic state changes, one can write:

$$\frac{\rho'}{\overline{\rho}} \approx \frac{p'}{\gamma\overline{p}} \tag{5.24}$$

By using this approximation, the density variations caused by the periodic displacement are rendered insignificant, since they are of higher order, yielding the following expression for the respective source term contribution

$$\mathrm{RI}_{\rho,i} = \int_{A_i}\int_0^{\mathcal{T}} p'(x,y,t)\frac{p'(x,y,t)}{\gamma\overline{p}(x,y)}\overline{\dot{q}}(x,y)dt\,dA \tag{5.25}$$

Herein, the isentropic exponent γ is assumed to be constant over the flame front and equal to its value in the unburnt mixture. For the simulated flame, the variation of γ is below 2%, the assumption made is thus acceptable in the linear context.

5.5.1.4 Heat release modulations due to fluctuations of chemical consumption rates

The last contribution considered is related to variations of the chemical reaction rates, which can be derived by considering the mass specific heat release rate. The spatial averages of the mass-specific and of the volumetric heat release rate in a window can be expressed as follows:

$$\dot{\omega}_{h,i}(t) = \frac{1}{A_i}\int_{A_i}\frac{\dot{q}(x,y,t)}{\rho(x,y,t)}dA \tag{5.26}$$

$$\dot{q}_i(t) = \frac{1}{A_i}\int_{A_i}\dot{q}(x,y,t)dA \tag{5.27}$$

Since the meso-scale windows are defined in a way to always contain the flame, the fluctuations of $\dot{\omega}_{h,i}(t)$ equal the spatial average of the consumption rate fluctuations in the moving frame:

$$\dot{\omega}'_{h,i}(t) = \frac{1}{A_i}\int_{A_i}\dot{\omega}'_{h,\vec{\xi}}(t)dA. \tag{5.28}$$

Such a mass-specific reaction rate can be affected in three ways, either by modulating the flame surface in the window, by modulating the local equivalence ratio, or by direct changes of the reaction rates, which can occur e.g. via pressure sensitivity. The impact of mixing is of course zero in the perfect premix setup.

The corresponding Rayleigh term contribution can thus be written as

$$\mathrm{RI}_{\dot{\omega},i} = \int_0^{\mathcal{T}} p'_i(t)\frac{\dot{\omega}'_{h,i}(t)}{\overline{\dot{\omega}}_{h,i}}\overline{\dot{q}}_i dt. \tag{5.29}$$

after bandpass-filtering the time series of $\dot{\omega}_i(t)$ and assuming acoustic compactness of the observation window. This allows the use of the spatially averaged acoustic pressure fluctuations in the window $p'_i(t)$.

This term is generally considered as the dominant one for the feedback of compact flames, i.e. because of flame surface variations due to velocity fluctuations. The quantification results shown in the following section will elucidate whether the same conclusion holds for the feedback linked to high-frequency modes.

5.5.2 Quantification results

5.5.2.1 Without consideration of pressure sensitivity

Before comparing the different contributions with each other, the validity of the Rayleigh index decomposition shall first be verified. Therefore a comparison is made between the reference Rayleigh distribution for the meso-scale windows and a reconstructed distribution, computed as the sum of the previously derived individual source term contributions:

$$\mathrm{RI}_{reconstr,i} = \mathrm{RI}_{\Delta,ac,i} + \mathrm{RI}_{\Delta,res,i} + \mathrm{RI}_{\rho,i} + \mathrm{RI}_{\dot{\omega},i}. \tag{5.30}$$

The result of the reconstruction is shown for the 1T excitation case in Fig. 5.20 and proves to be very accurate. The procedure allows to properly capture the alternation of positive and negative regions in the wrinkled flame region, as well as the overall constant positive values in the downstream part.

This characteristic pattern can be linked to the spatial distribution of the source term contributions. Close to the burner exit, the Rayleigh index is strongly influenced by the intense flame wrinkling, which leads to increased residual flame displacement, and moreover to high fluctuations of the chemical consumption rates. The latter is of far higher importance for the local thermoacoustic source term, as the strong variations in the flame surface lead to intense coupling between the flame and the acoustics. However, it shall be underlined that for the 1T case the two effects do not have a strong impact on the global thermoacoustic source term (see Table 5.1), because of the alternation of positive and negative contributions along the shear layer. In the downstream part, the wrinkling is of very small impact even at the local scale,

whereas the contributions of density fluctuations and acoustic displacement cause the positive Rayleigh index in this region and therefore represent the largest contribution to the overall Rayleigh index. The constant positive sign of these two contributions is in agreement with theoretical expectations for thin flames.

	1T	2T
$\mathrm{RI}_{\delta,ac}$	301.3	64.6
$\mathrm{RI}_{\delta,res}$	3.3	3.7
RI_{ρ}	477.6	66.2
$\mathrm{RI}_{\dot{\omega}}$	-250.7	-95.7
$\mathrm{RI}_{reconstr}$	531.5	38.8
RI_{ref}	559.4	37.5
Error [%]	-4.97	3.51

Table 5.1: Quantification of different Rayleigh index contributions summed up over meso-scale windows ($\mathrm{RI} = \sum_i \mathrm{RI}_i$, all given in $\cdot 10^3 \frac{\mathrm{kg}^2}{\mathrm{s}^4}$). Error percentage of the reconstruction made from the individual contributions.

The application of the same analysis tools to the 2T excitation case shows as well a very good quality of the reconstruction, as shown in Fig. 5.21 and Table 5.1. This underlines the general applicability of the theoretical description proposed in section 2.3.2. Nevertheless, the relative importance of the individual contributions observed for the 1T mode in the simulation is different for the 2T excitation case. When looking at the individual curve evolutions and the summed values, it is observed that, contrary to the 1T mode, the contribution linked to the consumption rate and hence to the flame wrinkling now influences the global thermoacoustic source term more strongly. Physically, this can be explained by the smaller size of the vortices generated by the high-frequency 2T mode, due to the decreasing ratio between acoustic and convective timescale. The dissipation length of the vortices and hence the flame wrinkling is consequently shorter, what leads to a higher weighting of the region directly behind the area jump. As the latter shows a negative Rayleigh index, a stronger attenuating effect can be observed for the global contribution of the consumption rate, see Table 5.1. This is further aided by constantly negative values of this contribution in zones 1-15 and 20-30 (see Fig. 5.21), for which no clear explanation can be provided at present.

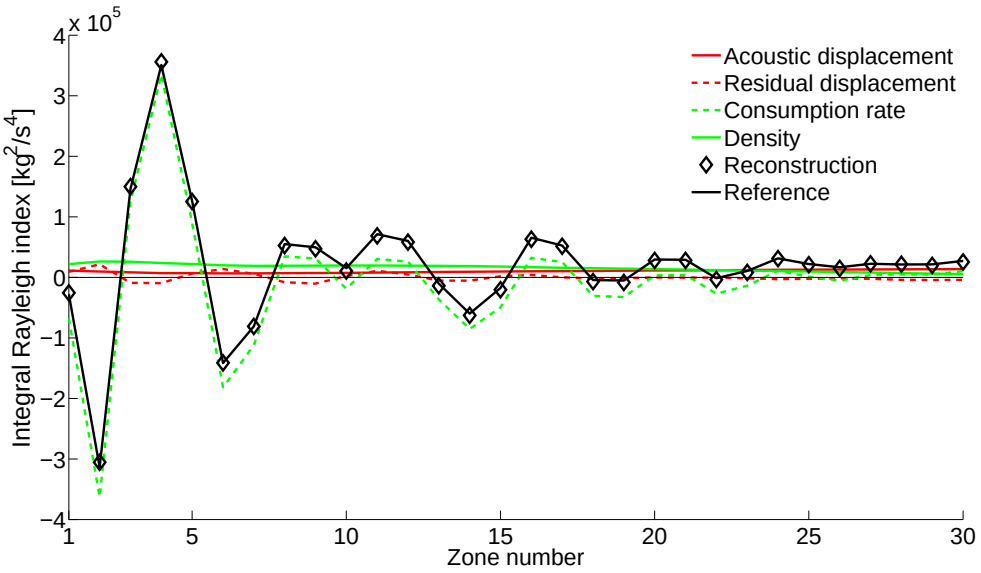

Figure 5.20: Rayleigh index evolutions along the shear layer for 1T excitation case – Comparison between reference and reconstructed evolutions, additional plots of individual contributions

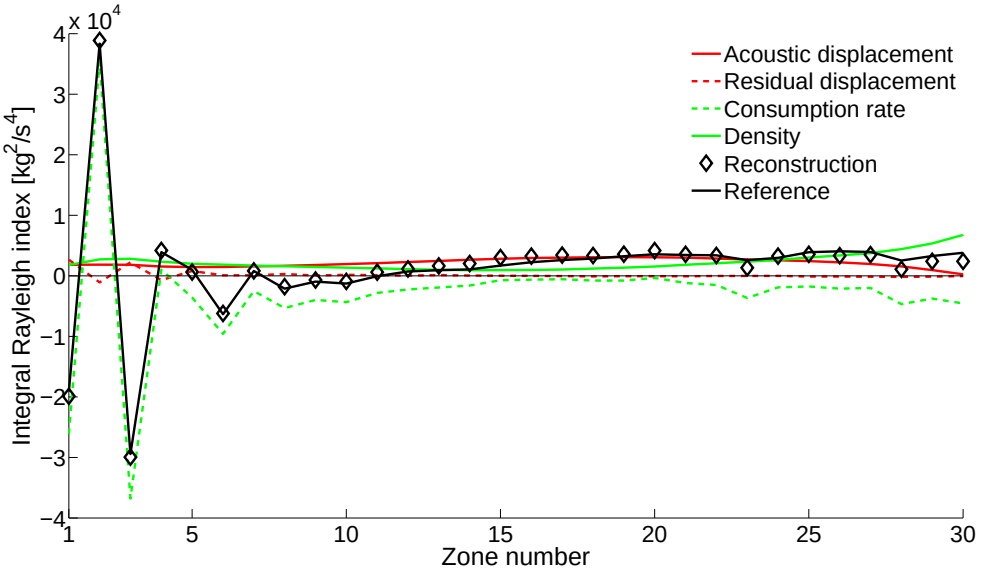

Figure 5.21: Rayleigh index evolutions along the shear layer for 2T excitation case – Comparison between reference and reconstructed evolutions, additional plots of individual contributions

5.5.2.2 With consideration of pressure sensitivity

One can observe in Figs. 5.22 and 5.23 that the pressure sensitivity adds a strictly positive term to the consumption rate distribution, shifting the Rayleigh index toward positive values. This holds for both the 1T and the 2T excitation cases. For the present configuration, the pressure sensitivity therefore represents the strongest contribution to the thermoacoustic feedback in the shear layers, as the contribution of the consumption rate is significantly increased for both excitation cases, as indicated in Table 5.2. The pressure sensitivity can be qualified as the dominant feedback mechanism for the perfect premix case.

The quality of the reconstruction is again very good for the 1T excitation. This also holds for the 2T excitation case in a large part of the shear layer. However, significant deviations appear between zones 10 and 23. This corresponds to the region in the middle of the shear layer where a phase reversal of the pressure occurs (see Fig. 5.11). As a consequence, the acoustic pressure in the flame varies strongly within a single meso-scale window, what violates the compactness assumption made for the window-based postprocessing of the contribution $\mathrm{RI}_{\dot{\omega}}$. This finally leads to the observed underestimation of the feedback, which did not appear for the case without pressure sensitivity, since no significant feedback linked to $\mathrm{RI}_{\dot{\omega}}$ appeared in the concerned zones.

	1T	2T
$\mathrm{RI}_{\delta,ac}$	249.0	80.0
$\mathrm{RI}_{\delta,res}$	-0.7	3.2
RI_{ρ}	538.9	69.3
$\mathrm{RI}_{\dot{\omega}}$	2851.5	245.8
$\mathrm{RI}_{reconstr}$	3638.6	398.4
RI_{ref}	3536.5	474.4
Error [%]	2.89	-16.0

Table 5.2: Quantification of different Rayleigh index contributions summed up over meso-scale windows ($\mathrm{RI} = \sum_i \mathrm{RI}_i$, all given in $\cdot 10^3 \frac{\mathrm{kg}^2}{\mathrm{s}^4}$). Error percentage regarding the reconstruction made from the individual contributions. Calculations made with pressure sensitivity.

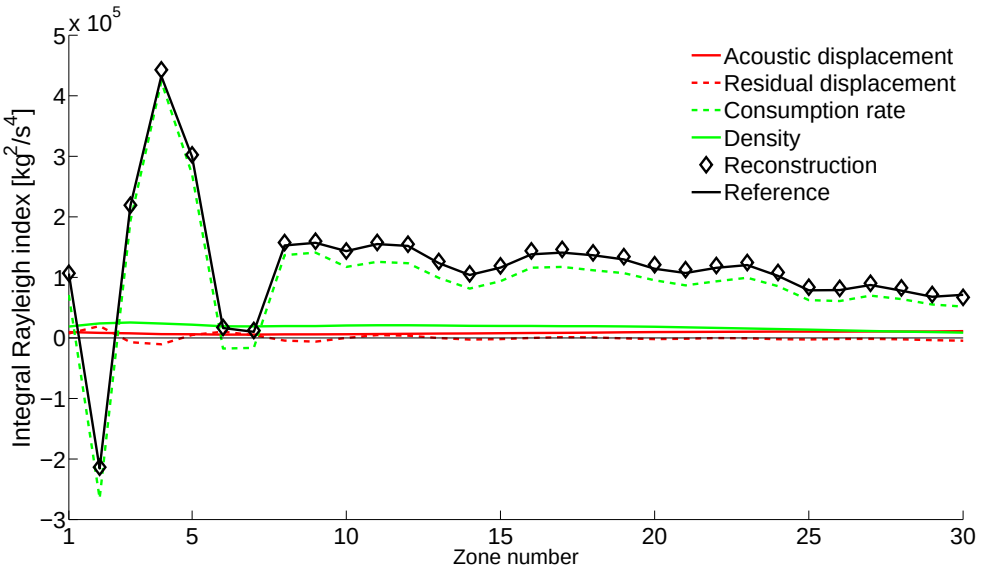

Figure 5.22: Rayleigh index evolutions along the shear layer for 1T excitation case with pressure sensitivity – Comparison between reference and reconstructed evolutions, additional plots of individual contributions

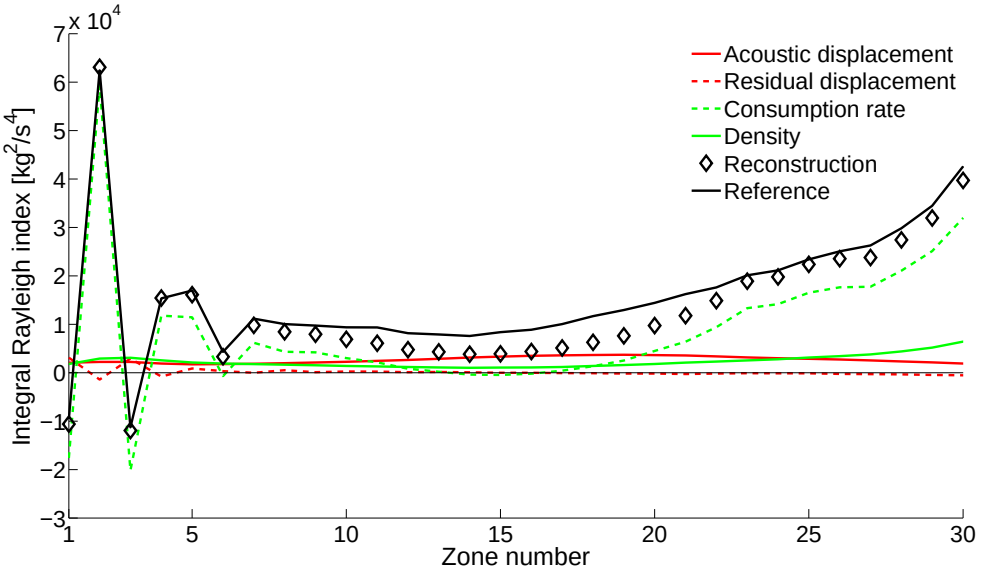

Figure 5.23: Rayleigh index evolutions along the shear layer for 2T excitation case with pressure sensitivity – Comparison between reference and reconstructed evolutions, additional plots of individual contributions

5.5.3 Summary of observations

From the perfect premix combustor simulations, a very detailed insight is obtained regarding the flame response to transverse acoustic waves. Different response mechanisms are observed, namely acoustic and residual (wrinkling) displacement, flame area changes due to wrinkling, density fluctuations, as well as reaction rate modulations for the cases with pressure sensitivity. The resulting patterns for fluctuation and Rayleigh index distributions were discussed on the basis of the response mechanisms. The separation of the Rayleigh index into individual contributions proposed in chapter 2 was successfully verified by a detailed postprocessing of the results. Deviations only appear for the 2T excitation case with pressure sensitivity, and are due to limitations of the postprocessing method when axial mode components are involved.

6 Large Eddy Simulation of Technical Premix Case

The technical premix case represents a further step toward industrial reheat burner configurations. As described in section 3.2.3.2, a fuel jet is injected as a cross-flow into the main stream of lean combustion products coming from a first stage. Compared to the perfect premix case, the physical complexity is significantly enhanced. Generally speaking, a similar flame behaviour is expected, with flame propagation in the shear layers and auto-ignition in the jet core. However, the presence of mixture inhomogeneities is likely to have an impact on the combustion process, on mean as well as on fluctuating values.

The simulation of this test case is extremely demanding in terms of computational ressources because of three principal reasons:

- The geometrical complexity of the flow requires several refined mesh regions: in the vicinity of the delta wing, around the crossflow injection, and in the shear layer region behind the area expansion. Resulting mesh sizes are thus relatively large; the mesh used with 2.2 million cells must be considered as relatively coarse (see section 3.2.3.2).
- The fluid residence time in the domain is very long due to the size of the domain and the medium range axial velocities; it lies around 30 ms. The residence time of the fuel from the injection point to the flame is about 10 ms. For comparison, the oscillation period of the 1T mode considered is equal to 0.33 ms.
- A reactive, ternary mixing case is considered here. When applying the stochastic fields method with 8 fields, in total 24 stochastic transport equations have to be solved, since two mixture fractions and one reaction progress are required.

Within this work, it was not possible to complete a simulation run that fulfills the usual requirements for long-time LES; i.e. a sufficiently long initia-

tion run and a recording time series of several residence times each. However, the oscillation period is much shorter than the overall flow timescale. Since the dynamic flame behavior is of primary interest, a relatively short recording time of 24 ms was selected, less than one residence time, but covering 72 oscillation periods. In addition, the initiation run was limited to two residence times and only one stochastic field was used. For these reasons, the study can only be considered as a preliminary one. Care was applied to have sufficiently long recording times for capturing the dynamic response of the flame. For more reliable quantitative results, which also capture the interaction of acoustics and turbulence-chemistry interaction, far more demanding computations are required. The computation of the recorded time series (without initiation) required 2400 CPU hours on new-generation Intel Xeon E5-2660 2.2 GHz processors. Increasing the number of fields to eight enlarges the demand by a factor of 2-2.5.

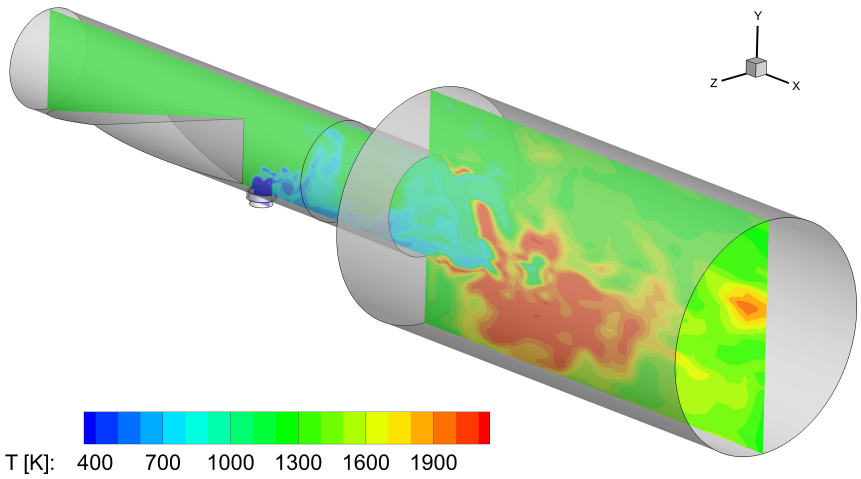

Figure 6.1: Location of central symmetry plane in technical premix setup with snapshot of temperature distribution

6.1 General flame description

Despite the relatively short recording time series, time-averaged distributions are presented first in order to describe the flow pattern in the test case. Distributions of flow variables are given for the central cut plane shown in Fig. 6.1, and also in two cross-sections before and behind the area expansion.

The heat release distribution in the central plane is shown in Fig. 6.2. The distribution is relatively homogeneous, even though one reckons that the recording time is insufficient for obtaining a smooth average. Indeed, when looking at time animations, the flame moves a lot, especially due to the consecutive appearance of ignition kernels similar to those observed in academic testcases, see e.g. Markides and Mastorakos [69]. Nevertheless, these distributions allow some qualitative observations. Firstly, the lower half contains most of the reaction due to a strong mixture stratification. This clearly appears from the distribution of the mean fuel mixture fraction given in Fig. 6.3. Furthermore, the auto-ignition zone is located quite far upstream and a local maximum of the reaction rate is observed in the lower shear layer close to the burner exit ; this suggests that intense flame wrinkling happens at this point, as it does for the perfect premix case.

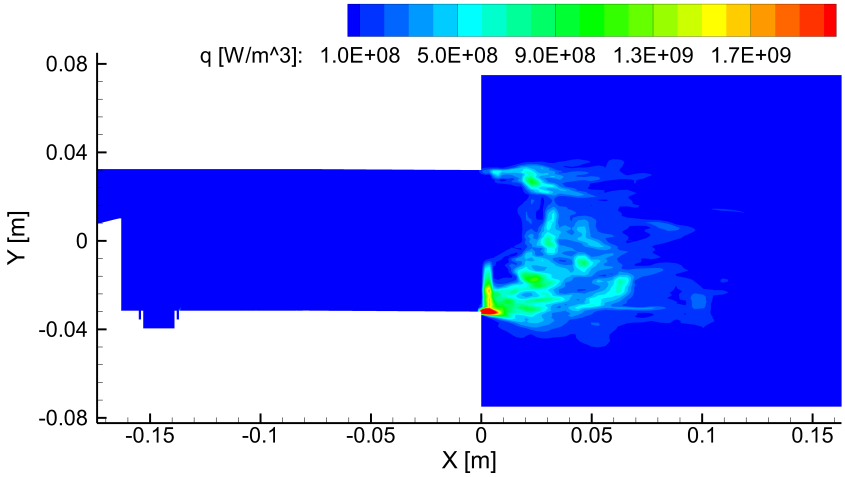

Figure 6.2: Mean distribution of volumetric heat release rate in central symmetry plane

In the upper combustor half, the auto-ignition zone lies further downstream; this is due to higher axial velocities in this region, see Fig. 6.4. It further appears that the inhomogeneous mixture distribution leads to asymmetric corner recirculation zones and thus to a deviation of the jet toward the upper half. As in the lower half, some intense reaction is observed in the shear layer.

The strong stratification of the mixture indicates that the operating parameters for the investigated setup are not ideal. At this point, the reader should be reminded that the setup corresponds to an intermediate development status of an experimental test rig, for which no extensive experimental data are available. These results clearly indicate that for future investigations the oper-

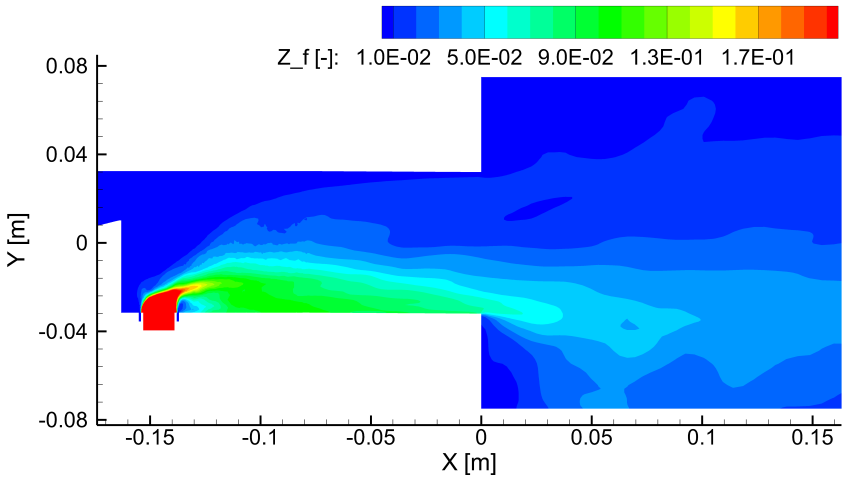

Figure 6.3: Mean distribution of fuel mixture fraction in central symmetry plane

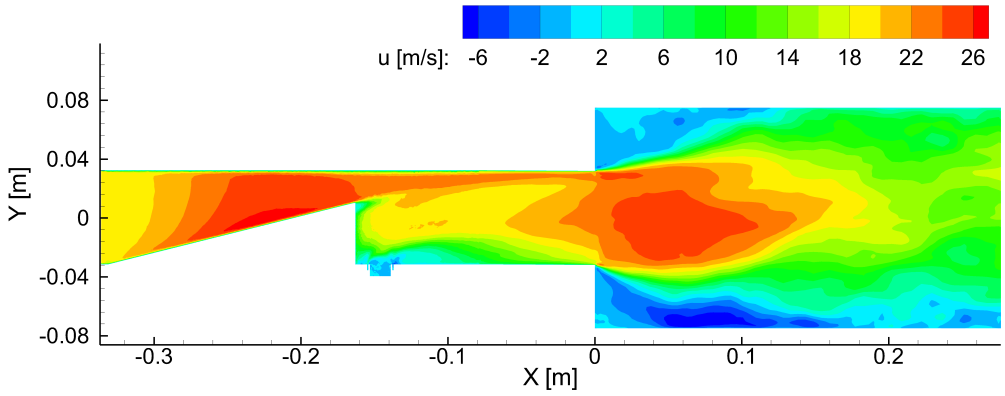

Figure 6.4: Mean distribution of axial velocity in central symmetry plane

ating point should be reviewed in order to obtain a more homogeneous mixing, which is more representative of industrial configurations.

Nevertheless, the simulations allow to get a better understanding of the mixing process in this complex flow field. Therefore, the velocity and mixing distributions are studied in a crossplane located at a position x=-0.1 m, i.e. 10 cm upstream of the area expansion. The contours are shown in Fig. 6.5. The helical vortex structure induced by the delta wing becomes apparent, inducing two parallel helices stretching in axial direction. The maximum of velocity component v in vertical direction (y-axis) is intended to suck the fuel into the hot gas stream. However, in the present case, this is not achieved properly, since only a small portion of the fuel penetrates far into the hot gas stream, while most of it accumulates close to the burner walls (see the mixture distribution on the lower right of Fig. 6.5).

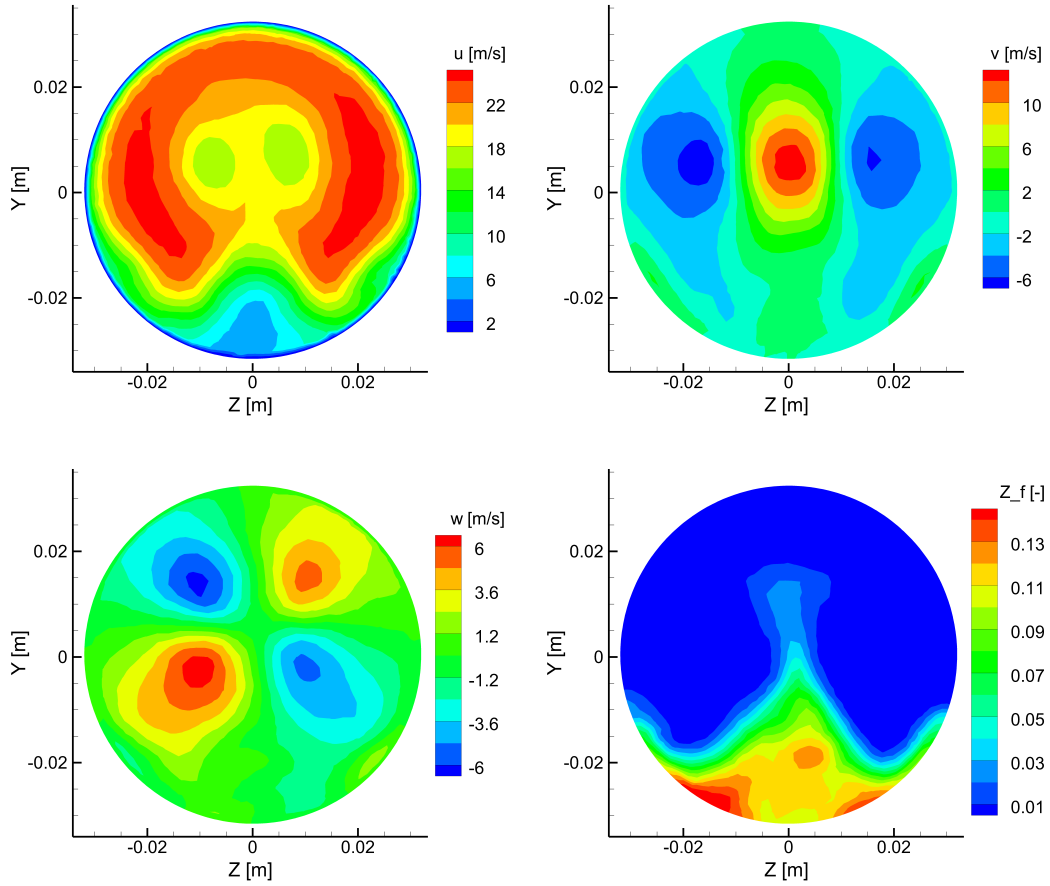

Figure 6.5: Mean distributions of velocity components and fuel mixture fraction in cross-plane located 10 cm upstream of the area expansion

Further downstream, the mixture stratification is also observed in a cross-plane through the combustion chamber shown in Fig. 6.6. Most of the fuel is located on the bottom, and moreover the stratification is slightly twisted in circumferential direction. This is due to the insufficient initiation run time; especially the recirculation zones are not fully developed. This insufficiency has one main drawback for the assessment of the flame dynamics, since the first transverse mode is also slightly twisted, as can be seen in the rms distribution of the acoustic pressure shown in Fig. 6.6. Nevertheless, in the central cut plane (z=0) used for the assessment of the flame dynamics, a clear transverse mode structure still appears. In any case, for a thorough quantitative assessment, a three-dimensional postprocessing should be used when dealing with such a complex flow field and flame shape.

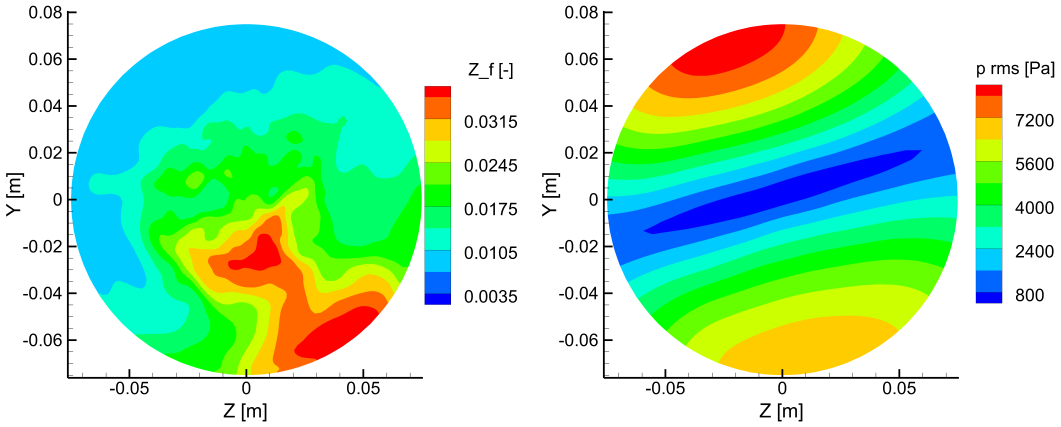

Figure 6.6: Mean distribution of fuel mixture fraction in crossplane (left) and resulting rms pressure distribution of 1T acoustic mode (right) in crossplane located 10 cm downstream of the area expansion

6.2 Analysis of flame dynamics

The filter-based postprocessing tools are also employed for this test case in order to obtain at least a qualitative description of the flame dynamics. Results will first be shown for a simulation without pressure sensitivity. The rms distribution of the heat release rate fluctuations is given in Fig. 6.7. It is similar to the mean distribution, although the maximum close to the lower burner lip is even more pronounced for the fluctuations.

Figure 6.8 shows the corresponding weighted phase plot distribution and indicates a continuously changing rainbow pattern of the phase at this position. It is thus confirmed that coherent flame wrinkling appears in this region; periodic flame wrinkles are as well observed when looking at time animations. In contrary to the perfect premix case, the flame wrinkles dissipate very quickly. In other parts of the flame, it is extremely difficult to distinguish a clear pattern of the phase.

The impact of inhomogeneous mixing is of particular interest for the present test case. Fig. 6.9 shows the instantaneous, filtered distributions of the fuel mixture fraction in the plane. Fluctuations occur both in the burner and the combustion chamber. However, these are not directly linked to each other. As mentioned, a strong mixture stratification exists in the combustion chamber. When subjected to a periodical acoustic displacement, it yields the observed

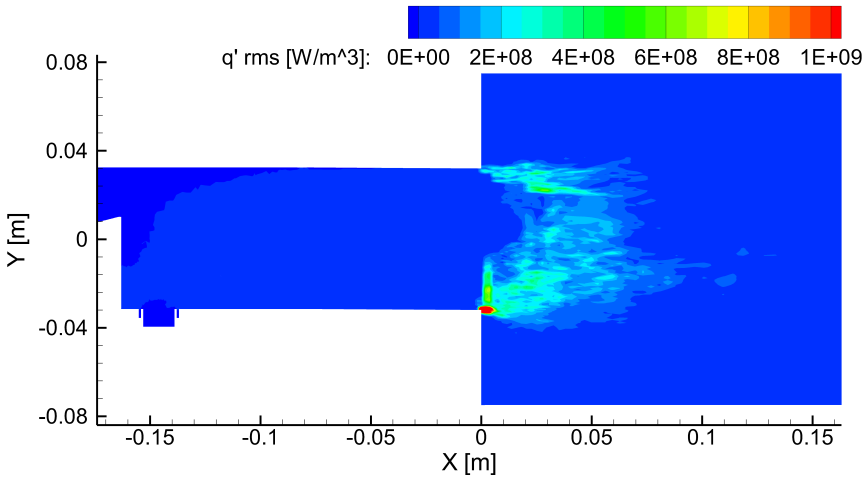

Figure 6.7: rms distribution of heat release rate fluctuations at 3000 Hz in central symmetry plane

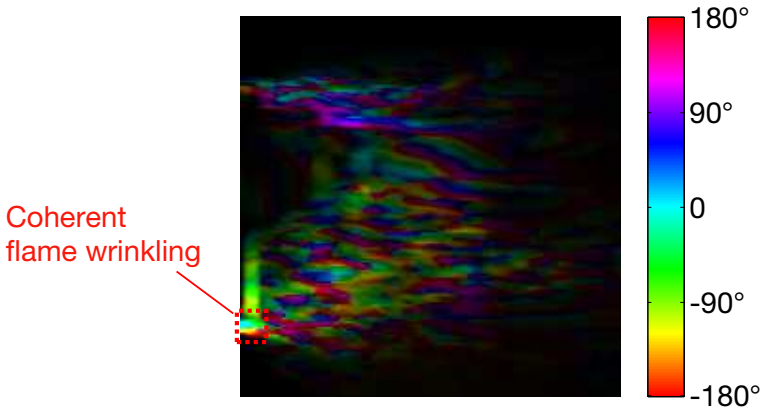

Figure 6.8: Phase lag distribution of heat release rate with respect to pressure at 3000 Hz

mixture fluctuations in the flame region. Consequently, when looking at the instantaneous fluctuations a quarter period later, mixture perturbations can no longer be observed in the combustion chamber. Therefore, these fluctuations do not cause a proper mixing-related thermoacoustic feedback. Instead it can be expected that the feedback linked to the acoustic displacement will again play a notable role.

The mixture fluctuations observed in the burner are caused by perturbations of the fuel injection. The latter occur, since the 1T mode generates weak fluctuations of axial velocity in the burner, which interact with the cross-flow injection. This leads to the mentioned mixture fluctuations in the burner. It also appears from Fig. 6.9 that these fluctuations are dissipated by turbulent diffusion before reaching the flame. Hence, it follows that no feedback related

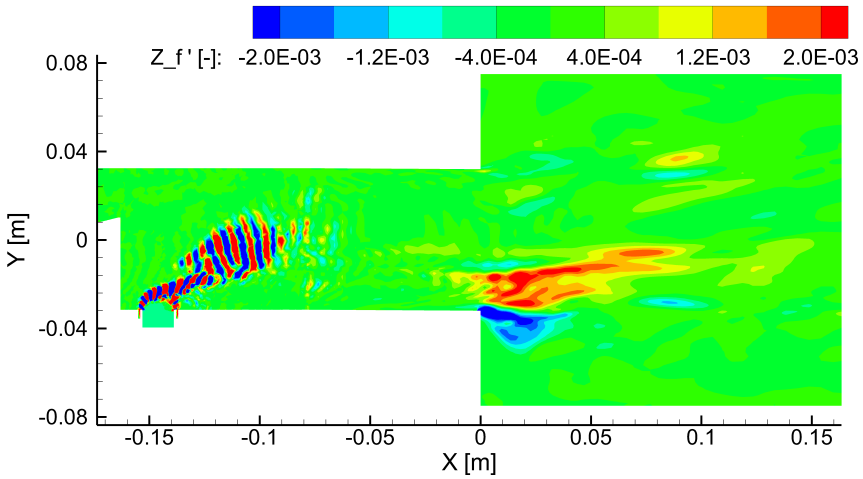

Figure 6.9: Instantaneous distribution of fuel mixture fraction fluctuations at 3000 Hz in central symmetry plane

to fuel mixture fluctuations occurs in the present case. It shall be noted that constant mass-flow boundary conditions were used for the fuel and carrier air inlets. Boundary conditions with differing impedance values might lead to stronger perturbations of the injection process. Furthermore, mixed modes with additional longitudinal components might as well induce mixture fluctuations with larger amplitudes, which might not dissipate before the flame front. The investigation of such alternative scenarios is, however, outside the scope of the present work.

From the analysis made, it follows that the flame dynamics is similar in the technical premix and in the perfect premix case. The flame is affected by transverse acoustic displacement, as well as by coherent wrinkling in the shear layers. However, the latter is observed only very close to the burner exit under technical premix conditions.

The planar distribution of the Rayleigh index is given in Fig. 6.10. As for the premix case, the inner and outer side of each shear layer yields negative and positive values, respectively. In addition, locally high values of the Rayleigh index are observed in the auto-ignition zone as well, and are supposed to be due to the interplay of the acoustic displacement and the non-constant mixture distribution. From the previous explanations, it follows that a local analysis at the cell scale is not sufficient for getting a clear understanding of the mechanisms involved. The corresponding axial distribution of the Rayleigh index is shown in Fig. 6.11. The profile is relatively smooth on the downstream end,

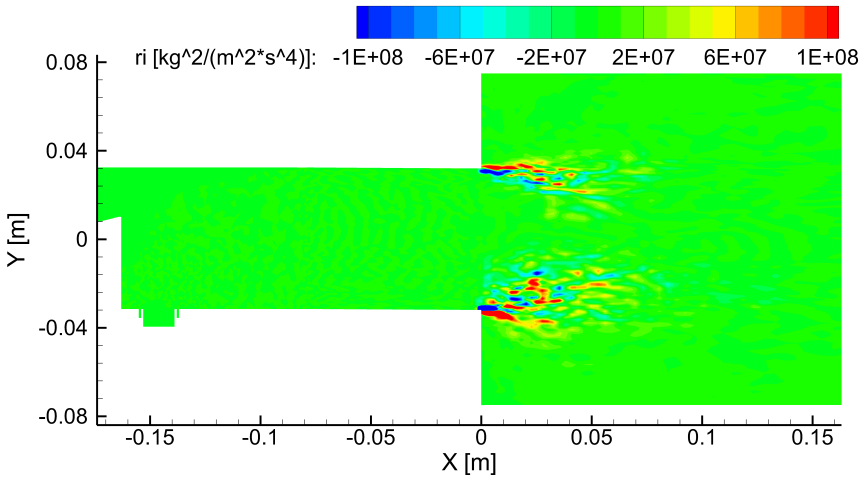

Figure 6.10: Rayleigh index distribution at 3000 Hz in central symmetry plane

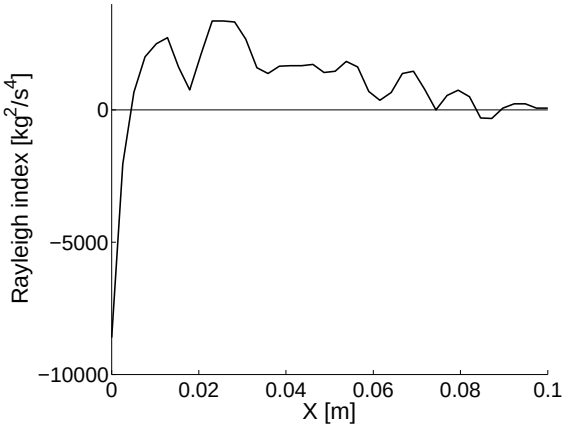

Figure 6.11: Axial distributions of Rayleigh index for technical premix case

while it shows a distinct negative peak close to the burner exit. The latter was also observed for the perfect premix case and proved to be due to the coherent flame wrinkling at the burner lip. However, the wrinkles dissipate very quickly here; an alternation of positive and negative peaks is thus not observed.

Results are also given for calculations with consideration of pressure sensitivity. Analogously to the perfect premix case, a constant value of $\varphi_p = 5$ was applied. The resulting Rayleigh index distribution in the central plane is given in Fig. 6.12 and indicates again a relative increase in positive feedback regions. The axial evolution of Fig. 6.13 consequently also shows a characteristic minimum at the burner lip followed by a relatively smooth profile, with the latter being shifted toward positive values in comparison to Fig. 6.11.

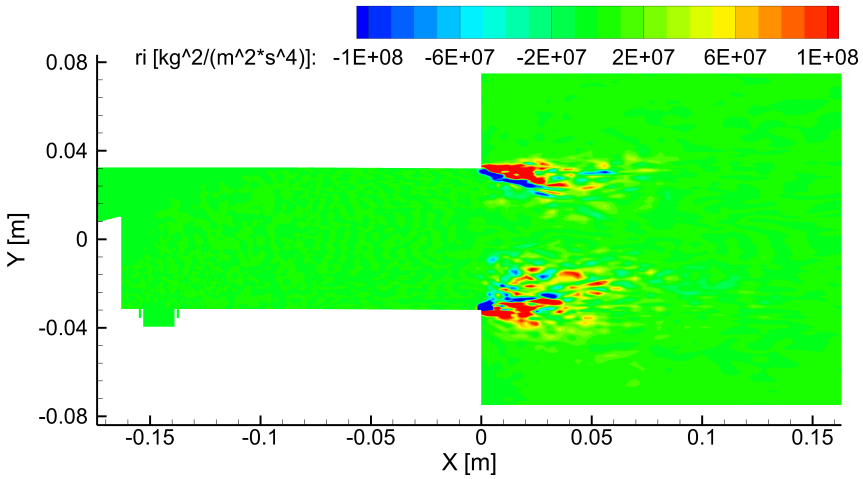

Figure 6.12: Rayleigh index distribution at 3000 Hz in central symmetry plane with pressure sensitivity

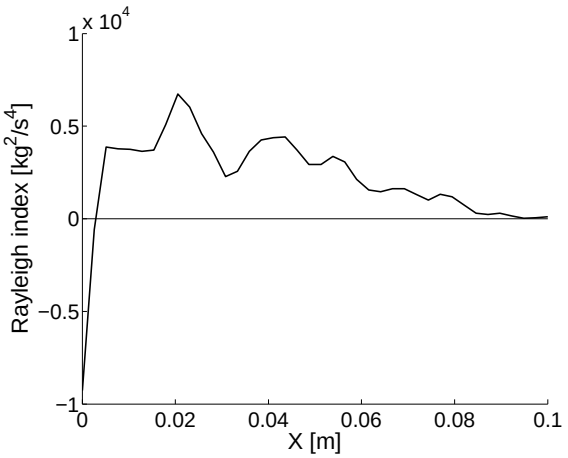

Figure 6.13: Axial distributions of Rayleigh index for technical premix case

It is not possible to proceed to a detailed decomposition of the thermoacoustic feedback contributions as for the first test case. In order to so, modelling tools are required; they are introduced in the next chapter. They are employed to estimate some of the feedback contributions mentioned and tested whether they allow to make an acceptable guess of the overall Rayleigh index.

Hence, one can conclude that despite the huge compromises needed for reducing the computational effort, a qualitative observation of flame dynamics could be done, which yielded a very similar behaviour as for the perfect premix test case. For more reliable results, the configuration should be reviewed in several aspects:

- Modify the operating conditions in order to obtain better mixing conditions, and hence a more realistic flame shape,
- Increase the length of the initiation run as well as of the recording period,
- Include turbulence-chemistry interaction modelling by using more than one stochastic field.

7 Thermoacoustic Feedback Related to High-Frequency Transverse Instabilities

7.1 Synthesis on observed feedback mechanisms

It follows from the previous chapters that similar flame response mechanisms appear for perfectly as well as for technically premixed flames. These can be categorised into two different kinds:

1. Inherent contributions: acoustic displacement, density, and pressure sensitivity. These contributions always appear and can be predicted from the mean flame shape and the acoustic mode structure. The corresponding feedback is always positive for the density; the same applies to the pressure sensitivity at high frequencies and to the acoustic displacement provided that the flame brush is thin in direction of the acoustic mode. For homogeneous reaction zones, like the auto-ignition zone in the perfect premix case, the feedback linked to acoustic displacement is typically rather low. Under certain circumstances, this contribution can also become negative, depending on the distribution of the mean heat release rate. The impact of these inherent contributions can only be influenced by modifying the mean flame shape, either by modifying its position with respect to the acoustic mode or by generating homogeneous reaction zones, thus minimising the acoustic displacement feedback.

2. Variable contributions: residual displacement and consumption rate (incl. equivalence ratio and flame surface modulations). Their effect will depend on the case setup and the excitation frequency, and can be of dampening or amplifying character. A beforehand prediction is difficult, as it strongly depends on the vortex roll-up and flame wrinkling as well as on the fuel injection. Nevertheless, this offers the possibility to reduce the global source term by design means, e.g. by influencing the vortex formation and the flame wrinkling at the burner exit.

An important observation could be made regarding the feedback linked to equivalence ratio fluctuations: The analysis of the technical premix case showed that it is unlikely that purely transverse modes within the combustion chamber are amplified by mixture fluctuations. However, it should be noted that this might not hold true for mixed modes with longitudinal components, as the latter generally induce larger equivalence ratio fluctuations at the injection, which might not be equilibrated before the flame front and thus lead to fluctuations of the heat release rate.

In industrial practice, it is of high interest to know which contributions are mainly responsible for the thermoacoustic feedback of the flame. A detailed decomposition was made for the shear layer combustion in chapter 5, but cannot be applied to more complex cases. To this end, flame transfer function formulations are proposed in the following that allow to model the inherent contributions and hence to quantify the corresponding thermoacoustic feedback.

7.2 Feedback modelling for inherent contributions

7.2.1 Formulation of flame transfer functions

Flame transfer functions describe the link between normalised fluctuations of heat release rate and acoustic velocity or pressure. As a consequence, with a modelled flame transfer function the thermoacoustic feedback can be predicted quantitatively from mean heat release rate distributions and acoustic mode shapes.

The following non-compact flame transfer function distributions are therefore proposed for the inherent feedback contributions linked to density, acoustic displacement, and pressure sensitivity, see also Zellhuber and Polifke [125]. Building up on the previous chapters, they can be formulated as follows for harmonic fluctuations:

- Density:

$$\left.\frac{\dot{q}'(\vec{x},t)}{\bar{\dot{q}}}\right|_{\rho} = \frac{1}{\gamma}\frac{p'(\vec{x},t)}{\bar{p}(\vec{x})} \tag{7.1}$$

- Acoustic displacement

$$\left.\frac{\dot{q}'(\vec{x},t)}{\bar{\dot{q}}(\vec{x})}\right|_{\Delta,ac} = -\frac{\vec{\Delta}_{ac}(\vec{x},t)\cdot\vec{\nabla}\bar{\dot{q}}(\vec{x})}{\bar{\dot{q}}(\vec{x})}$$

with $\vec{\Delta}_{ac}(\vec{x},t) = \int \vec{u}'(\vec{x},t)\,dt = \Re\left(\frac{1}{i\omega}\breve{\vec{u}}(\vec{x},t)\right)$, what finally yields:

$$\left.\frac{\dot{q}'(\vec{x},t)}{\bar{\dot{q}}(\vec{x})}\right|_{\Delta,ac} = \Re\left(-\frac{1}{i\omega}\frac{\breve{\vec{u}}(\vec{x},t)\cdot\vec{\nabla}\bar{\dot{q}}(\vec{x})}{\bar{\dot{q}}(\vec{x})}\right) \tag{7.2}$$

- Pressure sensitivity:

$$\left.\frac{\dot{q}'(\vec{x},t)}{\bar{\dot{q}}(\vec{x})}\right|_{\varphi_p} = \varphi_p\frac{p'(\vec{x},t)}{\bar{p}(\vec{x})} \tag{7.3}$$

One may notice that the term related to the pressure sensitivity is simplified similarly to Eq. (4.58). More exactly, the convectively transported, time-delaying term is omitted. It was shown in chapter 4 that under realistic conditions this term is small at higher frequencies.

From the transfer functions one can calculate corresponding Rayleigh index values

$$\mathrm{RI}_{\rho,mod} = \iiint\int_0^{\mathcal{T}} p'(\vec{x},t)\bar{\dot{q}}(\vec{x})\frac{1}{\gamma}\frac{p'(\vec{x},t)}{\bar{p}(\vec{x})}dt\,d\vec{x} \tag{7.4}$$

$$\mathrm{RI}_{\Delta,mod} = \iiint\int_0^{\mathcal{T}} p'(\vec{x},t)\bar{\dot{q}}(\vec{x})\Re\left(-\frac{1}{i\omega}\frac{\breve{\vec{u}}(\vec{x},t)\cdot\vec{\nabla}\bar{\dot{q}}(\vec{x})}{\bar{\dot{q}}(\vec{x})}\right)dt\,d\vec{x} \tag{7.5}$$

$$\mathrm{RI}_{\varphi_p,mod} = \iiint\int_0^{\mathcal{T}} p'(\vec{x},t)\bar{\dot{q}}(\vec{x})\varphi_p\frac{p'(\vec{x},t)}{\bar{p}(\vec{x})}dt\,d\vec{x}, \tag{7.6}$$

which can be summed up to a total modelled Rayleigh index for the inherent contributions $\mathrm{RI}_{inh,mod}$:

$$\mathrm{RI}_{inh,mod} = \mathrm{RI}_{\varphi_p,mod} + \mathrm{RI}_{\rho,mod} + \mathrm{RI}_{\Delta,mod} \tag{7.7}$$

$$\begin{aligned}\mathrm{RI}_{inh,mod} = \iiint\int_0^{\mathcal{T}} & p'(\vec{x},t)\bar{\dot{q}}(\vec{x}) \\ & \cdot\left[\left(\varphi_p+\frac{1}{\gamma}\right)\frac{p'(\vec{x},t)}{\bar{p}(\vec{x})} - \Re\left(\frac{1}{i\omega}\frac{\breve{\vec{u}}(\vec{x},t)\cdot\vec{\nabla}\bar{\dot{q}}(\vec{x})}{\bar{\dot{q}}(\vec{x})}\right)\right]dt\,d\vec{x}.\end{aligned} \tag{7.8}$$

This equation will be applied to the results of both test cases and compared to the direct computation of the Rayleigh index. For the variable feedback contributions, it is not possible to provide such a general quantitative description, they have to be determined by simulation or measurement for a given configuration.

7.2.2 Application to LES test cases

7.2.2.1 Application to perfect premix case

The applicability of Eqs. (7.1) to (7.8) is therefore first tested on the 1T and 2T excitation of the perfect premix case, with and without pressure sensitivity.

A reference Rayleigh index evolution is calculated using the filtered time series of pressure and heat release rate, as done before. The observation plane is again separated into individual layers, distributed in axial (as e.g. in Fig. 5.12 on the right) and additionally in transverse direction. The inherent contributions to the feedback are modelled, using only acoustic velocity and pressure data as well as the mean heat release rate distributions. Pressure sensitivity values ($\varphi_p = 0$ or 5) are used according to the considered simulation setup.

A comparison between the reference value and the modelled sum of the inherent contributions – see Figs. 7.1 to 7.4 – allows to draw a number of conclusions. First of all, the relative importance of the inherent contributions to the total thermoacoustic source term can be assessed. Moreover, by comparing the results with and without pressure sensitivity, one can estimate the error made by using the simplified transfer function of Eq. 7.3. Lastly, the distributions shown in the following allow to gain a physical understanding of the interplay between the different feedback contributions even for complex configurations such as the technical premix case.

1T excitation of perfect premix test case The axial and transverse Rayleigh index evolutions in the perfect premix, 1T excitation case are shown in Figs. 7.1 and 7.2 for both values of pressure sensitivity. One can conclude that the proposed flame transfer functions allow good predictions of the thermoacoustic feedback profile, in particular in the downstream parts. Notable differences appear only in the upstream region, where the coherent flame wrinkling

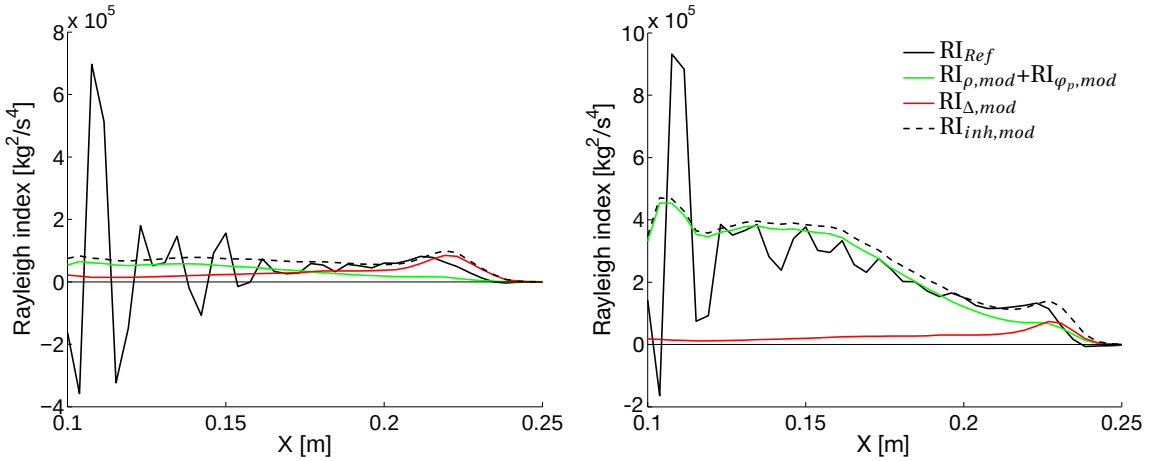

Figure 7.1: Comparison of reference and modelled axial Rayleigh index distributions for 1T excitation case – left: φ_p=0, right: φ_p=5

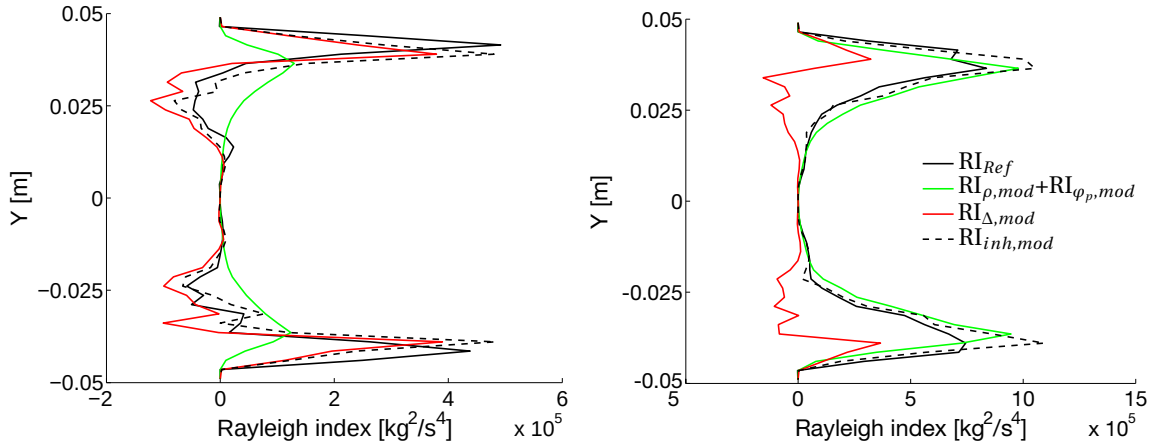

Figure 7.2: Comparison of reference and modelled transverse Rayleigh index distributions for 1T excitation case – left: φ_p=0, right: φ_p=5

contributes significantly to the source term. This appears as well in the transverse profiles, which show the strongest deviations between inherent and reference Rayleigh index in the shear layer regions.

In chapter 5, the contribution linked to the consumption rate was found to be slightly negative when integrated over the entire shear layer. This is in accordance with the results of the modelling, since the total sum of inherent contributions overpredicts the Rayleigh index by 45.5% and 19.1% for the cases without and with pressure sensitivity, respectively. The simplification made

for the pressure sensitivity contribution appears to be justified, as a similar modelling quality are obtained for both values of φ_p.

It can be noted from the transverse profiles that locally the contribution of the acoustic displacement can be negative. That is due to the dependence of this contribution on the gradient of the mean heat release rate. However, as shown in section 2.3.2, the integral over the thin flame yields a positive value, explaining the overall positive values that are observed in the axial profiles.

2T excitation of perfect premix test case The comparison between reference and modelled Rayleigh index is shown for the 2T excitation case in Figs. 7.3 and 7.4, in axial and transverse directions respectively. Looking at the transverse plots, it clearly appears that the auto-ignition zone contributes to the flame feedback, as pointed out in chapter 5.

For the case without pressure sensitivity, the flame transfer function modelling does not allow a satisfying estimation of the flame feedback, which is overestimated by 137%. This can be seen in the axial distribution plot. In section 5.5.2, it was mentioned that for the 2T excitation case the feedback contribution $\mathrm{RI}_{\dot{\omega}}$ was constantly shifted toward negative values. It is supposed that this shift is causing the overestimations by the flame transfer functions. As noted before, this shift is not understood at present, as it does not have any clear physical explanation. In addition, the low absolute fluctuation values, in particular in the downstream part, might also affect the postprocessing quality and explain partly the discrepancies observed.

When including the pressure sensitivity, this discrepancy appears to be rather insignificant: A deviation of only 11.6% is observed in this case. It follows from both axial and transverse distributions that the pressure sensitivity is the dominant thermoacoustic feedback mechanism, which is well described by the flame transfer function introduced earlier, i.e. by Eq. (7.3).

7.2.2.2 Application to technical premix case

The analysis made in chapter 6 underlined that the technical premix flame is rather irregular. In the following it will be shown that, in spite of this complexity, the presented flame transfer functions allow fairly good predictions of the

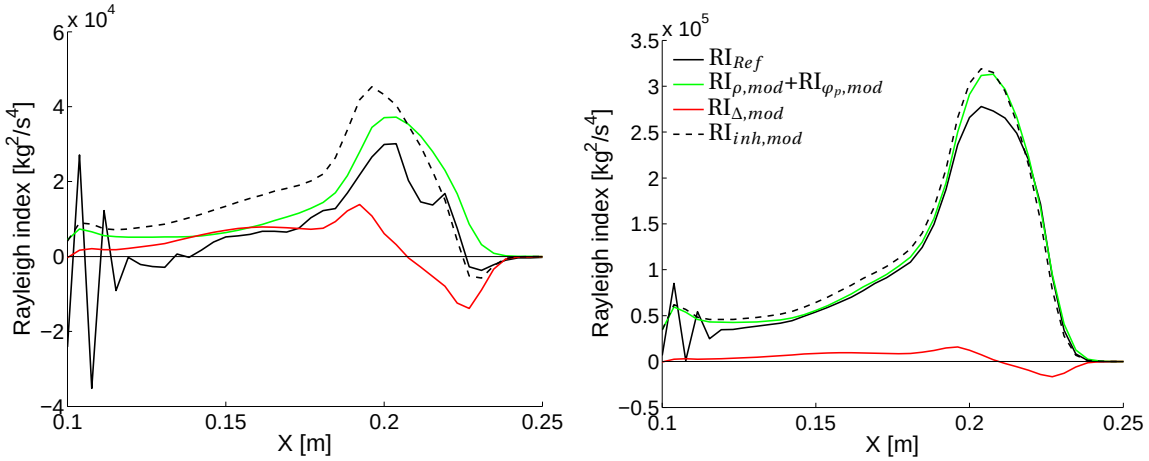

Figure 7.3: Comparison of reference and modelled axial Rayleigh index distributions for 2T excitation case – left: φ_p=0, right: φ_p=5

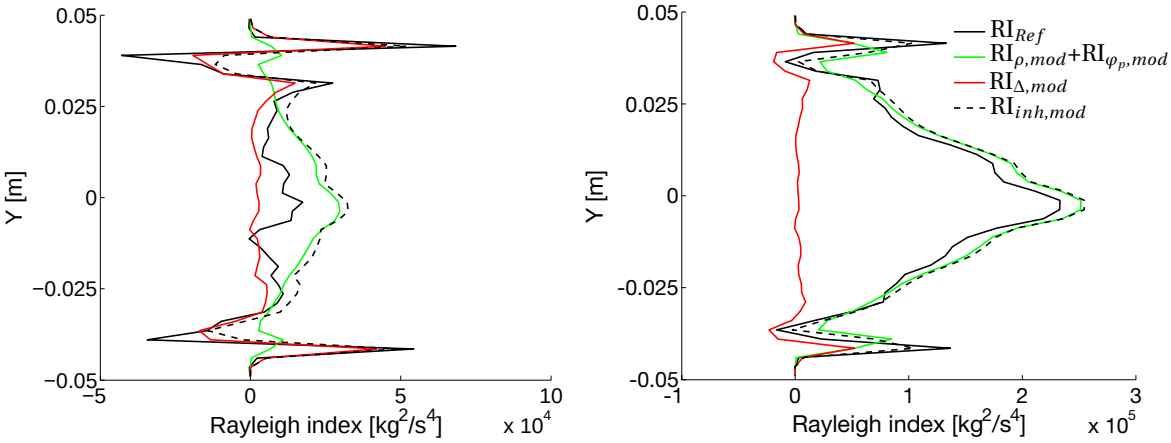

Figure 7.4: Comparison of reference and modelled transverse Rayleigh index distributions for 2T excitation case – left: φ_p=0, right: φ_p=5

flame response and moreover, allows to dismantle the total flame response into individual contributions.

Therefore, as for the perfect premix case, the modelled inherent and the reference Rayleigh index are calculated in axial and transverse layers and are plotted in Figs. 7.5 and 7.6. Results are again shown for two simulation runs, without and with pressure sensitivity.

For the case without sensitivity, the transverse evolution of the reference Rayleigh index is satisfactorily predicted by the model for the inherent contributions. The stratification of the mixture is clearly present in the trans-

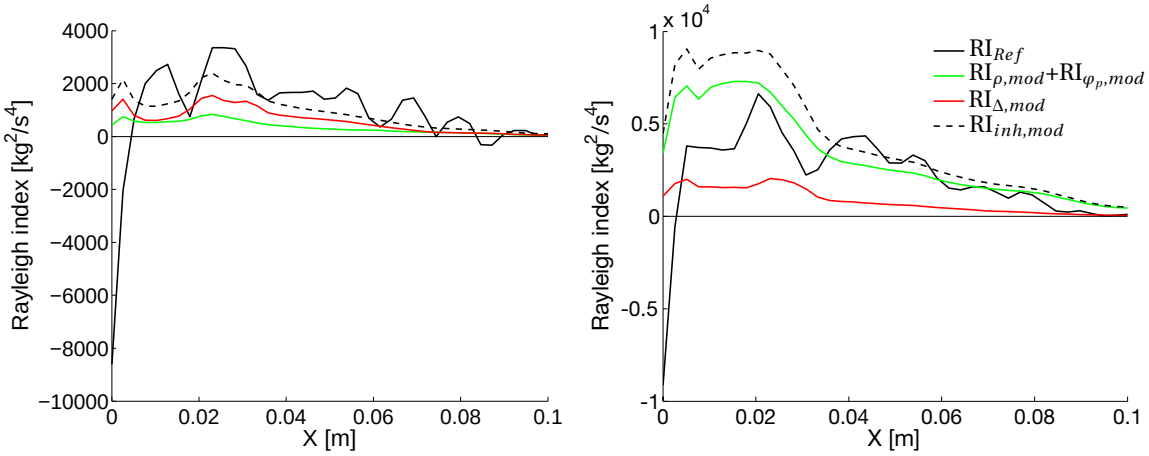

Figure 7.5: Comparison of reference and modelled axial Rayleigh index distributions for technical premix case – left: φ_p=0, right: φ_p=5

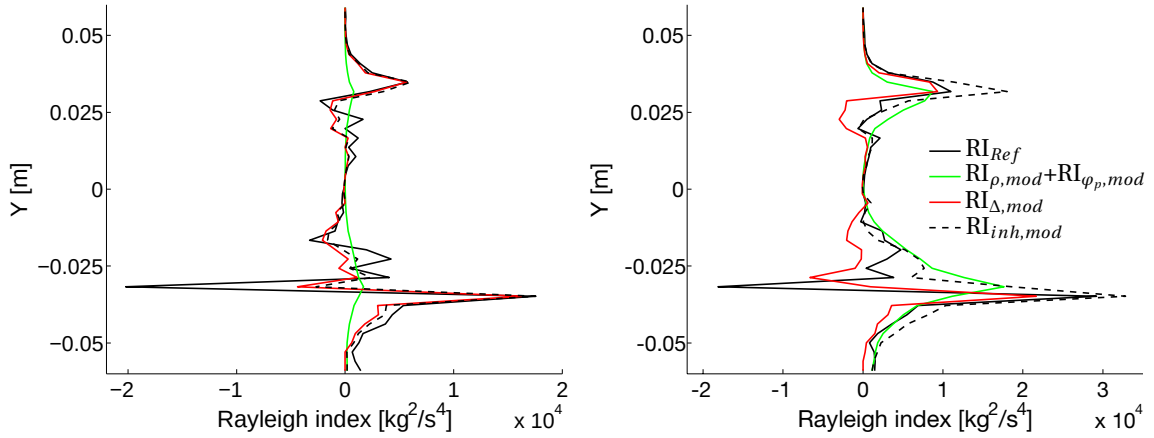

Figure 7.6: Comparison of reference and modelled transverse Rayleigh index distributions for technical premix case – left: φ_p=0, right: φ_p=5

verse feedback profile, since it is asymmetric with higher absolute values in the lower combustor half.

In the transverse plot, largest deviations are found again in the shear layers, especially in the lower; it is supposed to be linked to the coherent flame wrinkling observed in the phase plot of Fig. 6.8. Indeed, in the axial evolution plot, a strong negative value is found for the Rayleigh index close to the burner exit. This minimum is not captured by the modelling, what supports the hypothesis about the impact of flame wrinkling. Summed up over the entire flame,

the modelling of inherent contributions overestimates the reference Rayleigh index by only 6.0% for the case without pressure sensitivity.

As shown in chapter 6, the addition of the pressure sensitivity strengthens the feedback. However, in comparison to the perfect premix case, its influence is less pronounced. The contribution of the acoustic displacement is relatively strong and thus has to be retained. It can be noted that for the case with pressure sensitivity the modelling leads to a significant overestimation of the flame feedback by 88.0%. These deviations appear in both axial and transverse profiles. Especially in the upstream flame region, the modelled flame transfer function does not deliver satisfactory predictions. From the transverse profile, it appears that, in addition to an overestimation made in the shear layers, the feedback in the lower part of the auto-ignition zone is as well overestimated.

It is not possible to develop a detailed understanding of these deviations from the available LES data. This aspect has to be addressed in future work, mainly by investigating operating points leading to a flame located further downstream with less variations in flame position. In any case, as mentioned in chapter 6, the shortcomings of the technical premix LES runs have to be amended in order to obtain more reliable quantitative results. Nevertheless, the application of the modelled flame transfer functions is promising, since the global evolution of the feedback profiles can be reproduced despite the complex flame shape, in particular for the case without pressure sensitivity.

7.2.3 Growth rate calculations from modelled Rayleigh-index

The flame transfer functions introduced in the previous section allow to obtain a fair estimation of the global thermoacoustic feedback. As shown by Schwing et al. [109] and Ibrahim et al. [48], the Rayleigh criterion can be converted to a growth rate contribution α_{FD} linked to flame dynamics:

$$\alpha_{FD} = \frac{1}{2\overline{E}_{ac}\mathcal{T}} \int_0^{\mathcal{T}} \frac{dE_{ac}}{dt} dt = \frac{1}{2\overline{E}_{ac}\mathcal{T}} \frac{\gamma - 1}{\gamma \overline{p}} \mathrm{RI} \tag{7.9}$$

with $E_{ac} = \int_V e_{ac} dV$ and $\overline{E}_{ac} = \frac{1}{\mathcal{T}} \int_0^{\mathcal{T}} E_{ac} dt$. From the growth rate, one can finally estimate the approximate damping level needed to balance the thermoacoustic energy production. This however needs to be performed on the entire three-dimensional domain, e.g. using acoustic field data gained from FEM.

For the simulations done in the present work, one can calculate growth rates on the basis of the symmetry cut plane data. For the perfect premix test case, this can even be regarded as an approximate value of the total growth rate, since the flame shape is quite regular, as seen in the Rayleigh distribution plots in the transverse monitor plane (Fig. 5.14). For the technical premix case, growth rate computations should at least take into account data gathered in several cut planes, and even better in the entire three-dimensional space. This can be viewed as a challenging task in terms of postprocessing and would be of interest for future work. Nonetheless, a growth rate is also calculated for the technical premix case, in order to get an indication of growth rate values.

The results are gathered in Tables 7.1 and 7.2 for the perfect and technical premix test cases, respectively. They are computed on the basis of $\mathrm{RI}_{inh,mod}$ defined in Eq. (7.8). Whether these values are truly representative needs to be examined in future work, even though the order of magnitude is rather typical of gas turbine combustors, see e.g. [109, 111].

	1T, $\varphi_p = 0$	1T, $\varphi_p = 5$	2T, $\varphi_p = 0$	2T, $\varphi_p = 5$
$\alpha_{FD}[1/s]$	99.0	425	110	678

Table 7.1: Quantification of thermoacoustic growth rate contributions in central symmetry plane for perfect premix case

	$\varphi_p = 0$	$\varphi_p = 5$
$\alpha_{FD}[1/s]$	56.4	193

Table 7.2: Quantification of thermoacoustic growth rate contributions in central symmetry plane for technical premix case

7.3 Exemplifying stability analysis with acoustic network

Using Eq. (7.9), one can calculate the thermoacoustic growth rate contributions. This is not sufficient for a stability analysis, as one needs to know the acoustic damping rate, which is governed by the hydrodynamics of the flow, acoustic boundary conditions (openings and walls), as well as by the temperature distribution in the setup. In industrial practice, stability prediction tools (see section 3.3) are used, which rely on flame transfer function formulations.

For doing a stability analysis of the presented test cases, one would use, for instance, Eqs. (7.1) to (7.3) in an FEM tool. The application in multidimensional FEM calculations lies outside the scope of the present work. Instead, the flame transfer functions are used by way of example in a 1D network model approach for a model configuration inspired by the premix test case. It is shown in Fig. 7.7 and features an area expansion. The flame consists of a horizontal flame propagation and a vertical auto-ignition zone. Only the stability of the first transverse mode is investigated. This allows to neglect the impact of the auto-ignition zone, since it was found to not cause a significant feedback for the 1T mode in the perfect premix case. With this simplification, the system can be represented by a one-dimensional network, with elements disposed in transverse direction. Because of the symmetry, only the upper combustor half is modelled, as indicated in Fig. 7.7 and shown more in detail in Fig. 7.8. The acoustic network representation comprises

1. a boundary condition (BC) representing the upper wall at position $y = H$,
2. one duct in the burnt mixture of length L_h,
3. a flame with heat release $\dot{Q}$ at a mean position $y = \bar{y}_f$,
4. one duct in the cold mixture of length L_c,
5. a boundary condition representing the burner axis at position $y = 0$.

Acoustic network structures with these elements are commonly used for the calculation of longitudinal mode stability. They ask for a flame transfer function to model the heat release fluctuations at the flame. Although such a network would allow to incorporate the feedback linked to density fluctuations and pressure sensitivity, it cannot account for the acoustic displacement. The latter proved to bring a significant contribution to the thermoacoustic feedback, but cannot be modelled when using a single flame element.

Therefore, the flame is discretised into N "flame slices" separated by duct elements, as indicated in Fig. 7.9, and assuming a Gaussian normal distribution of the mean heat release rate over the flame. The mean heat release rate in the slice of index i at a position y_i then reads as

$$\overline{\dot{q}}(y_i, t) = \frac{\overline{\dot{Q}}}{L_f\sqrt{2\pi}} \exp\left(-\frac{1}{2}\left(\frac{y_i - \overline{y}_f}{L_f}\right)^2\right) \tag{7.10}$$

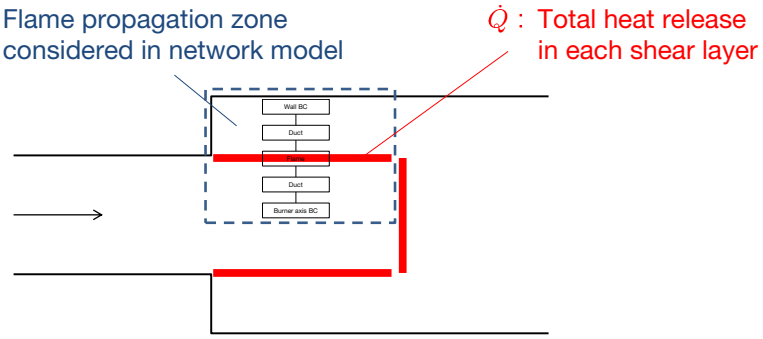

Figure 7.7: Sketch of configuration used for exemplifying stability analysis

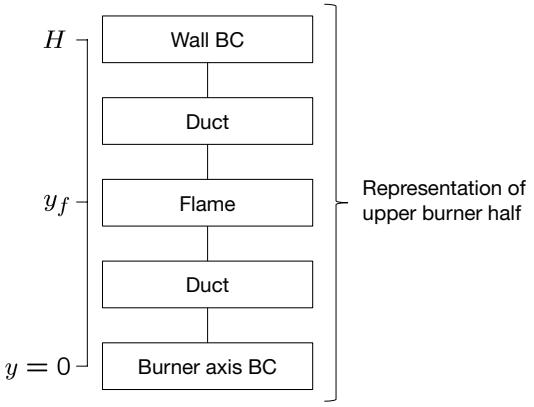

Figure 7.8: Sketch of configuration used for exemplary stability analysis

with L_f denoting the flame thickness, which is supposed to remain constant. The mean mixture temperatures before (index c - cold) and behind (index h - hot) each flame slice can be calculated from the assumed flame shape. The overall energy balance reads:

$$\overline{\rho}_c \overline{u}_c \frac{\gamma R}{\gamma - 1} (\overline{T}_{h,N} - \overline{T}_{c,1}) = \sum_{i=1}^{N} \frac{\overline{\dot{Q}}}{L_f \sqrt{2\pi}} \exp\left(-\frac{1}{2} \left(\frac{y_i - \overline{y}_f}{L_f} \right)^2 \right) (y_{i+1} - y_i), \tag{7.11}$$

and the local one:

$$\overline{\rho}_c \overline{u}_c \frac{\gamma R}{\gamma - 1} (\overline{T}_{h,i} - \overline{T}_{c,i}) = \frac{\overline{\dot{Q}}}{L_f \sqrt{2\pi}} \exp\left(-\frac{1}{2} \left(\frac{y_i - \overline{y}_f}{L_f} \right)^2 \right) (y_{i+1} - y_i). \tag{7.12}$$

Combining these equations, the local mean temperatures can be determined.

Analogously, when proceeding to a stability analysis using FEM, a sufficiently fine computational mesh has to be used in order to discretise the flame brush and capture the effect of acoustic displacement.

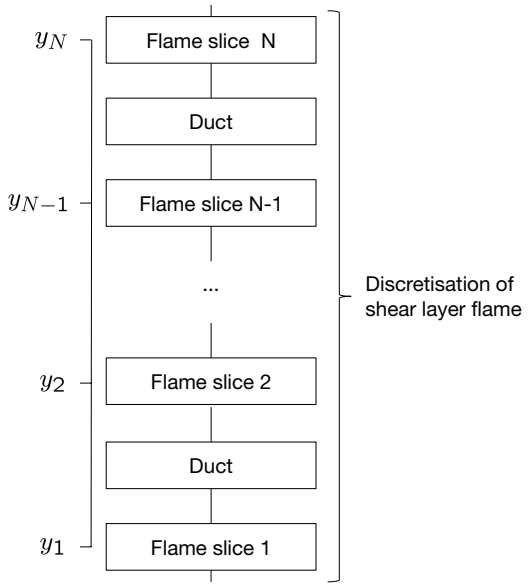

Figure 7.9: Sketch of flame discretisation

Then, one needs to insert the flame transfer functions. For the density and the pressure sensitivity, a direct proportionality to the local pressure is used as given by Eqs. (7.1) and (7.3). For the acoustic displacement, the local heat release rate fluctuations can be written as follows, after combining Eqs. (7.2) and (7.10) and introducing Riemann invariants f and g:

$$\breve{\dot{q}}_{\Delta,ac}(y_i,t) = \frac{1}{i\omega}\left[f(\overline{y}_f,t) - g(\overline{y}_f,t)\right]\frac{y_i-\overline{y}_f}{L_f^2}\frac{\overline{\dot{Q}}}{L_f\sqrt{2\pi}}\exp\left(-\frac{1}{2}\left(\frac{y_i-\overline{y}_f}{L_f}\right)^2\right). \tag{7.13}$$

It shall be noted that in the above equation a constant displacement is modelled over the flame front, depending on the acoustic velocity at the flame center $\overline{y}_f$. This is consistent with the assumption of a constant flame thickness. This simplification might not hold true anymore when the flame is located close to a pressure antinode. Indeed, strong spatial gradients of acoustic velocity exist at these locations; hence, the straightforward application of Eq. (7.2) will predict a stretching or a narrowing of the flame brush. Whether this actually happens, depends on the other hand on the total mass-specific fluctuations of the consumption rate. Hence, in the present work, averaged values of the displacement are considered, analogously to the post-processing made in chapter 5; possible stretching/narrowing effects are not considered further. However, this should be looked more closely at, in particular when considering wall-near combustion like in rocket engines.

In a network model, the discretisation of the flame leads to a relatively large system matrix, with N flames and $N-1$ infinitesimal ducts connecting the flames with each other. It is very convenient to use an odd number of flames, such that the flame with index $m = (N+1)/2$ represents the overall flame center. The system matrix can then be completed by applying the Rankine-Hugoniot relations at each flame, taking into account the local heat release rate fluctuations.

The Rankine-Hugoniot relations for the Riemann invariants before and behind each flame i finally can be written as follows:

$$\varsigma_i f_{h,i} + \varsigma_i g_{h,i} = f_{c,i} + g_{c,i} - \left(\frac{\overline{T}_{h,i}}{\overline{T}_{c,i}} - 1\right) M_{c,i} \cdot \left[f_{c,i} - g_{c,i} + \frac{\overline{v}_c (f_{c,m} - g_{c,m})(x_i - \bar{y}_f)}{i\omega L_f^2} + \left(1 + \varphi_p M_{c,i} \gamma\right)\left(f_{c,i} + g_{c,i}\right) \right] \tag{7.14}$$

$$f_{h,i} - g_{h,i} = f_{c,i} - g_{c,i} + \left(\frac{\overline{T}_{h,i}}{\overline{T}_{c,i}} - 1\right) \cdot \left[\left(\varphi_p + \frac{1}{\gamma} - 1\right) \gamma M_{c,i} (f_{c,i} + g_{c,i}) + \frac{\overline{v}_c (f_{c,m} - g_{c,m})(y_i - \bar{y}_f)}{i\omega L_f^2} \right] \tag{7.15}$$

with $\varsigma_i = \frac{\overline{\rho}_{h,i} \overline{a}_{h,i}}{\overline{\rho}_{c,i} \overline{a}_{c,i}}$.

At the hot end, i.e. at the combustor wall, a velocity node ($v' = 0$) is applied; the cold end, i.e. the burner axis, is represented by a pressure node ($p' = 0$). The latter is representative of the 1T mode only. For a 2T mode one ought to use a velocity node at the axis.

The results of the network analysis are shown in Fig. 7.10 in terms of growth rates, for varying values of the flame position $\bar{y}_f$. Here, the variation of the flame position is equivalent to a change in area expansion ratio. Largest growth rates appear in a medium range when the superposition of pressure and velocity dependent flame response mechanisms is the strongest. For this simple model configuration one can estimate for instance an approximate damping need of 130 s^{-1} for the 1T mode. Fig. 7.10 further indicates that the design impact on inherent contributions is rather limited, unless one goes to unrealistically high area expansion ratios, i.e. to low values of $\overline{y}_f$.

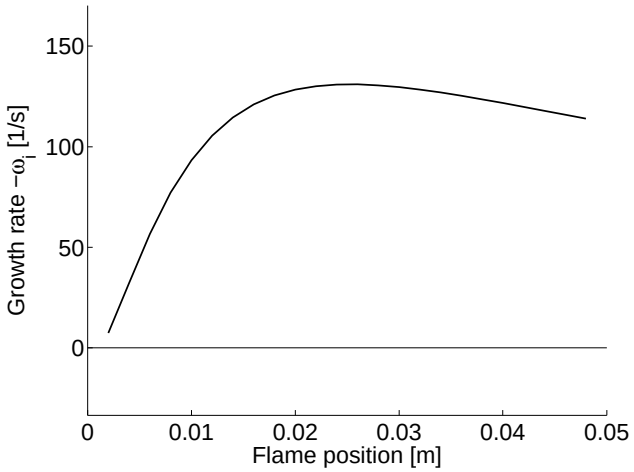

Figure 7.10: Impact of vertical flame position on 1T mode stability.

7.4 Outlook on high-frequency stability design

The quantitative description of the inherent feedback contributions is of high interest for gas turbine combustor design, as it allows two main conclusions. Firstly, one can obtain a good estimate of the level of damping needed for ensuring stable operation. With this knowledge, the layout of passive damping devices can be incorporated at a very early stage into the design process, as target damping levels can be estimated from a single CFD calculation (to get the mean flame shape) in addition to a FEM calculation delivering the acoustic mode shapes of pressure and velocity.

Secondly, possible design measures for enhancing the stability can already be derived: the inherent contributions can mostly be varied by changing the relative position of the flame with respect to the acoustic modes of interest, as well as by modifying the local gradient values of the mean heat release rate. To this end, a more profound analysis of the technical premix case could yield interesting conclusions. However, it should be preceded by an in-depth validation of the numerical simulation techniques with detailed measurement data, which are not available yet. Building on this, systematic flame shape variations could be induced mainly by varying the operating conditions, i.e. flow temperatures and velocities. The impact on thermoacoustic feedback could then be examined on the basis of the presented post-processing tools and flame transfer function formulations. Here again, close cooperation with the experiment would be important, especially since the impact of pressure sensitivity has not been confirmed in experiments yet.

Furthermore, additional contributions to the thermoacoustic feedback exist which are highly case-dependent. These relate in particular to variations of the flame surface, which are typically caused by perturbations of the mixing shear layer at the burner lip by transverse acoustic velocity fluctuations. As could be seen in particular for the perfect premix case, very high local Rayleigh index values can appear because of flame area fluctuations. At the global scale, these fluctuations can cancel out each other as for the perfect premix 1T excitation case, but not necessarily, as could be observed especially for the 2T excitation and the technical premix case. What follows is the indication that geometric modifications of the burner exit region might allow to influence the flame wrinkling in the shear layers and hence the corresponding thermoacoustic feedback.

From the investigations reported here one cannot identify suitable design measures for influencing the flame surface modulations. This has to be done in future work, by defining possible design measures and evaluating their impact on the thermoacoustic feedback. The excitation and post-processing techniques introduced in the present work should also be helpful for this kind of investigation. However, to save computational time, a broadband analysis might be more suitable. For instance, system identification could be used as in longitudinal mode analysis [45, 53, 55, 115] to analyse the response of shear layer combustion over a large frequency range using a single CFD run. Since the response is triggered by velocity fluctuations, an incompressible simulation setup could be used for such investigations, thus avoiding acoustic resonance. Transverse velocity excitation can be applied as in the present work using momentum source terms in transverse direction, although it should be applied directly in the flame region in an incompressible setup. A preliminary study made by the author indicates that such a setup allows to obtain a valid broadband excitation of transverse velocity. From a methodical point of view, such an analysis could be challenging, as the phenomena of shear layer instability and flame wrinkling tend to yield a non-linear system behaviour [2]. Such investigations therefore might represent an interesting study object for non-linear system identification techniques. Regarding the technical application, it would also be very interesting to investigate the interaction of shear layer combustion with effusion cooling through the burner walls.

8 Summary and Outlook

The present work proposes a two-fold extension to the thermoacoustic theory of gas turbine combustion systems. It is specifically dedicated to capturing the flame dynamics that appear in reheat combustors of sequential combustion systems, i.e. by dealing with the occurrence of auto-ignition due to high inlet temperatures. Moreover, it focusses on the stability of transverse modes at elevated frequencies, for which the widely used acoustic compactness assumption for the flame is not valid anymore. These aspects have been treated conjointly throughout this work in order to propose a consistent description of the phenomena that leads the way toward prediction tools that can be used in the future in industrial design processes.

The foundation was laid in chapter 2, which discussed differences between auto-igniting and propagating flames, between compactness and non-compactness. In conclusion, a mathematical formalism has been proposed for heat release rate fluctuations, expressed at a local scale, that can be applied for auto-igniting as well as for propagating flames. It splits the fluctuations into three main contributions, namely variations of density, mass-specific reaction rate, and flame position. The latter represents a peculiarity for non-compact flames, whose movement can lead to significant feedback because of the short acoustic wavelength of high-frequency pulsations. Its relevance had been discussed earlier [74, 109], including a first model description for thin flames in [109]. The model has been extended in the present work in order to be applicable to distributed reaction zones as well, which often appear when auto-ignition is involved.

From the formalism to the prediction tool, quantitative relations need to be provided for characterising the individual heat release rate oscillation terms. In this work, various numerical methods have been employed: detailed chemistry calculations (homogeneous reactors, plug-flow reactors, and 1D flames), large eddy simulations, and acoustic network tools (see chapter 3). The use of the former is described in chapter 4 and is motivated by the high inlet temper-

atures in reheat combustors and the appearance of auto-ignition. Reaction chemistry plays an important role therein and the thermoacoustic feedback linked to the pressure sensitivity of reaction rates has thus been studied. A relevant sensitivity factor has been defined and quantified; it was found to be applicable to both auto-ignition and flame propagation. The values obtained for the sensitivity factor are significant and indicate a strong thermoacoustic coupling caused by this mechanism. The sensitivity factor has been used in a newly developed analytical model, which allows to express the dynamic response of auto-ignition flames to acoustic perturbations for simplified configurations. At high frequencies, this feedback mechanism is dominated by an instantaneous flame response to local pressure fluctuations in the heat release zone.

Three-dimensional setups have been studied using large eddy simulations of two generic, acoustically excited test cases, with perfect and technical premixing. The simpler test case allowed the observation of distinct flame response mechanisms: acoustic and turbulent displacement, flame surface and density variations, as well as contributions of pressure sensitivity when using an extension of the combustion model. Based on a novel description of local heat release rate fluctuations, a filter-based postprocessing method has been developed that allows to obtain field distributions of fluctuation values and, more important, of the thermoacoustic feedback in terms of a local Rayleigh index. Going further, individual contributions could be quantified and the total feedback has been successfully reconstructed from its constituents, a fact that underlines the general applicability of the formalism. The increased geometrical complexity of the technical premix case did not significantly alter the flame dynamics, as similar response mechanisms were observed, but it becomes more difficult to distinguish between the different effects. Interestingly, periodic perturbations of the fuel injection by transverse modes could be observed, although they were dissipated by turbulent diffusion before reaching the combustion chamber. For the premix test case, the results indicate a largely dominant role of the pressure sensitivity in the thermoacoustic coupling, whereas its importance is less pronounced for the technical premix case.

Building on these observations, a distinction between inherent and variable feedback contributions has been made in chapter 7, based on how strongly the different response mechanisms depend on combustor geometry and op-

erating conditions. Moreover, modelled flame transfer functions have been formulated for the inherent contributions. Applied to the LES test cases, they proved to be able to give valid estimations of the thermoacoustic feedback. The exemplary use in an acoustic network calculation is meant to indicate how these quantitative relations can be employed in multi-dimensional FEM calculations for stability predictions of industrial burners.

The following principal conclusions are drawn from the present work:

1. At high frequencies, the analysis of heat release fluctuations and thermoacoustic feedback has to be conducted at a local scale, in order to account for the non-compactness of the flame with respect to the acoustic mode.

2. The pressure sensitivity of chemical formation rates causes significant thermoacoustic feedback in auto-ignition flames. At high frequencies, the heat release rate is likely to show an instantaneous response to local pressure perturbations, as indicated by Eq. (4.58).

3. Using LES and a detailed data postprocessing, various flame feedback mechanisms are identified. A theoretical formalism is proposed to decompose local heat release rate fluctuations into individual contributions, which can be classified into inherent and variable flame response contributions.

4. Flame transfer function formulations are derived to model local heat release rate fluctuations caused by the inherent contributions, i.e. density fluctuations, acoustic displacement, and pressure sensitivity. Their application to the LES results allows an accurate reconstruction of the total thermoacoustic feedback. A possible use in acoustic stability analysis of industrial combustors is indicated.

The findings of this work need to be corroborated by experimental observations, in particular by an experimental verification of the pressure sensitivity. This would ideally ask for a perfect premix configuration stabilised by auto-ignition, which is practically impossible to realise in a test rig. Alternatively, the test rig corresponding to the technical premix test case could deliver interesting results. Therefore, a detailed mapping of operating points should be

built up using experiments, in order to identify conditions that are suitable for a cross-check between simulation and experiments.

While it is sensible to compare the mean flame behaviour conventionally on the basis of velocity, temperature, and/or heat release rate distributions, it would be interesting to compare the system dynamics with respect to growth rates. The main motivation lies in the fact that this would correspond to an assessment of the entire three-dimensional domain. Moreover, difficulties regarding the experimental assessment of heat release rate (see the works of Lauer et al. [61, 62]) can be avoided. Instead, growth rates have to be quantified in both experiment and simulation. To this end, researchers from Alstom [113] and from TU München [111, 118] have reported new methods to determine growth rates in combustor test rigs. On the numerical side, it was shown in the present work that Rayleigh index values can be converted into growth rate contributions. The postprocessing must therefore be expanded to all three dimensions. In addition, acoustic damping rates could be deduced from amplitude-decaying time-domain simulations or from FEM simulations. In order to be able to confront experimental and numerical values, the acoustic impedance of liner walls needs to be assessed. Correspondingly, time-domain implementation variable impedance boundary conditions could be of interest for numerical simulations, possibly building up on the works of Lamarque et al. [60] or Polifke and co-workers [47, 53]. Eventually, a reliable method for assessing numerical dissipation in LES would be valuable. These extensions would facilitate systematic and quantitative studies of flame dynamics and could be employed for potential future investigations regarding the design impact on high-frequency mode stability that were discussed in section 7.4.

Supervised Theses

Im Rahmen dieser Dissertation entstanden am Lehrstuhl für Thermodynamik in den Jahren 2009 bis 2012 unter wesentlicher wissenschaftlicher, fachlicher und inhaltlicher Anleitung des Autors die im Folgenden aufgeführten studentischen Arbeiten. In ihnen wurden verschiedene Fragestellungen zur Verbrennung und Thermoakustik untersucht. Ergebnisse aus diesen Arbeiten sind in Teilen in das vorliegende Dokument eingeflossen. Der Autor dankt hiermit nochmals explizit allen ehemals betreuten Studenten für ihr Engagement bei der Unterstützung dieser wissenschaftlichen Arbeit.

Associated with this Ph.D. thesis are a number of "student theses" (Semesterarbeiten, Diplomarbeiten, Bachelor theses, or Master theses) that were supervised by the author of the present work. These theses were prepared at the Lehrstuhl für Thermodynamik in the years 2009 through 2012 under the close supervision of the present author in its full academical and professional breadth. Various issues were investigated concerning combustion and thermoacoustics. Parts of those supervised theses have been incorporated into the present thesis. Finally, the author would like to express his sincere gratitude to all formerly supervised students for their commitment supporting this research project.

Student	**Thesis**
Simon Rouchier	*Extension of the TFC Model Including Effects of Stretch and Mixture Inhomogeneities*, Diplomarbeit, filed in September 16th, 2009.
Michael Kolb	*Anwendbarkeit eines kommerziellen Lösers für linearisierte Navier-Stokes-Gleichungen zur Untersuchung thermoakustischer Probleme*, Semesterarbeit, filed in April 29th, 2010.
Christoph Meraner	*LES basierte Untersuchung des Einflusses von Wirbelablösung auf die Flammendynamik in sequentiellen Brennkammern*, Diplomarbeit, filed in November 17th, 2011.
Viona Müller	*Einflüsse von Streckung und Wärmeverlusten auf Wärmefreisetzung und Chemilumineszenz in laminaren Gegenstromflammen*, Bachelorarbeit, filed in September 3rd, 2012.
Josselin Guillozet	*LES-Based Investigation of the Flame Response to Transversal Acoustic Modes in Sequential Gas Turbine Combustors*, Diplomarbeit, filed in November 27th, 2012.

References

[1] ANSYS. General documentation. Fluent, release 13.

[2] R. Balachandran, B. Ayoola, C. Kaminski, A. Dowling, and E. Mastorakos. Experimental investigation of the nonlinear response of turbulent premixed flames to imposed inlet velocity oscillations. *Combustion and Flame*, 143:37–55, 2005.

[3] K. Balasubramanian and R. Sujith. Non-normality and nonlinearity in combustion-acoustic interaction in diffusion flames. *Journal of Fluid Mechanics*, 594:29–57, 2008.

[4] G. Bansal, H. Im, and S.-R. Lee. Auto-ignition of a homogeneous hydrogen-air mixture subjected to unsteady temperature fluctuations. *Combustion Theory and Modelling*, 13(3):413–425, 2009.

[5] R. Blumenthal, P. Subramanian, R. Sujith, and W. Polifke. Novel perspectives on the dynamics of premixed flames. *Combustion and Flame*, 160(7):1215–1224, 2013.

[6] R. Borghi. On the structure and morphology of turbulent premixed flames. In C. Bruno and C. Casci, editors, *Recent advances in aeronautical sciences*. Pergamon Press, 1984.

[7] M. Bothien, N. Noiray, and B. Schuermans. A novel damping device for broadband attenuation of low-frequency combustion pulsations in gas turbines. In *Proceedings of the ASME Turbo Expo 2012, GT2012-68873*, 2012.

[8] D. Bradley, L. Kwa, A. Lau, and M. Missaghi. Laminar flamelet modelling of recirculating premixed methane and propane-air combustion. *Combustion and Flame*, 71:109–122, 1988.

[9] M. Brandt. *Beschreibung der Selbstzündung in turbulenter Strömung unter Einbeziehung ternärer Mischvorgänge*. PhD thesis, Technische Universität München, 2005.

[10] M. Brandt, W. Polifke, B. Ivancic, P. Flohr, and B. Paikert. Auto-ignition in a gas turbine burner at elevated temperature. In *Proceedings of the ASME Turbo Expo, 2003-GT-38224*, Atlanta, GA, U.S.A., June 2003.

[11] R. Cabra, J.-Y. Chen, R. Dibble, A. Karpetis, and R. Barlow. Lifted methane-air jet flames in a vitiated coflow. *Combustion and Flame*, 143(4):491–506, 2005.

[12] R. Cabra, T. Myhrvold, J.Y. Chen, R. Dibble, A. Karpetis, and R. Barlow. Simultaneous laser Raman-Rayleigh-LIF measurements and numerical modeling results of a lifted turbulent H2/N2 jet flame in a vitiated coflow. *Proceedings of the Combustion Institute*, 29(2):1881–1888, 2002.

[13] I. Celik, Z. Cehreli, and N. Yavuz. Index of resolution quality for large eddy simulations. *Journal of Fluids Engineering*, 127:949–958, 2005.

[14] P. Clavin, P. Pelcé, and L. He. One-dimensional vibratory instability of planar flames propagating in tubes. *Journal of Fluid Mechanics*, 216:299–322, 1990.

[15] O. Colin, C. Pera, and S. Jay. Detailed chemistry tabulation based on a FPI approach adapted and applied to 3-D internal combustion engine calculations. In *Proceedings of the European Combustion Meeting, ECM2007*, 2007.

[16] L. Crocco and S. Cheng. *Theory of combustion instability in liquid propellant rocket motors*. Butterworths Scientific Publications, 1956.

[17] F. Culick. Nonlinear growth and limiting amplitude of acoustic oscillations in combustion chambers. *Combustion Science and Technology*, 3:1–16, 1971.

[18] F. Culick. Nonlinear behavior of acoustic waves in combustion chambers, parts I and II. *Acta Austronautica*, 3:714–757, 1976.

[19] F. Culick. Unsteady motions in combustion chambers for propulsion systems. Technical report, Research and Technology Organisation, North Atlantic Treaty Organisation (NATO), 2006.

[20] E. Deuker. *Ein Beitrag zur Vorausberechnung des akustischen Stabilitätsverhaltens von Gasturbinen-Brennkammern mittels theoretischer und experimenteller Analyse von Brennkammerschwingungen.* VDI Verlag: Fortschrittsberichte, Reihe 6: Energietechnik, RWTH Aachen, 1994.

[21] K. Döbbeling, J. Hellat, and H. Koch. 25 Years of BBC/ABB/Alstom lean premix combustion technologies. *Journal of Engineering for Gas Turbines and Power*, 129(1):2–12, 2007.

[22] A. Dowling. The calculation of thermoacoustic oscillations. *Journal of Sound and Vibration*, 180(4):557–581, 1995.

[23] A. Dowling. Nonlinear self-excited oscillations of a ducted flame. *Journal of Fluid Mechanics*, 346:271–290, 1997.

[24] S. Ducruix, T. Schuller, D. Ducrox, and S. Candel. Combustion dynamics and instabilities: Elementary coupling and driving mechanisms. *Journal of Propulsion and Power*, 19(5):722–734, 2003.

[25] T. Echekki and E. Mastorakos, editors. *Turbulent combustion modeling - Advances, new trends and perspectives.* Fluid mechanics and its applications. Springer, 2011.

[26] A. Eroglu, K. Döbbeling, F. Joos, and P. Brunner. Vortex generators in lean-premix combustion. *Journal of Engineering for Gas Turbines and Power*, 123:41–49, 2001.

[27] J. Fleck, P. Griebel, A. Steinberg, and M. Aigner. Autoignition of hydrogen/natural gas/nitrogen fuel mixtures at reheat combustor operating conditions. In *Proceedings of ASME Turbo Expo 2012, GT2012-68401*, 2012.

[28] F. Galeazzo, C. Prathap, M. Kern, P. Habisreuther, N. Zarzalis, C. Beck, W. Krebs, and B. Wegner. Investigation of a flame anchored in cross-flow stream of vitiated air at elevated pressures. In *Proceedings of ASME Turbo Expo 2012, GT2012-69632*, 2012.

[29] J. Galpin, A. Naudin, L. Vervisch, C. Angelberger, O. Colin, and P. Domingo. Large-eddy simulation of a fuel-lean premixed turbulent swirl-burner. *Combustion and Flame*, 155(1-2):247–266, 2008.

[30] J. Gikadi, T. Sattelmayer, and A. Peschiulli. Effects of the mean flow field on the thermo-acoustic stability of aero-engine combustion chambers. In *Proceedings of ASME Turbo Expo 2012, GT2012-69612*, 2012.

[31] D. Goodwin. Cantera: An object-oriented software toolkit for chemical kinetics, thermodynamics, and transport processes, 2009. Caltech, Pasadena. [Online]. Available: http://code.google.com/p/cantera.

[32] R. Gordon, A. Masri, and E. Mastorakos. Simultaneous rayleigh temperature, oh- and ch2o-lif imaging of methane jets in a vitiated coflow. *Combustion and Flame*, 155(1-2):181–195, 2008.

[33] R. Gordon, A. Masri, S. Pope, and G. Goldin. A numerical study of autoignition in turbulent lifted flames issuing into a vitiated co-flow. *Combustion Theory and Modelling*, 11(3):351–376, 2007.

[34] R. Gordon, A. Masri, S. Pope, and G. Goldin. Transport budgets in turbulent lifted flames of methane autoigniting in a vitiated co-flow. *Combustion and Flame*, 151(3):495–511, 2007.

[35] F. Guethe, J. Hellat, and P. Flohr. The reheat concept: the proven pathway to ultra-low emissions and high efficiency and flexibility. In *ASME Turbo Expo, GT2007-27846*, 2007.

[36] J. Guillozet. LES-based investigation of the flame response to transversal acoustic modes in sequential gas turbine combustors. Diploma thesis, Technische Universität München/Alstom Power, 2012.

[37] M. Hauser, M. Lorenz, and T. Sattelmayer. Influence of transversal acoustic excitation of the burner approach flow on the flame structure. *Journal of Engineering for Gas Turbines and Power*, 133(4):041501/1–8, 2011.

[38] S. Hayashi, H. Yamada, and M. Makida. Extending low-NOx operating range of a lean premixed-prevaporized gas turbine combustor by reaction of secondary mixtures injected into primary stage burned gas. *Proceedings of the Combustion Institute*, 30(2):2903–2911, 2005.

[39] J. Hellat. Development of low emission combustion for gas turbines. In *Presentation at ASME Turbo Expo 2012*, 2012.

[40] R. Hilbert and D. Thévenin. Autoignition of turbulent non-premixed flames investigated using direct numerical simulations. *Combustion and Flame*, 128(1-2):22–37, 2002.

[41] A. Hoffmann. *Modellierung turbulenter Vormischverbrennung*. PhD thesis, Universität Karlsruhe (TH), 2004.

[42] B. Höflich, R. Noster, H. Peinl, P. Richard, J. Völker, D. Echternacht, F. Grote, A. Schäfer, and H. Schuster. Integration der erneuerbaren Energien in den deutschen/europäischen Strommarkt. Technical report, Deutsche Energie-Agentur GmbH, 2012.

[43] Y. Huang, H.-G. Sung, S.-Y. Hsieh, and V. Yang. Large-eddy simulation of combustion dynamics of lean-premixed swirl-stabilized combustor. *Journal of Propulsion and Power*, 19(5):782–794, 2003.

[44] A. Huber. *Impact of fuel supply impedance and fuel staging on gas turbine combustion stability*. PhD thesis, Technische Universität München, 2009.

[45] A. Huber and W. Polifke. Dynamics of practical premix flames, part I: Model structure and identification. *International Journal of Spray and Combustion Dynamics*, 1(2):199–229, 2009.

[46] A. Huber and W. Polifke. Dynamics of practical premix flames, part II: Identification and interpretation of CFD data. *International Journal of Spray and Combustion Dynamics*, 1(2):229–250, 2009.

[47] A. Huber, P. Romann, and W. Polifke. Filter-based time-domain impedance boundary conditions for CFD applications. In *Proceedings of ASME Turbo Expo, GT2008-51195*, 2008.

[48] Z. Ibrahim, F. Williams, S. Buckley, and J. Lee. An acoustic energy approach to modeling combustion oscillations. In *Proceedings of the ASME Turbo Expo 2006, GT2006-90096*, 2006.

[49] M. Janus and G. Richards. Results of a model for premixed combustion oscillations. In *Proceedings of 1996 International Symposium Combustion in Industry*, 1996.

[50] W. Jones and S. Navarro-Martinez. Large eddy simulation of autoignition with a subgrid probability density function method. *Combustion and Flame*, 150:170–187, 2007.

[51] W. Jones, S. Navarro-Martinez, and O. Röh. Large eddy simulation of hydrogen auto-ignition with a probability density function method. *Proceedings of the Combustion Institute*, 31(2):1765–1771, 2007.

[52] F. Joos, P. Brunner, M. Stalder, and S. Tschirren. Field experience with the sequential combustion system of the GT24/GT26 gas turbine family. *ABB Review*, 5:12–20, 1998.

[53] R. Kaess, W. Polifke, T. Poinsot, N. Noiray, D. Durox, T. Schuller, and S. Candel. CFD-based mapping of the thermo-acoustic stability of a laminar premix burner. In *Proceedings of the 2008 Summer Program, Stanford Univ., Center for Turbulence Research*, pages 289–302, 2008.

[54] S. Kerkemeier. *Direct numerical simulation of combustion on petascale platforms: Application to turbulent non-premixed hydrogen autoignition*. PhD thesis, ETH Zürich, 2010.

[55] T. Komarek and W. Polifke. Impact of swirl fluctuations on the flame response of a perfectly premixed swirl burner. *Journal of Engineering for Gas Turbines and Power*, 132(6):061503–1,7, 2010.

[56] U. Krüger, J. Hüren, S. Hoffmann, W. Krebs, P. Flohr, and D. Bohn. Prediction and measurement of thermoacoustic improvements in gas turbines with annular combustion systems. In *Proceedings of the ASME Turbo Expo 2000, 2000-GT-0084*, 2000.

[57] R. Kulkarni. *Large eddy simulation of autoignition in turbulent flows*. PhD thesis, Technische Universität München, 2013.

[58] R. Kulkarni and W. Polifke. LES of Delft-Jet-In-Hot-Coflow (DJHC) with tabulated chemistry and stochastic fields combustion model. *Fuel Processing Technology*, 107:138–146, 2013.

[59] R. Kulkarni, M. Zellhuber, and W. Polifke. LES based investigation of autoignition in turbulent co-flow configurations. *Combustion Theory and Modelling*, 17(2):224–259, 2013.

[60] N. Lamarque, M. Porta, F. Nicoud, and T. Poinsot. On the stability and dissipation of wall boundary conditions for compressible flows. *International Journal for Numerical Methods in Fluids*, 62(10):1134–1154, 2010.

[61] M. Lauer and T. Sattelmayer. On the adequacy of chemiluminescence as a measure for heat release in turbulent flames with mixture gradients. *Journal of Engineering for Gas Turbines and Power*, 132(6:061502):1–8, 2010.

[62] M. Lauer, M. Zellhuber, C. Aul, and T. Sattelmayer. Determination of the heat release distribution in turbulent flames by a model based correction of OH* chemiluminescence. *Journal of Engineering for Gas Turbines and Power*, 133(12:1501):1–8, 2011.

[63] C. Lawn. Lifted flames on fuel jets in co-flowing air. *Progress in Energy and Combustion Science*, 35(1):1–30, 2009.

[64] T. Lieuwen. Modeling premixed combustion-acoustic wave interactions: A review. *Journal of Propulsion and Power*, 19(5):17, 2003.

[65] T. Lieuwen, Y. Neumeier, and B. Zinn. The role of unmixedness and chemical kinetics in driving combustion instabilities in lean premix combustors. *Combustion Science and Technology*, 135:193–211, 1998.

[66] T. Lieuwen, H. Torres, C. Johnson, and B. Zinn. A mechanism of combustion instability in lean premixed gas turbine combustors. *Journal of Engineering for Gas Turbines and Power*, 123(1):182–189, 2001.

[67] E. Mallard and H. Le Chatelier. Recherches expérimentales et théoriques sur la combustion des mélanges gazeux explosifs. In *Annales des Mines, 8e Série: Mémoires 4*, page 379, 1883.

[68] C. Markides. *Autoignition in turbulent flows*. PhD thesis, University of Cambridge, 2005.

[69] C. Markides and E. Mastorakos. An experimental study of hydrogen autoignition in a turbulent co-flow of heated air. *Proceedings of the Combustion Institute*, 30(1):883–891, 2005.

[70] E. Mastorakos. Ignition of turbulent non-premixed flames. *Progress in Energy and Combustion Science*, 35:57–97, 2009.

[71] MathWorks. Matlab, 2011. version R2011b.

[72] A. McIntosh. The linearised response of the mass burning rate of a premixed flame to rapid pressure changes. *Combustion Science and Technology*, 91(4):329–346, 1993.

[73] C. Meraner. LES-basierte Untersuchung des Einflusses von Wirbelablösung auf die Flammendynamik in sequentiellen Brennkammern. Diploma thesis, Technische Universität München, 2011.

[74] Y. Méry, L. Hakim, P. Scouflaire, L. Vingert, S. Ducruix, and S. Candel. Experimental study of the combustion-acoustics coupling in liquid rocket engine high-frequency instabilities. In *Proceedings of AAAF-ESA-CNES Space Propulsion 2012*, Bordeaux, France, 2012.

[75] J.-B. Michel, O. Colin, and C. Angelberger. On the formulation of species reaction rates in the context of multi-species CFD codes using complex chemistry tabulation techniques. *Combustion and Flame*, 157(4):701–714, 2010.

[76] J. Moeck, M. Oevermann, R. Klein, C. Paschereit, and H. Schmidt. A two-way coupling for modeling thermoacoustic instabilities in a flat flame Rijke tube. *Proceedings of the Combustion Institute*, 32(1):1199–1207, 2009.

[77] D. Mukherjee. State-of-the-art gas turbines - a brief update. *ABB Review*, 2:4–14, 1997.

[78] R. Mustata, L. Valino, C. Jimenez, W. Jones, and S. Bondi. A probability density function Eulerian Monte Carlo field method for large eddy simulations: Application to a turbulent piloted methane/air diffusion flame (Sandia D). *Combustion and Flame*, 145(1-2):88–104, 2005.

[79] A. Ni, W. Polifke, and F. Joos. Ignition delay time modulation as a contribution to thermoacoustic instability in sequential combustion. In *Proceedings of ASME Turbo Expo, 2000-GT-0103*, 2000.

[80] W. Nicholson. On the sound produced by a current of hydrogen gas passing through a tube. *A Journal of Natural Philosophy, Chemistry, and the Arts*, 1:129–131, 1802.

[81] N. Noiray, D. Durox, T. Schuller, and S. Candel. A unified framework for nonlinear combustion instability analysis based on the flame describing function. *Journal of Fluid Mechanics*, 615(-1):139–167, 2008.

[82] J. O'Connor and T. Lieuwen. Disturbance field characteristics of a transversely excited burner. *Combustion Science and Technology*, 183:427–443, 2011.

[83] J. O'Connor and T. Lieuwen. Further characterization of the disturbance field in a transversely excited swirl-stabilized flame. *Journal of Engineering for Gas Turbines and Power*, 134:1–9, 2012.

[84] J. O'Connor, S. Natarajan, M. Malanoski, and T. Lieuwen. Disturbance field characteristics of a transversely excited annular jet. In *Proceedings of ASME Turbo Expo, GT2010-22133*, 2010.

[85] P. Palies, D. Durox, T. Schuller, and S. Candel. The combined dynamics of swirler and turbulent premixed swirling flames. *Combustion and Flame*, 157(9):1698–1717, 2010.

[86] C. Paschereit, B. Schuermans, W. Polifke, and O. Mattson. Measurement of transfer matrices and source terms of premixed flames. *J. Eng. Gas Turbines and Power*, 124(2):239–247, 2002.

[87] N. Peters. The turbulent burning velocity for large-scale and small-scale turbulence. *Journal of Fluid Mechanics*, 384:107–132, 1999.

[88] E. Petersen, D. Kalitan, S. Simmons, G. Bourque, H. Curran, and J. Simmie. Methane/propane oxidation at high pressures: Experimental and detailed chemical kinetic modeling. *Proceedings of the Combustion Institute*, 31(1):447–454, 2007.

[89] C. Pierce and P. Moin. Progress-variable approach for large-eddy simulation of non-premixed turbulent combustion. *Journal of Fluid Mechanics*, 504(1):73–97, 2004.

[90] J. Pieringer. *Simulation selbsterregter Verbrennungsschwingungen in Raketenschubkammern im Zeitbereich*. PhD thesis, Technische Universität München, 2008.

[91] T. Poinsot and D. Veynante. *Theoretical and numerical combustion*. R. T. Edwards, Inc., 2nd edition, 2005.

[92] W. Polifke, J. Kopitz, and A. Serbanovic. Impact of the fuel time lag distribution in elliptical premix nozzles on combustion stability. In *7th AIAA/CEAS Aeroacoustics Conference, AIAA 2001-2104*, 2001.

[93] W. Polifke and C. Lawn. On the low-frequency limit of flame transfer functions. *Combust. Flame*, 151(3):437–451, 2007.

[94] W. Polifke, A. Poncet, C. Paschereit, and K. Döbbeling. Reconstruction of acoustic transfer matrices by instationary computational fluid dynamics. *Journal of Sound and Vibration*, 245(3):483–510, 2001.

[95] M. Poyyapakkam, J. Wood, S. Mayers, A. Ciani, F. Guethe, and K. Syed. Hydrogen combustion within a gas turbine reheat combustor. In *Proceedings of ASME Turbo Expo 2012, GT2012-69165*, 2012.

[96] Lord Rayleigh. The explanation of certain acoustical phenomena. *Nature*, 18(455):319–321, 1878.

[97] P. Rijke. On the vibration of the air in a tube open at both ends. *Philosophical Magazine*, 17:419–422, 1859.

[98] R. Rook, L. Goey, L. Somers, K. Schreel, and R. Parchen. Response of burner-stabilized flat flames to acoustic perturbations. *Combustion Theory and Modelling*, 6(2):223–242, 2002.

[99] T. Sattelmayer. Influence of the combustor aerodynamics on combustion instabilities from equivalence ratio fluctuations. *Journal of Engineering for Gas Turbines and Power*, 125(1):11–19, 2003.

[100] S. Savic, K. Lindvall, T. Papadopoulos, and M. Ladwig. The next generation KA24/GT24 from Alstom, the pioneer in operational flexibility. Technical report, Alstom Power, 2011.

[101] H. Schmidt and C. Jimenez. Numerical study of the direct pressure effect of acoustic waves in planar premixed flames. *Combustion and Flame*, 157(8):1610–1619, 2010.

[102] L. Schmidt. *The engineering of chemical reactions*. Oxford University Press, 1st edition, 1998.

[103] D. Schmitt, M. Kolb, J. Weinzierl, C. Hirsch, and T. Sattelmayer. Ignition and flame stabilization of premixed jet in hot cross flow. In *Proceedings of the ASME Turbo Expo 2013, GT2013-94763*, 2013.

[104] B. Schuermans. *Modeling and control of thermoacoustic instabilities*. PhD thesis, Ecole Polytechnique Fédérale de Lausanne (EPFL), 2003.

[105] B. Schuermans, H. Luebcke, D. Bajusz, and P. Flohr. Thermoacoustic analysis of gas turbine combustion systems using unsteady CFD. In *Proceedings of ASME Turbo Expo, GT2005-68393*, 2005.

[106] B. Schuermans, W. Polifke, and C. Paschereit. Modeling transfer matrices of premixed flames and comparison with experimental results. In *Proceedings of ASME Turbo Expo 1999, 99-GT-132*, 1999.

[107] T. Schuller, D. Durox, and S. Candel. A unified model for the prediction of laminar flame transfer functions: comparisons between conical and V-flame dynamics. *Combustion and Flame*, 134:21–34, 2003.

[108] J. Schwing. *Hochfrequente Instabilitäten in Drallbrennkammern von Gasturbinen*. PhD thesis, Technische Universität München, 2013.

[109] J. Schwing, F. Grimm, and T. Sattelmayer. A model for the thermoacoustic feedback of transverse acoustic modes and periodic oscillations in flame position in cylindrical flame tubes. In *Proceedings of ASME Turbo Expo 2012, GT2012-68775*, 2012.

[110] J. Schwing, N. Noiray, and T. Sattelmayer. Interaction of vortex shedding and transverse high-frequency pressure oscillations in a tubular combustion chamber. In *Proceedings of ASME Turbo Expo, GT2011-45246*, Vancouver, Canada, 2011. ASME.

[111] J. Schwing and T. Sattelmayer. High-frequency instabilities in cylindrical flame tubes: Feedback mechanism and damping. In *Proceedings of ASME Turbo Expo 2013, GT2013-94064*, 2013.

[112] F. Selimefendigil and W. Polifke. A frequency domain system model with coupled modes for limit cycle prediction of thermoacoustic systems. *International Journal of Spray and Combustion Dynamics*, 3(4):303–330, 2011.

[113] G. Singla, N. Noiray, and B. Schuermans. Combustion dynamics validation of an annular reheat combustor. In *Proceedings of the ASME Turbo Expo 2012, GT2012-68684*, 2012.

[114] L. Spadaccini and M. Colket. Ignition delay characteristics of methane fuels. *Progress in Energy and Combustion Science*, 20:431–460, 1994.

[115] L. Tay Wo Chong, T. Komarek, R. Kaess, S. Föller, and W. Polifke. Identification of flame transfer functions from LES of a premixed swirl burner. In *Proceedings of ASME Turbo Expo 2010, GT2010-22769*, 2010.

[116] L. Valino. A field Monte Carlo formulation for calculating the probability density function of a single scalar in a turbulent flow. *Flow, Turbulence and Combustion*, 60(2):157–172, 1998.

[117] J. Villermaux and J.C. Devillon. Représentation de la coalescence et de la redispersion des domaines de ségrégation dans un fluide par un modèle d'interaction phénoménologique. In *Proceedings of the 2nd Int'l Symposium on Chemical Reaction Engineering*, 1972.

[118] M. Wagner, C. Jörg, and T. Sattelmayer. Comparison of the accuracy of time-domain measurement methods for combustor damping. In *Proceedings of the ASME Turbo Expo 2013, GT2013-94844*, 2013.

[119] K. Wieczorek. *Numerical study of Mach number effects on combustion instability*. PhD thesis, Université Montpellier II, 2010.

[120] F. Williams. *Combustion theory*. The Benjamin/Cummings Publishing Company, Inc., 2nd edition, 1985.

[121] X. Wu, M. Wang, P. Moin, and N. Peters. Combustion instability due to the nonlinear interaction between sound and flame. *Journal of Fluid Mechanics*, 497:23–53, 2003.

[122] M. Zellhuber, V. Bellucci, B. Schuermans, and W. Polifke. Modelling the impact of acoustic pressure waves on auto-ignition flame dynamics. In *Proceedings of the European Combustion Meeting, ECM2011*, 2011.

[123] M. Zellhuber, C. Meraner, R. Kulkarni, B. Schuermans, and W. Polifke. Large eddy simulation of flame response to transverse acoustic excitation in a model reheat combustor. In *Proceedings of the ASME Turbo Expo 2012, GT2012-68317*, 2012.

[124] M. Zellhuber, C. Meraner, R. Kulkarni, B. Schuermans, and W. Polifke. Large eddy simulation of flame response to transverse acoustic excita-

tion in a model reheat combustor. *Journal of Engineering for Gas Turbines and Power*, 135(9):091508/1–9, 2013.

[125] M. Zellhuber and W. Polifke. Large-eddy-simulation of high-frequency flame dynamics in perfect premix combustors with elevated inlet temperatures. In *Ercoftac workshop on Direct and Large-Eddy Simulation, DLES-9*, 2013.

[126] M. Zellhuber, B. Schuermans, and W. Polifke. Impact of acoustic pressure on auto-ignition and heat release. *Combustion Theory and Modelling*, pages 1–31, 2014, doi:10.1080/13647830.2013.817609.

[127] M. Zellhuber, J. Schwing, B. Schuermans, T. Sattelmayer, and W. Polifke. Experimental and numerical investigation of thermoacoustic sources related to high-frequency instabilities. *International Journal of Spray and Combustion Dynamics*, 6(1):1–34, 2014.

[128] M. Zellhuber, L. Tay Wo Chong, and W. Polifke. Non-linear flame response at small perturbation amplitudes - consequences for analysis of thermoacoustic instabilities. In *Proceedings of the European Combustion Meeting, ECM2011*, 2011.